Progress in Materials Science 163 (2027) 101762

Contents lists available at ScienceDirect

Progress in Materials Science

journal homepage: www.elsevier.com/locate/pmatsci

Electrochemical methods for restructuring of metal surfaces: mechanisms and strategies for tailoring free-standing electrocatalysts

Mohamed M. Elnagar [a,b,c,*], Ludwig A. Kibler [a], Timo Jacob [a,b,c,*]

[a] Institute of Electrochemistry, Ulm University, 89069 Ulm, Germany
[b] Helmholtz-Institute-Ulm (HIU) Electrochemical Energy Storage, 89081 Ulm, Germany
[c] Karlsruhe Institute of Technology (KIT), P.O. Box 3640, 76021 Karlsruhe, Germany

ARTICLE INFO

Keywords:
Electrochemical restructuring
Nanostructured metal electrodes
Structure–activity relationships
Cathodic corrosion
Stability of metal electrodes
Binder-free electrodes
Electrocatalysis

ABSTRACT

Electrocatalysis is driven by the chemical nature of electrodes and their surfaces. Furthermore, the electrocatalytic activity and selectivity critically depend on the atomic surface arrangement of electrodes, characterized by facets and their crystallographic orientation, surface steps, and defects, *i.e.,* the electrode surface structure. Over the past decades, single-crystal studies have provided fundamental insights into so-called structure–activity relationships, while nanoparticle systems have extended this knowledge toward industrial electrocatalysts. Yet, translating these insights into practical electrodes remains limited by the use of binders, supports, and surfactants, which mask active sites, compromise stability, and hinder reproducibility. This review provides a framework for the electrochemical restructuring of metal electrodes, emphasizing how electrochemical processes can generate nanostructured, binder-free, free-standing electrodes with tailored surface architectures. We critically evaluate restructuring strategies, including electrodeposition, potential cycling, anodic polarization, electrochemical dealloying, and particularly cathodic corrosion, reframing the latter not only as a degradation pathway but also as a versatile tool for fine-tuning metal surfaces and fabricating flexible electrodes. Fundamental insights into

Abbreviations: 2D, Two-dimensional; ADMCs, Atomically dispersed metal catalysts; *A*OH (*A* = Li, Na, K, Cs), Alkali metal hydroxides; CP-EGOR, Constant-potential ethylene glycol oxidation; CO_2RR, Carbon dioxide electrochemical reduction reaction; DFT, Density functional theory; DGNs, Dendrite-like gold nanostructures; DMF, Dimethylformamide; EDS, Energy-dispersive X-ray spectroscopy; EG, Ethylene glycol; EASA, Electrochemically active surface area; FAOR, Formic acid oxidation reaction; FCC, Face-centered cubic; FE, Faradaic efficiency; GA, Glycolic acid; GC, Glassy carbon; H_{ad}, Adsorbed hydrogen; HAADF-STEM, High-angle annular dark-field scanning transmission electron microscopy; HER, Hydrogen evolution reaction; HERFD-XANES, High-energy-resolution fluorescence-detected X-ray absorption near-edge structure; HESXRD, High-energy surface X-ray diffraction; HPLC, High-performance liquid chromatography; HOR, Hydrogen oxidation reaction; IL-TEM, Identical-location transmission electron microscopy; LEED, Low-energy electron diffraction; LOD, Limit of detection; LSV, Linear sweep voltammetry; MSE, Saturated Mercury sulfate electrode; NCs, Nanocubes; Ni–Ru/PTE, Ni–Ru catalyst-integrated porous transport electrode; NO_2RR, Nitrite reduction reaction; NO_3RR, Nitrate reduction reaction; NP, Nanoparticle; NPG, Nanoporous gold; ODs, Nano-octahedra; OER, Oxygen evolution reaction; OPD, Overpotential deposition; ORCs, Oxidation–reduction cycles; ORR, Oxygen reduction reaction; pc-NPG, Potential cycling-derived nanoporous gold; PEMWE, Proton exchange membrane water electrolysis; pzc, Potential of zero charge; R, Enhancement factor; HE, Reversible hydrogen electrode; RSWPS, Repetitive symmetrical square-wave potential signal; SCE, Saturated calomel electrode; SECCM, Scanning electrochemical cell microscopy; SEM, Scanning electron microscopy; SERS, Surface-enhanced Raman spectroscopy; STM, Scanning tunneling microscopy/microscope; SWP, Square-wave potential; THH, Tetrahexahedral; UPD, Underpotential deposition; XAS, X-ray absorption spectroscopy.

* Corresponding authors.
E-mail addresses: mohamed.elnagar@uni-ulm.de (M.M. Elnagar), timo.jacob@uni-ulm.de (T. Jacob).

https://doi.org/10.1016/j.pmatsci.2026.101762
Received 27 August 2025; Received in revised form 29 April 2026; Accepted 2 June 2026
Available online 6 June 2026

cathodic corrosion are discussed in detail, linking atomic-scale restructuring mechanisms with the emergence of features relevant for catalysis and electrocatalysis. We further address stability challenges, parameters influencing restructuring, and applications in electrocatalysis, including HER and OER, CO_2 reduction, nitrate reduction, and electro-oxidation of small organic molecules as candidates for fuels in energy storage and conversion. This review bridges electrochemical surface science with engineering of electrode materials to provide a roadmap for advancing surface design in energy technology, electrochemical science, and sustainable catalysis.

1. Introduction

Electrocatalysis occupies a central position at the intersection of materials science, electrochemistry, and sustainable chemical engineering. It provides the fundamental basis for a broad spectrum of energy-conversion and chemical-manufacturing technologies, including fuel cells, water electrolyzers, electrochemical carbon dioxide and nitrogen conversion, oxygen electrochemistry, and organic electrosynthesis [1–8]. In these systems, simple and earth-abundant molecular feedstocks, such as H_2O, CO_2, N_2, O_2, and organic molecules, are converted into fuels, energy carriers, and value-added chemicals through electrocatalytic reactions occurring at electrified metal–electrolyte interfaces. Electrocatalysts are critical in these conversion reactions to lower the reaction energy barrier and the electrochemical overpotential, thus expediting the reaction rate, efficiency, and power [9]. An electrocatalytic reaction is typically a heterogeneous process that takes place at the "*electrified interface*" of a solid electrocatalyst and an electrolyte. At a simple electrochemical interface, complex chemical phenomena proceed during the electrochemical reaction, such as adsorption and desorption processes, electron- and charge-transfer reactions, solvation and desolvation, and electrostatic interactions, among others [10,11]. Taken together, these interfacial processes establish a direct link between the atomic-scale structure of the electrode surface and macroscopic electrocatalytic performance. While the chemical composition of the electrode defines the accessible reaction space, it is the surface structure and its dynamic evolution under applied electrochemical potentials that ultimately governs activity, selectivity, and stability [12]. Consequently, a central objective of electrocatalysis research is the rational design of electrode materials whose surface architectures are purposely tailored to achieve high intrinsic activity, controlled product selectivity, and sustained performance under technologically relevant operating conditions [13,14]. Foundational concepts in catalysis provide a guiding framework for this endeavor. According to Paul Sabatier (1854–1941), the optimized catalytic surface for a given reaction should have an optimized adsorption strength for the relevant reaction intermediates that is neither too strong nor too weak, an observation which, among others, earned him the 1912 Nobel Prize in Chemistry for his seminal work on hydrogenation catalysis [15–18]. Linus Pauling (1901–1994) added that the catalyst (in his case, an enzyme) must bind the transition state more tightly than the substrate [19]. These two concepts lie at the heart of catalysis at the active center. Thus, electrocatalytic reactions and electrode kinetics are affected by the adsorption of intermediates, which is typically very sensitive to the local atomic structure.

Moreover, the surface structure (roughness, grain boundaries, crystallographic orientation, facets, defects, heteroatom doping, surface morphology, etc.) of metal electrodes can remarkably influence the energetic pathways from reactants to products and, consequently, the reaction rate, activity, and selectivity [11,12,20]. Accordingly, establishing quantitative correlations between surface structure and electrocatalytic performance is essential for a fundamental understanding of electrochemical reactions and for the rational design of improved catalysts.

Driven by these insights, substantial effort has been devoted to the fabrication of nano- and microstructured metal surfaces with well-defined crystallographic orientation, enhanced electrochemically active surface area (EASA), and possessing numerous under-coordinated sites to enhance electrocatalytic activity while allowing correlation of electrochemical behavior and catalytic performance with surface structure [21–23]. Typically, the metal nano/micro-particles with a controlled surface structure are synthesized by solid-state or solution-based techniques in the presence of capping agents. However, capping agents can significantly alter or even block the intrinsic surface chemistry of the nano/micro-particle assemblies, thereby obscuring structure–activity relationships and limiting catalytic performance [24–26]. Furthermore, practical electrodes are often fabricated by depositing these materials onto conductive supports using polymeric binders such as Nafion or polytetrafluoroethylene. Under electrochemical operating conditions, such composite electrodes may suffer from mechanical degradation, diminished electrical conductivity, partial site blocking, and uncontrolled structural evolution, ultimately compromising performance and reproducibility [27].

In contrast, electrochemical approaches provide an alternative and fundamentally distinct route for tailoring metal electrode surfaces with enhanced properties [28–34]. Rather than relying on *ex-situ* synthesis and assembly, electrochemical methods exploit potential-controlled interfacial processes to directly restructure metal surfaces under well-defined conditions. Based on a fundamental understanding of electrochemical surface transformations, a range of strategies has emerged to fabricate nano- and microstructured, binder-free, and free-standing metal electrodes with exceptional electrochemical and electrocatalytic properties.

Despite the increasing interest in electrochemical surface restructuring, existing reviews have largely focused on specific aspects of the field, such as dynamic catalyst evolution under operating conditions [35–38] or the development of *operando* techniques for probing interfacial processes [39,40]. As a result, a unified materials-oriented framework that connects restructuring pathways to the resulting surface architectures and their electrocatalytic performance remains underdeveloped.

In this review, we critically examine the role of metal surface structure in electrocatalysis, with particular emphasis on insights gained from single-crystal studies and well-defined nanostructured electrodes. We highlight that electrocatalysts are not static entities: under reaction conditions, their surface structure may evolve dynamically in response to the applied potential, electrolyte

composition, pH, and the nature of the electrochemical reaction. Consequently, electrochemical processes such as potential-induced surface reconstruction, anodic oxidation, repetitive oxidation–reduction cycling, and cathodic corrosion are discussed in detail. Building on this mechanistic understanding, we comprehensively review electrochemical strategies for fabricating nanostructured metal electrodes, including (i) electrodeposition, (ii) anodic polarization, (iii) oxidation–reduction cycles, (iv) square-wave potential programming, (v) electrochemical dealloying, and (vi) negative polarization under certain conditions by the so-called cathodic corrosion. These approaches are discussed both in terms of their fundamental mechanisms and their ability to generate controlled surface architectures (Fig. 1).

Importantly, this review adopts a structure-oriented perspective in which electrochemical restructuring is treated not only as a dynamic phenomenon to be observed, but as a controllable toolbox for engineering metal surfaces. Rather than asking which method is superior, the central question addressed here is which electrochemical pathway is most suitable for generating a desired surface architecture and catalytic function. This perspective provides a unifying framework that links electrochemical processes to structure–property relationships and practical electrode design.

Within this framework, particular emphasis is placed on cathodic corrosion, which has a dual role in electrocatalysis. On one hand, it can act as a degradation pathway during electrochemical conversion reactions, influencing catalyst stability and long-term performance [41]. On the other hand, cathodic corrosion can be applied as a powerful top-down strategy to fine-tune surface structure, generate high densities of catalytically active sites, and fabricate flexible, binder-free electrodes [31,32,42,43]. Moreover, cathodic corrosion has emerged as a versatile synthetic route applicable to a broad range of metals and alloys, enabling the preparation of clean metal, metal oxide, or alloy nanoparticles, as well as single-atom catalysts, without the use of surfactants or chemical reducing agents [44–48]. Therefore, an in-depth understanding of cathodic corrosion and the subsequent structural changes of metal surfaces/electrodes is of central importance for research, development, and technological applications. While a recent review has addressed cathodic corrosion primarily in the context of electro-organic synthesis in organic electrolytes [41], the present review extends beyond this scope by integrating fundamental mechanistic insights with applications in electrocatalyst fabrication and performance optimization. The principles outlined herein provide guidelines for the rational electrochemical design of metal electrodes with tailored surface structures, with implications for electroanalytical chemistry, bioelectrochemistry, energy conversion and storage, spectroelectrochemistry, and materials science.

2. Structure–activity relationships in electrocatalysis

The electrocatalytic performance strongly depends on the surface structure, underscoring the importance of rigorously establishing structure–activity relationships across different electrode materials. A key challenge lies not in recognizing the importance of surface structure, but in disentangling the contributions of distinct atomic-scale motifs such as terraces, steps, defects, grain boundaries, and compositional heterogeneities from the ensemble-averaged response of extended metal electrodes. In this regard, the use of well-defined model surfaces of single-crystal electrodes is essential to understand the influence of surface structure on electrocatalytic reaction kinetics and to elucidate their reaction mechanisms and product selectivity, all of which can vary markedly with surface orientation and coordination environment [23,49–55]. Furthermore, the simplicity of single-crystal surfaces permits the direct comparison of the experiments with theoretical calculations [56]. However, translating such insights to nanostructured and polycrystalline electrocatalysts remains nontrivial, as practical electrodes introduce additional complexities, including size effects, interparticle interactions, grain boundaries, and dynamic surface evolution under reaction conditions.

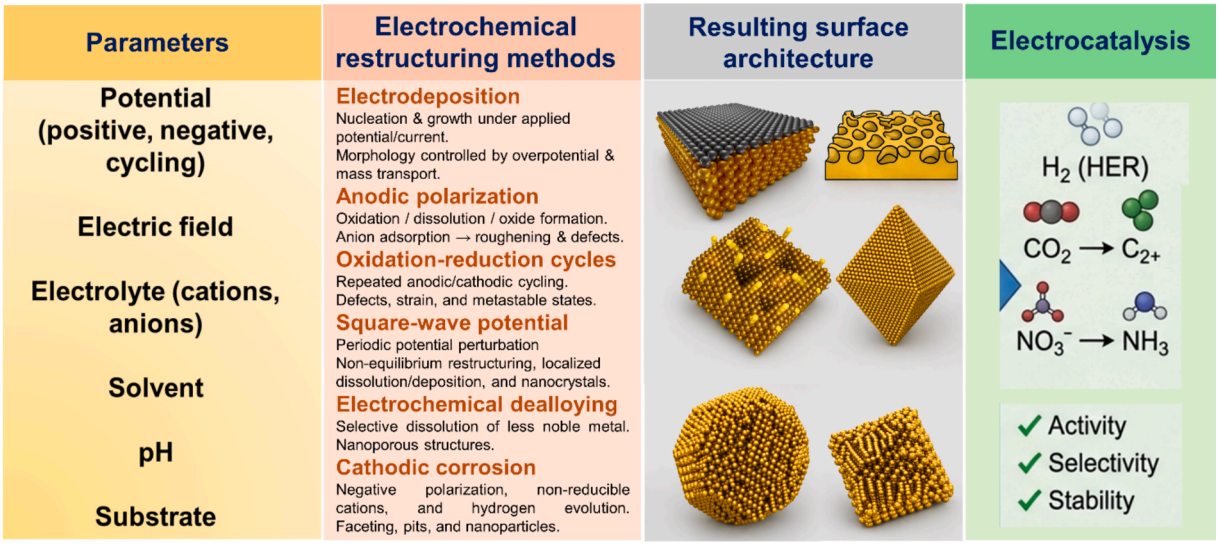

Fig. 1. Key electrochemical approaches for restructuring metal surfaces.

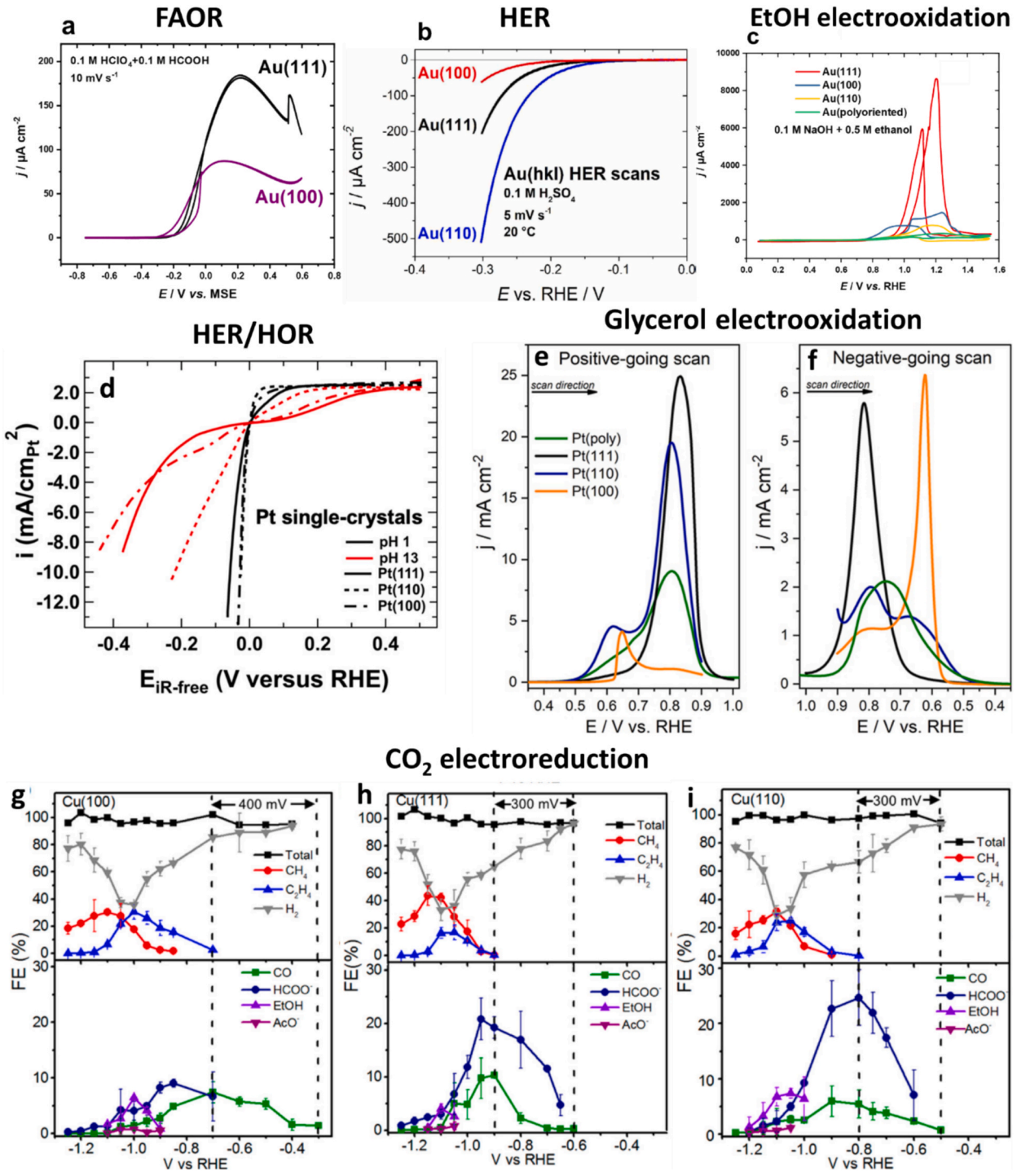

Fig. 2. Electrocatalytic structure-sensitive reactions on single crystal surfaces. Current–potential curves of (a) FAOR on Au(100) and Au(111) electrodes, (b) HER on Au(100), Au(111) and Au(110) and (c) ethanol oxidation on Au(111), Au(100), Au(110) and Au(polyoriented) electrodes. (d) HER/HOR polarization curves of Pt single crystals in H_2-saturated electrolytes. (e) Positive-going scan and (f) negative scan of the 1st cycle of electrooxidation of glycerol at different surfaces of Pt electrodes. Faradaic efficiencies of CO_2 electroreduction products formed on (g) Cu(100), (h) Cu(111), and (i) Cu(110) surfaces. The dashed lines mark the onset potentials for CO and C_2H_4 formation on the three surfaces.
Reproduced with permission from [50,51,69–71].

Recent advances in experimental methodologies have begun to bridge the gap between single-crystal studies and realistic electrocatalysts by enabling spatially resolved correlations between local surface structure and electrochemical activity at the nanoscale [12,57,58]. These approaches build directly upon the fundamental knowledge derived from single-crystal electrodes, translating facet-, step-, and defect-specific reactivity into nanoscale structure–function relationships applicable to nanostructured and polycrystalline materials. Within this conceptual framework, complex electrode surfaces are viewed as assemblies of simpler structural motifs, each characterized by a distinct intrinsic reactivity inherited from well-defined single-crystal models. Consequently, structure–activity relationships emerge not as single, static descriptors, but as evolving distributions that depend on electrode morphology, composition, and electrochemical history. In the following subsections, we discuss how these ideas have been developed and refined. Section 2.1 examines insights obtained from single-crystal electrodes as archetypal systems for probing intrinsic structure sensitivity. Section 2.2 addresses strategies for bridging single-crystal concepts with nanoparticle and polycrystalline electrocatalysts, emphasizing the role of heterogeneity and scale. We highlight representative electrocatalytic reactions on various metal surfaces, highlighting structure-sensitive processes and illustrating how surface structure governs reaction pathways, kinetics, and selectivity.

2.1. Insights from single-crystal electrodes

Well-defined single-crystal electrodes with long-range atomic order have long served as benchmark systems for elucidating intrinsic structure–activity relationships in electrocatalysis [23,49–55]. By exposing a single crystallographic orientation under thoroughly controlled conditions, these model surfaces enable the isolation of specific surface sites, including terraces, steps, and kinks, and their direct correlation with electrocatalytic reactivity. In particular, low Miller index planes of face-centered cubic (FCC) metals, namely (111), (100), and (110), provide atomically periodic surfaces with well-defined coordination environments, making them ideal platforms for fundamental mechanistic investigations.

Of note, the validity of structure–activity relationships derived from single-crystal studies critically depends on rigorous surface preparation and characterization to obtain clean and well-ordered model surfaces, respectively [52,59]. Atomic-scale structural order is commonly verified using surface-sensitive techniques such as low-energy electron diffraction (LEED), scanning tunneling microscopy (STM), and surface X-ray scattering [54,60–64]. In electrochemical environments, cyclic voltammetry provides characteristic "fingerprints" of surface orientation through features associated with hydrogen adsorption/desorption, anion adsorption, or surface reconstruction [52,65–67]. Complementary electrochemical probes, including electrocatalytic reaction, underpotential deposition (UPD) of metal adlayers, and CO stripping voltammetry, are routinely used to quantify surface site distributions and electrochemically active surface areas [32,68]. Together, these techniques ensure that observed electrocatalytic trends can be confidently attributed to well-defined surface structures rather than uncontrolled heterogeneity.

Most noble metals adopt an FCC lattice and can be systematically represented within a stereographic triangle, where the basal planes occupy the vertices and stepped surfaces appear along the edges [21]. The three low-index facets differ markedly in surface atom coordination numbers, with 9 for (1 1 1), 8 for (1 0 0), and 7 for (1 1 0), resulting in distinct electronic structures and adsorption energetics. These differences manifest directly in electrocatalytic behavior, as demonstrated across a wide range of reactions. Although single-crystal electrodes are not practically deployable in industrial electrocatalysis, the knowledge they provide is indispensable for rationalizing the behavior of structurally complex catalysts such as nanoparticles and polycrystalline electrodes.

In this context, macroscopic electrochemical measurements on single-crystal surfaces have revealed pronounced structure sensitivity for many reactions. Fig. 2a-i displays various electrocatalytic reactions, which have been studied on single-crystal surfaces [50,51,69–71]. Interestingly, the surface structure affects the reactivity of Au electrodes towards the hydrogen evolution reaction (HER), formic acid oxidation reaction (FAOR), and methanol electro-oxidation; however, different trends are observed as a function of the electrocatalytic reaction (Fig. 2a-c). As can be seen in Fig. 2a, the electrocatalytic activity of the Au(111) electrode at high potentials is significantly higher than that of Au(100) for FAOR in acidic media. Furthermore, a marked step-up toward higher current values (kink) in the voltammogram for FAOR on Au(111) appears around 0.5 V *vs.* MSE for both sweep directions, which is a specific feature of large and well-ordered Au(111) single crystal surfaces (Fig. 2a) [72]. In comparison, the electrocatalytic activity increases in the order of Au(110) > Au(111) > Au(100), measured under clean conditions and for thermally reconstructed surfaces toward HER in acidic media (Fig. 2b) [69]. For the electrooxidation of ethanol in alkaline media, even though the onset of oxidation is similar for the three basal planes, the catalytic activity of the Au(111) electrode at high potentials is considerably higher than on Au(100), while the Au(110) displays the lowest activity (Fig. 2c) [71].

Furthermore, Pt single-crystal electrodes have been extensively employed to investigate numerous electrocatalytic reactions, including but not limited to the HER, hydrogen oxidation reaction (HOR), and glycerol electrooxidation [51,70]. The HER/HOR polarization curves in 0.1 M $HClO_4$ (pH = 1) and 0.1 M KOH (pH = 13) electrolytes at 20 mV s^{-1} for different Pt single crystal surfaces are shown in Fig. 2d [70]. The HER and HOR kinetics of all Pt surfaces decrease with increasing pH. The comparison highlights that the activity for the HER on Pt(hkl) is comparable in acidic media, but it increases in the sequence (111) < (100) < (110) in alkaline media. To explain, the overall reaction kinetics are influenced by an interplay of factors involving the electrode, electrolyte, and the electrode/electrolyte interface. In this regard, it is well-known that the HER/HOR kinetics in acid correlate with the hydrogen binding energy of the electrode. Furthermore, understanding surface and solvent effects related to the electrode/electrolyte interface is thus required for interpreting such deviations between the activity as a function of electrolyte pH. Research conducted by the Yan [73,74] as well as Koper and Janik [75,76] groups has demonstrated a major difference in the surface environment during the HER/HOR at low and high pH. The increased presence of surface co-adsorbates at high pH has been identified as a key factor. While the specific identity and coverage of these co-adsorbed species, whether H_2O_{ad} or OH_{ad}, with or without near-surface alkali cations, remain subjects of ongoing debate, it is widely acknowledged that their existence contributes to the non-Nernstian pH dependence. Consequently, a

comprehensive understanding of the HER/HOR mechanism necessitates the consideration of co-adsorbates, in addition to other thermodynamic descriptors and changes to intrinsic kinetic parameters.

The electrocatalytic behavior for glycerol electrooxidation was investigated by comparing current–potential curves in both forward and backward scans for Pt single crystal electrodes and polycrystalline Pt electrodes in 0.1 M NaOH + 0.1 M glycerol at a scan rate of 10 mV s^{-1}, as depicted in Fig. 2e and 2f [51]. Each of the three Pt single-crystal model electrodes exhibits different electrocatalytic activity towards glycerol electrooxidation. The observed onset potential for the Pt single crystal electrodes follows the sequence: Pt (110) < Pt(100) < Pt(111). This suggests that the onset potential for each surface orientation depends on the nature of the adsorbed species (O-containing species) and their bonding to the surface sites, influenced by the atomic arrangement. As the electrode potential becomes positive, the faradaic current related to glycerol electrooxidation rises, with all electrodes showing at least one oxidation peak, except Pt(110). Among the Pt basal planes, the Pt(111) electrode exhibits the highest activity, followed by the Pt(110) and Pt (100). However, this feature is valid only for the first voltammetric cycle. The electrode deactivation under successive potential scans is a characteristic feature of the Pt electrocatalysis towards the oxidation of small organic molecules, particularly in alkaline media [77]. Another distinct feature is the trend in current densities during the negative-going scan. At the beginning of the negative-going scan, surface sites are significantly occupied due to oxide growth formed at high positive potentials. Surface reactivation occurs during the negative scan as the oxide gradually reduces, cleaning the surface. However, current densities are lower than those in the positive-going scan. The hysteresis observed between positive and negative-going scans during glycerol electrooxidation indicates mechanistic aspects of the reaction. This is mainly related to the formation of strongly adsorbed intermediates, suggesting that during glycerol oxidation, the formation of these adsorbed residues plays a significant role in the process. Once formed during the positive-going scan, some species remain adsorbed within the potential window during the reverse sweep due to strong coordination to the surface sites and/or slow oxidation kinetics.

Significantly, the surface structure of metal electrodes not only influences their electrocatalytic activity but also plays a crucial role in determining selectivity towards specific products, as observed in reactions such as CO_2 electroreduction. The Faradaic efficiencies of products formed during CO_2 electroreduction on Cu single crystal electrodes at various electrochemical potentials have been previously investigated, as shown in Fig. 2g-i [50]. The primary products detected include CO, formate, CH_4, C_2H_4, ethanol, and H_2, each exhibiting distinct faradic efficiencies and onset potentials, which both depend on the surface orientation of Cu electrodes. A minor amount of acetate (FE < 2%) is also observed on Cu single crystals. The onset potentials for C_2H_4 and CO production are closely related, with Cu(100) exhibiting the lowest onset potential for CO (−0.3 V) and C_2H_4 (−0.7 V *vs.* RHE) formation, while Cu(111) demonstrates the much higher onset potentials for CO (−0.6 V) and C_2H_4 (−0.9 V) production. Notably, across all Cu single crystals, the onset of

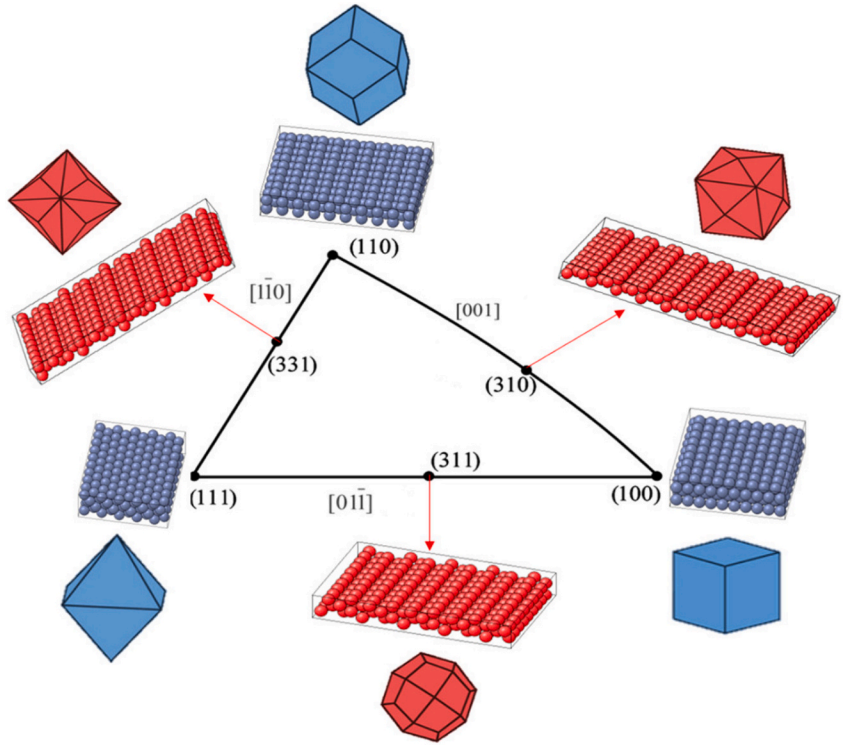

Fig. 3. Stereographic triangle projection of FCC single-crystal surfaces, along with the corresponding model of the surface atomic arrangements and polyhedral nanocrystals bounded by the related crystal planes. Low-index facets and their associated polyhedra are highlighted in blue, while high-index facets and their corresponding polyhedra are distinguished in red.
Reproduced with permission from [21]

C_2H_4 formation consistently occurs at 300–400 mV more negatively than the onset of CO formation. Collectively, such studies help to identify and quantify the structural sensitivity, which varies according to the reaction of interest, the working electrode, and the electrolyte composition [23,49,53,69].

2.2. Bridging single-crystal and nanoparticle electrocatalysis

While single-crystal electrodes provide supreme mechanistic insight, practical electrocatalysts are typically nanostructured and structurally heterogeneous. Bridging the gap between these two regimes has therefore become a central objective in electrocatalysis research. A key strategy toward this goal is the synthesis of shape-controlled metal nanoparticles whose exposed facets mimic the crystallographic orientations of single-crystal surfaces [12,22,24,78–81].

In analogy with the stereographic triangle for single-crystal surfaces, nanocrystals are also illustrated in order to associate the crystal surface index and the nanoparticle (NP) shape (Fig. 3). At the vertex of the triangle, NPs with low-index facets bonded by basal facets are exhibited, *i.e.*, octahedral with (111) facets, nanocubes with (100) facets, and rhombic dodecahedra with (110) facets, while at the edges, one can see NPs with high-index surface facets.

Numerous studies demonstrate that nanoparticles enriched in specific facets reproduce trends observed on single-crystal electrodes. Fig. 4a shows a comparison of the transient current density of FAOR at 0.25 V *vs.* SCE on the tetrahexahedral (THH) Pt

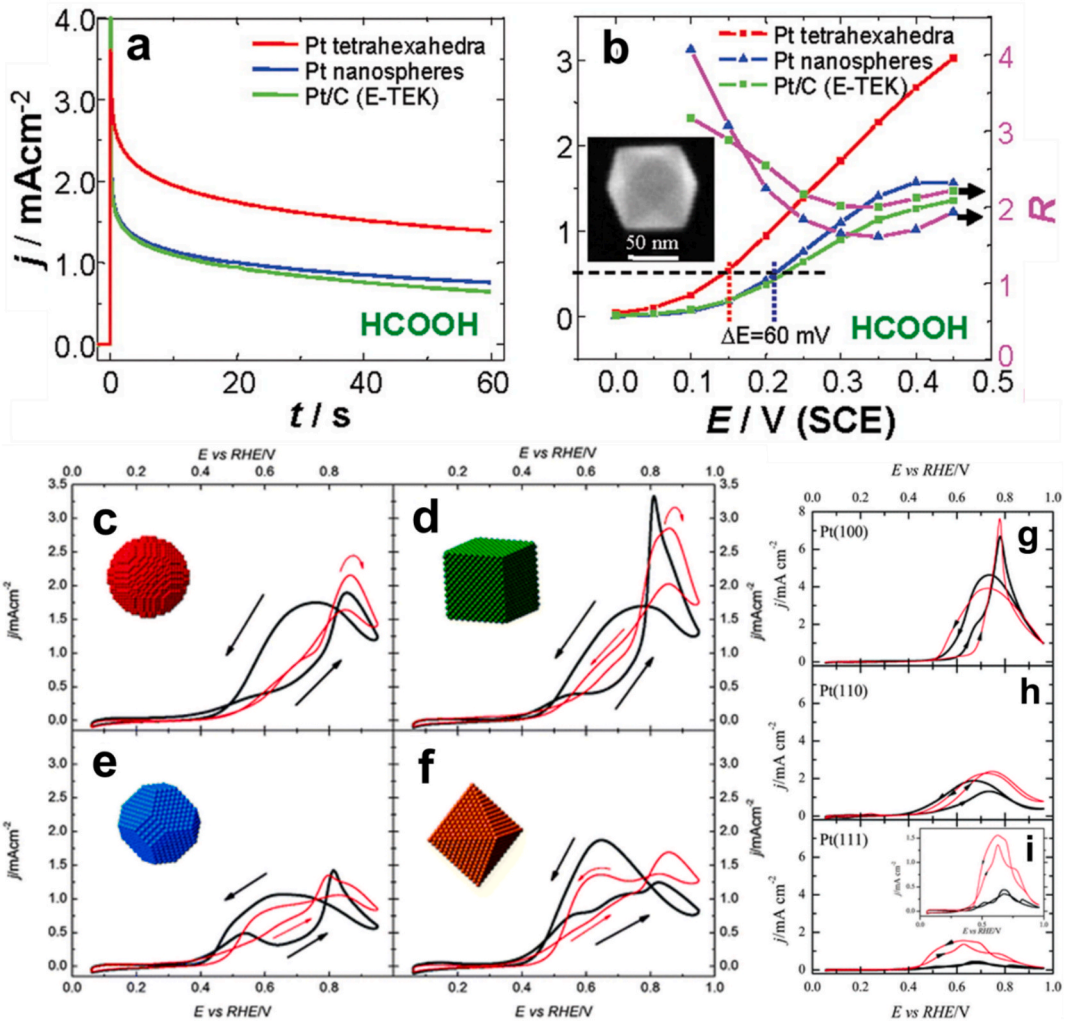

Fig. 4. Comparison of electrocatalytic activity between differently shaped Pt nanoparticles. (a) Transient current density curves of FAOR at 0.25 V. (b) Potential-dependent steady-state current density (left, recorded at 60 s) of FAOR on THH Pt, Pt nanospheres, and Pt/C catalyst, and the ratios R (right) between that of THH with the latter two, respectively. Ethanol electrooxidation (1st cycle) on (c) Pt(poly), (d) Pt(100), (e) Pt(100)–(111) and (f) Pt (111) nanoparticles as well as on (g) Pt(100), (h) Pt(110) and (i) Pt(111) single crystals in 0.5 M H_2SO_4 + 0.2 M CH_3CH_2OH (black line) and 0.1 M $HClO_4$ + 0.2 M CH_3CH_2OH (red line) at 50 mV s^{-1}.
Reproduced with permission from [22,81].

nanocrystals (mean diameter = 81 nm), the electrodeposited polycrystalline Pt nanospheres (mean diameter = 115 nm), and the commercial 3.2 nm Pt/C electrocatalyst at room temperature in acidic electrolyte [81]. The oxidation current is normalized to the EASA of Pt so that the current density can be directly used to compare the electrocatalytic activity of different electrocatalysts. The oxidation current density on THH Pt nanocrystals is nearly double that on Pt nanospheres or Pt/C electrocatalyst. Moreover, the potential dependence of the steady-state current density recorded at 60 s is shown in Fig. 4b. The current density of FAOR on THH Pt nanocrystals is higher than that on the Pt nanospheres or the Pt/C electrocatalyst, and the enhancement factor (R), which is defined as the ratio of the current density measured on THH Pt nanocrystals versus that achieved on Pt nanospheres or Pt/C electrocatalyst, varies from 160% to 400% for Pt nanospheres and from 200% to 310% for Pt/C electrocatalyst, depending on electrode potential. The superior electrocatalytic activity of THH Pt nanocrystals may be attributed to the high density of stepped atoms on the surfaces of the nanocrystals.

In another illustrative example, Fig. 4c-i shows the voltammetric profiles for the ethanol electrooxidation (first cycle) on different shapes of Pt nanoparticles compared to Pt(111), Pt(110), and Pt(100) single crystals in 0.2 M CH_3CH_2OH + 0.5 M H_2SO_4 and 0.2 M CH_3CH_2OH + 0.1 M $HClO_4$ at 50 mV s^{-1} [22]. In all cases, the voltammetric profiles show an oxidation peak at 0.8–0.85 V *vs.* RHE in

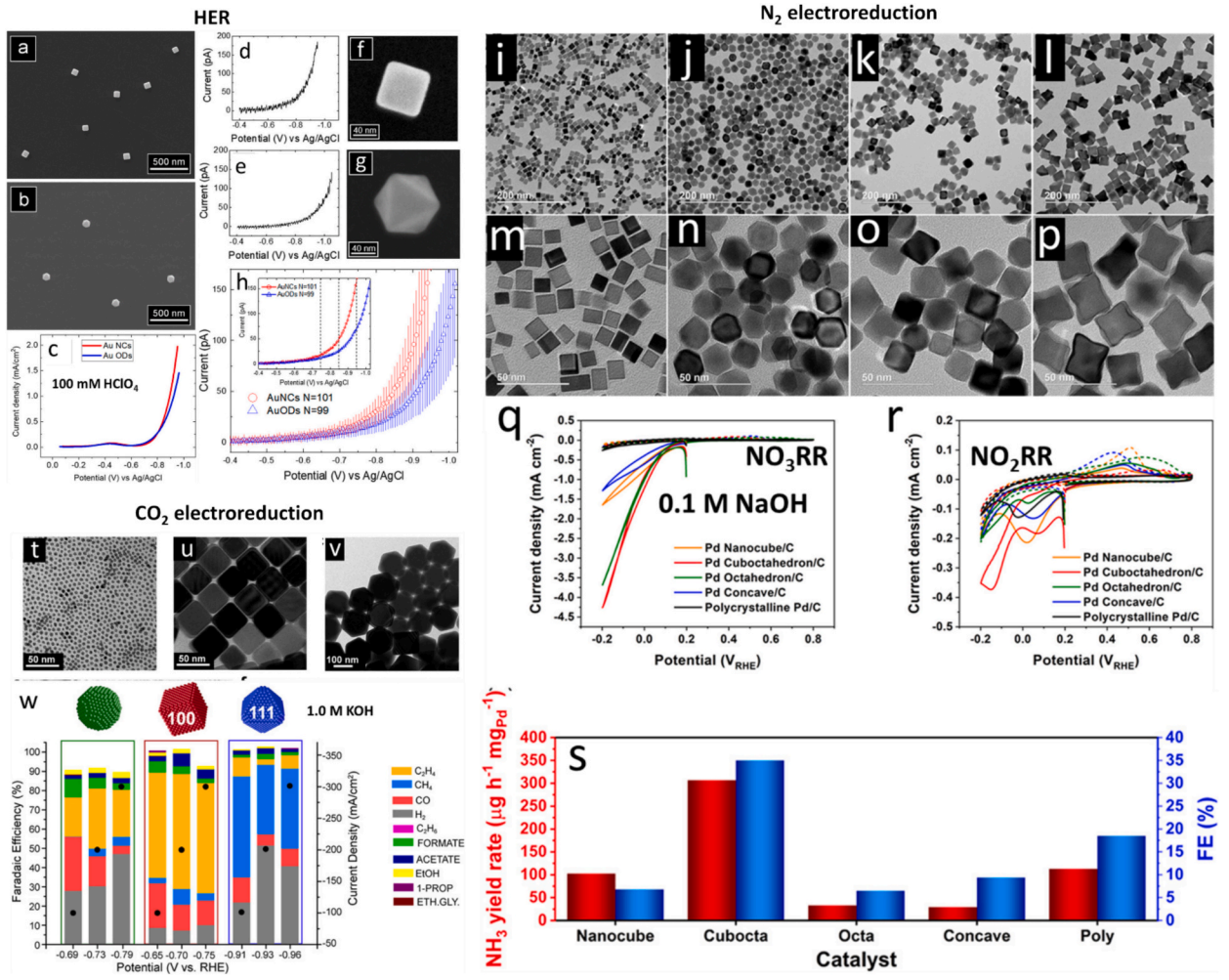

Fig. 5. Impact of nanoparticle shape and morphology on electrocatalytic performance across different metals. SEM micrographs of (a) Au NCs and (b) Au ODs employed for (c) macroscale LSVs for HER. The HER activity for a single particle of (d) Au NC and (e) Au OD. The corresponding high-resolution SEM micrographs are shown in (f) and (g), respectively. (h) Averaged HER response at individual Au NC (n = 101) and Au OD (n = 99). Inset: Same averaged profiles without standard deviation error bars. The cyclic voltammetry profiles for single particles are recorded in aqueous 100 mM $HClO_4$ at a scan rate of 1 V s^{-1}. TEM images of Pd shape-controlled nanoparticles. (i,m) Pd nanocube, (j, n) Pd cuboctahedron, (k,o) Pd octahedron, and (l,p) Pd concave nanocube. Electrochemical activity of (q) NO_3RR and (r) NO_2RR for all Pd catalysts over HER. Dash lines are blank cyclic voltammetry tests for all Pd catalysts at Ar-saturated 0.1 M NaOH in the absence of 20 mM NO_3^- or 2 mM NO_2^-, whereas solid lines are cyclic voltammetry tests at Ar-saturated 0.1 M NaOH in the presence of 20 mM NO_3^- or 2 mM NO_2^-. (s) NH_3 yield rate at 3 h and faradaic efficiency of all Pd catalysts. TEM images of the as-synthesized (t) Cu spheres, (u) Cu cubes, and (v) Cu octahedra. (w) Faradaic efficiencies of CO_2 electroreduction products formed on the Cu catalysts measured in the gas-fed flow cell in 1 M KOH.
Reproduced with permission from [82–84]

the positive scan and higher oxidation currents in the negative scan. For the Pt(100) nanoparticles (Fig. 4d), a prominent peak in the positive scan at 0.8–0.85 V *vs.* RHE is obtained, which is associated with the oxidation of the CO layer formed due to the cleavage of the C–C bond at low potentials and the reactivation of the surface for the oxidation of ethanol. This behaviour is comparable to that typically observed for the Pt(100) single crystal (Fig. 4g). This type of contribution is absent in the other two basal planes (110) and (111) (Fig. 4h and 4i). Therefore, the peak observed for the Pt nanoparticles at this potential is then clearly related to the presence of (100) domains on the nanoparticles. As expected, the current density is maximum for the Pt(100) nanoparticles, whereas Pt(111) nanoparticles, which have a very low amount of (100) ordered domains on the surface, show the lowest current density in this potential region (Fig. 4f). In addition, Pt (poly) and Pt(100)–(111) nanoparticles, which have an intermediate amount of (100) ordered domains, have intermediate current values in this potential region (Fig. 3d and 3e).

Advances in spatially resolved electrochemical techniques have further strengthened the bridge between model and realistic systems. Scanning electrochemical cell microscopy (SECCM) has enabled direct measurements of electrocatalytic activity at the level of individual nanoparticles. Electrocatalytic HER at individual faceted Au nanocubes (NCs) and nano-octahedra (ODs) expressing predominantly (100) and (111) crystal planes on the surface, respectively, were studied by SECCM [82]. Scanning electron microscopy (SEM) images of Au NCs (edge length of ~78 nm) and Au ODs (edge length of ~99 nm) are illustrated in Fig. 5a and 5b, respectively. Macroscopic linear sweep voltammogram (LSV) measurements in 100 mM $HClO_4$ at a scan rate of 50 mV s^{-1} were conducted to compare the HER activity between Au NCs and Au ODs (Fig. 5c). The results indicated that Au NCs achieve a current density of 1 mA cm^{-2} at a potential approximately 30 mV more positive than that of Au ODs, indicating more favorable kinetics for Au NCs (Fig. 5c). To gain a deeper understanding of the HER activity at the single-particle level, the authors conducted SECCM studies for Au NCs and Au ODs. Cyclic voltammogram maps were generated by sweeping the potential at each pixel from −0.4 to −0.95 V *vs.* Ag/AgCl at a scan rate of 1 V s^{-1}. Notably, the electrocatalytic activity observed at the single Au NP level mirrored the macroscopic measurements, reaffirming that HER activity is higher for Au NCs than Au ODs. Importantly, the difference in electrocatalytic activity between Au NCs and Au ODs is more pronounced in the single-particle measurements than in the macroscale measurements, providing novel insights into the quantification of a nanocrystal's catalytic activity.

The impact of the surface structure of Pd NPs with well-defined shapes on nitrate and nitrite reduction has been thoroughly examined, shedding light on the role that catalyst structural design plays in enabling the selective reduction of nitrate to ammonia (Fig. 5i-s) [83]. The Pd shape-controlled nanoparticles investigated include a Pd nanocube enclosed by six (100) facets with an average edge length of 13.0 nm, a Pd cuboctahedron containing six (100) and eight (111) facets with an average edge length of 20.5 nm, a Pd octahedron with eight (111) facets and an average edge length of 21.9 nm, and a Pd concave nanocube with (100) facets at the terrace and high-index (hk0) facets such as (730) at the edges/vertex, possessing an average edge length of 19.0 nm (Fig. 5i-p). The electrochemical activities for the nitrate reduction reaction (NO_3RR), the rate-determining step, and nitrite reduction reaction (NO_2RR), the selectivity-determining step, were assessed by cyclic voltammetry in 0.1 M NaOH (Fig. 5q and 5r). Blank cyclic voltammetric profiles in the absence of reactants were measured in an Ar-saturated 0.1 M NaOH electrolyte, showing low current densities (~0.2 mA cm^{-2} at −0.2 V *vs*. RHE) primarily due to the HER. The electrochemical NO_3RR activity of all Pd catalysts was evaluated in the presence of nitrate ions (20 mM NO_3^-). The Pd cuboctahedron/C exhibited the highest NO_3RR activity, followed by Pd octahedron/C, Pd nanocube/C, Pd concave/C, and polycrystalline Pd/C. The order of electrochemical activity toward NO_3RR was attributed to the presence of eight (111) facets, which are absent in the nanocube and concave cube. Furthermore, the electrochemical NO_2RR activities of all shape-controlled Pd/C in the presence of nitrite ions (2 mM NO_2^-) were measured, indicating that the Pd nanocube/C exhibits the highest NO_2RR activity, followed by Pd cuboctahedron/C, Pd concave/C, polycrystalline Pd/C, and Pd octahedron/C. The results highlighted the critical role of the (100) facet, suggesting higher NO2RR activity than Pd(111) or Pd(hk0). The NH_3 yield rate at 3 h and the faradaic efficiency of all Pd catalysts were also evaluated (Fig. 5s). Notably, Pd cuboctahedron/C demonstrates the highest NH_3 yield rate and faradaic efficiency compared to other catalysts, showcasing its bifunctional nature with the (111) facet catalyzing the conversion of NO_3^- to NO_2^- and the (100) facet catalyzing the conversion of NO_2^- to NH_3.

Facet-dependent activity and selectivity of differently shaped Cu nanoparticles are compared towards CO_2 electrochemical reduction (CO_2RR) under commercially relevant current densities in a gas-fed flow cell [84]. Fig. 5t–v demonstrates the transmission electron microscopy (TEM) images of the as-obtained Cu spheres of 6 nm, Cu cubes of 44 nm with (100) facets, and Cu octahedra of 150 nm with (111) facets, which all possess high uniformity in size and shape. Fig. 5w illustrates the faradaic efficiencies for the three CuNCs in the gas-fed flow cell, along with current densities normalized by the EASA. In summary, the Cu cubes exhibit high selectivity toward C_2H_4 (57%), the Cu octahedra show selectivity toward CH_4 (51%), and the Cu spheres do not display selectivity toward any specific product in a 1 M KOH electrolyte.

Recognizing that electrocatalysts may undergo structural transformations during electrocatalytic reactions, we discuss the potential structure changes in the next section. The focus is primarily on Au surfaces due to their exceptional properties, relative ease of preparation, and high stability in terms of superior resistance to oxidation and dissolution, making them a model example to illustrate the possible structure changes during electrocatalytic reactions.

Together, shape-controlled nanoparticle studies provide compelling evidence that concepts derived from single-crystal electrocatalysis remain relevant at the nanoscale. At the same time, they emphasize that additional factors such as particle size, interparticle interactions, support effects, and local mass transport must be considered when extrapolating single-crystal insights to practical catalysts.

2.3. Dynamic structure sensitivity

Importantly, structure–activity relationships in electrocatalysis are not necessarily static. Induced by the applied potential,

electrode surfaces may undergo reconstruction/restructuring, adsorbate-induced segregation processes, oxidation–reduction cycling, dissolution–redeposition, or defect generation, leading to continuous evolution of the electrocatalytically active surface. Consequently, the surface structure probed *ex situ* or under idealized conditions may differ substantially from the surface structure operative during electrocatalysis. This dynamic nature of electrocatalyst surfaces provides a natural bridge to the next section of this review, which focuses on electrochemical restructuring processes and their deliberate exploitation for tailoring free-standing electrocatalysts.

3. Stability considerations of metal electrodes

Electrochemical reactions are essentially constrained by the thermodynamic stability window of the electrolyte. Once the applied potential approaches or exceeds this window, electrolysis of the solvent or electrolyte components becomes unavoidable, generating gas evolution and highly reactive interfacial species [85]. While electrolyte decomposition is widely recognized and often treated as an operational boundary, the concurrent response of the electrode itself is frequently overlooked. In applied technologies, electrolysis conditions impose severe chemical and mechanical stresses on electrode materials, driving dissolution, redox cycling, surface restructuring, and morphological evolution [86]. These transformations can fundamentally modify the active surface, thereby altering apparent catalytic activity, selectivity, and stability. Electrode stability must therefore be viewed not as a static material property, but as a dynamic consequence of electrolysis-driven interfacial processes during operation.

From a materials science perspective, electrode stability is not merely the absence of dissolution, but the ability of a surface to preserve or controllably evolve its atomic structure under electrochemical driving forces. Electrochemical potentials act as external thermodynamic variables that continuously reshape surface structure. The stability of metal electrode surfaces in contact with an electrolyte strongly depends on the applied potential, the electrolyte composition, the electrolyte pH, and the reaction of interest [87–90]. Fig. 6 schematically illustrates the various electrochemical processes that can induce various changes in the surface structure of Au electrodes and the relevant structures depending on the applied potentials. The positions of surface atoms vary from the bulk due to the broken symmetry and the broken bonds. The modifications are termed relaxations if the surface unit cell remains truncated compared to the bulk. However, if the surface unit cell is different, then the resultant changes in the structure are referred to as reconstruction [91]. Most 5d-transition metals, such as Ir, Pt, and Au, undergo surface reconstruction [91,92]. In this respect, the reconstructed surface plane contains a higher atom density per unit area compared to an unreconstructed surface. The underlying principle driving this reconstruction seems to be the compensation of the coordination loss caused by the "broken bonds" at the surface by increasing the effective coordination within the surface plane [91–93].

In an electrochemical environment, the reconstructed surfaces tend to be stable at potentials negative to the potential of zero charge (pzc). A negative surface charge encourages the reconstruction of a surface, while a positive surface charge induces the lifting of reconstruction, leading to the dominance of an unreconstructed surface [91]. When applying a potential negative of the pzc to an already unreconstructed surface, a potential-induced surface reconstruction can be observed [91–93]. In addition, examples of reconstruction induced by adsorption are also widely recognized [94–97]. Reconstructed surfaces can significantly differ from unreconstructed surfaces in terms of morphology, thermodynamic stability, and electrocatalytic activity [54,93,97,98].

For example, the influence of the applied potential on the surface reconstruction of Au(111) in 0.1 M aqueous H_2SO_4 was investigated within the so-called double-layer region (Fig. 7a-f) [54]. After flame-annealing and immersion of the Au(111) electrode at −0.60 V *vs.* MSE, a thermally reconstructed surface exhibits a herringbone-like structure (Fig. 7a). Stepping the potential to positive values of the pzc, such as 0.09 V, leads to the lifting of surface reconstruction due to specific (bi)sulfate anion adsorption (Fig. 7b,c). This leads to higher defect density and island formation (Fig. 7c). Returning to −0.60 V results in potential-induced surface reconstruction, but to a different degree as a function of time (Fig. 7c-e), leading to the development of a herringbone-like structure distinct from the one observed through thermal reconstruction. Of note, the reconstructed surface of Au(111) displays lower activity towards HER compared to the unreconstructed (1x1) surface (Fig. 7g) [54,93]. This can be attributed to the formation of islands arising from the lifting of reconstruction, which act as active defect sites (Fig. 7b).

On one hand, applying a positive potential greater than the range where the (unreconstructed) surface remains metallic results in

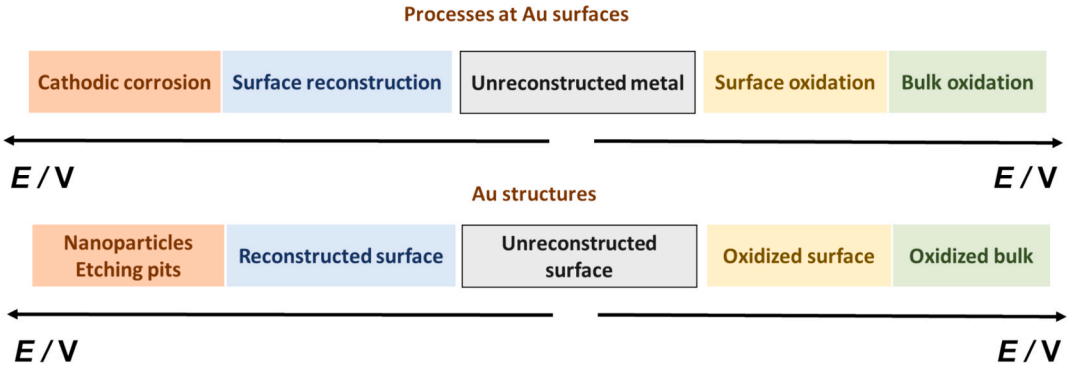

Fig. 6. Schematic illustration of the various electrochemical processes that can induce changes in the surface structure of Au electrodes and the corresponding structures depending on the applied potentials.

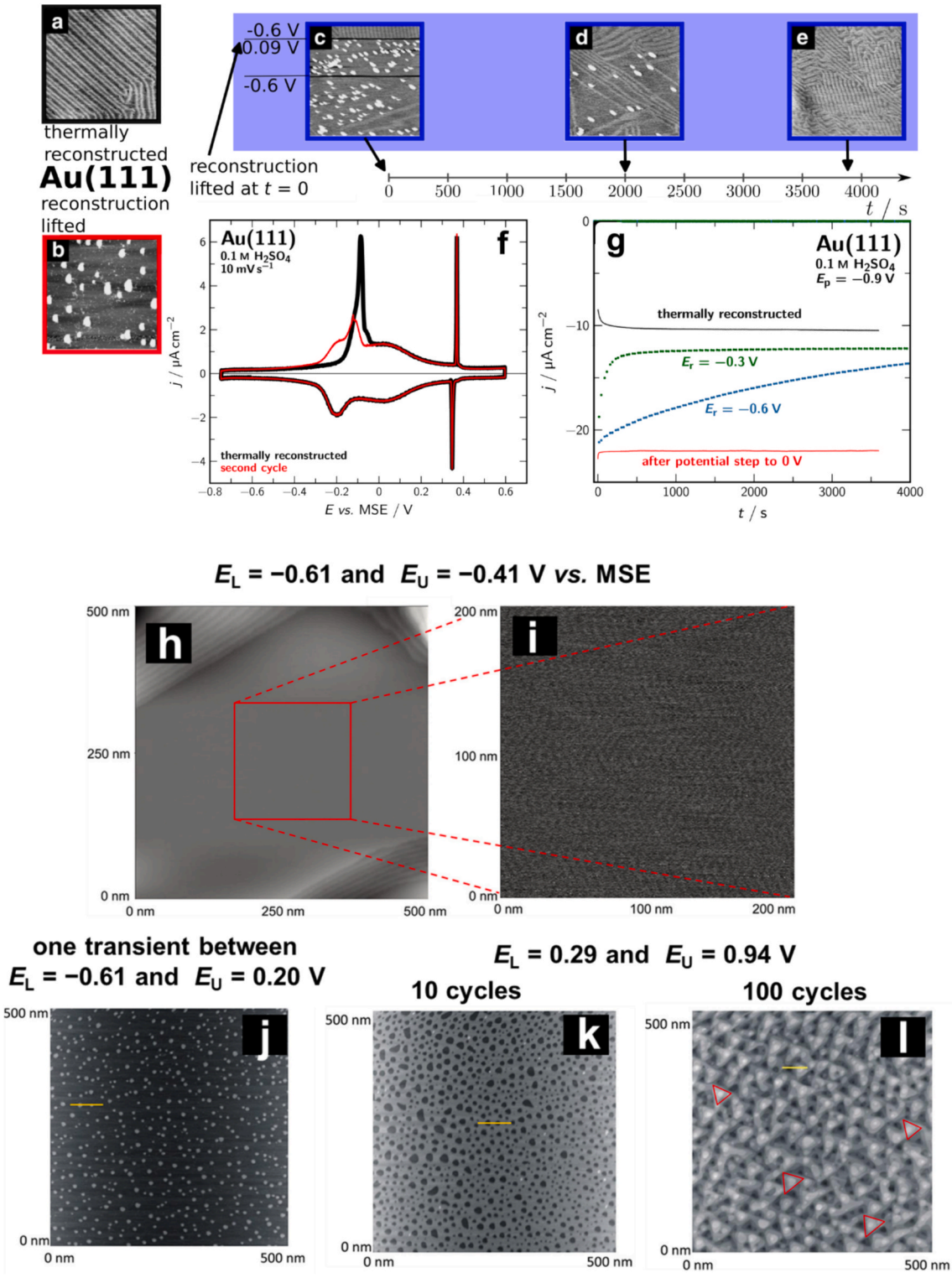

Fig. 7. Potential-induced surface reconstruction of Au(111) revealed by *in-situ* STM. Structural evolution from reconstructed to unreconstructed surfaces ((a–e)) and its dependence on electrochemical history. Corresponding electrochemical signatures ((f,g)) confirm that these transformations directly influence catalytic behavior, emphasizing that the active surface is defined by *operando* conditions. (h–l) demonstrates that surface morphology dynamically responds to applied potential.
Reproduced with permission from [54,63]

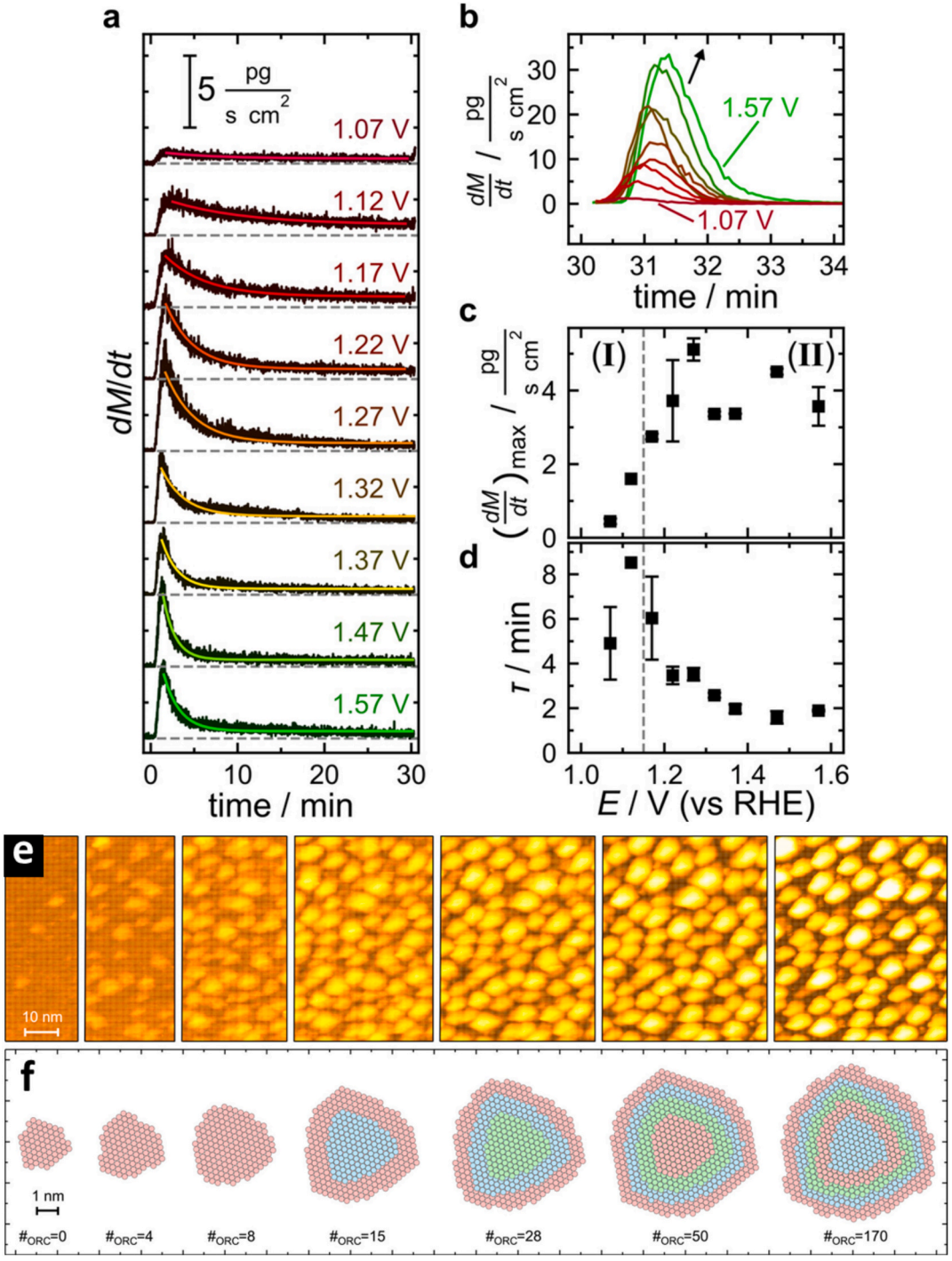

Fig. 8. Platinum dissolution and surface restructuring during oxide formation–reduction cycles. (a) Anodic dissolution rate recorded during a potential sweep (50 mV s^{-1}) from 0.17 V to upper potentials between 1.07 and 1.57 V, followed by a 30 min potential hold. Solid lines represent exponential fits; individual profiles are vertically offset by 5 pg s^{-1} cm^{-2} for clarity. (b) Cathodic dissolution rate during the reverse sweep back to 0.17 V obtained immediately after (a). (c) Maximum dissolution rate $(dM/dt)_{max}$ and (d) decay time constant (τ) extracted from the anodic dissolution transients; error bars denote the standard deviation from 2 to 3 independent measurements. (e) *In-situ* STM images acquired after different oxide formation–reduction cycles, showing progressive surface roughening within the same area (image size: 230 × 230 nm^2). (f) Corresponding average nanoisland structures derived from the *in-situ* STM data, with colors indicating successive atomic layers.
Reproduced with permission from [88,107]

anodic surface oxidation. This process can induce various structural changes such as transformation, facetting, roughening, and even dissolution of metal surfaces [63,87,88,90,99,100]. For instance, consider the case of Au(111) in 0.1 M aqueous H_2SO_4 between the potential range of $E_L = -0.61$ and $E_U = -0.41$ V *vs.* MSE, *in-situ* scanning tunneling microscopy (STM) images show that increasing E_U to 0.20 V *vs.* MSE lifts the herringbone reconstruction and results in round Au clusters (Fig. 7h-j) [63]. When several voltammetric cycles between $E_L = 0.29$ and $E_U = 0.94$ V are applied at a scan rate of $s = 50$ mV s^{-1}, followed by acquiring *in-situ* STM images at $E_L = 0.29$ V *vs.* MSE, to follow the changes in the Au(111) surfaces upon the electrochemical formation and reduction of a surface oxide. As the surface oxide develops, anion desorption occurs; upon reduction of the oxide layer, the anions readsorb. After ten cycles ($n = 10$), the clusters almost vanish, and holes of around 30 nm cover the surface (Fig. 7k). Increasing the cycle number to $n = 100$ produces a distinct pattern resembling a network of interconnected trigonal pyramids (Fig. 7l). These observations of surface roughening and patterning indicate that applying positive potentials sufficient for the oxide formation increases the mobility of Au atoms on the Au (111) surface. Given that numerous electrocatalytic reactions, such as the oxygen evolution reaction (OER) and electrooxidation of organic molecules, occur within these potential regimes, substantial research efforts have been directed towards understanding anodic processes at metal surfaces, encompassing oxidation, surface restructuring, roughening, and dissolution [63,87,88,90,99,100].

An in-depth understanding of the structural changes of metal electrodes upon oxidation or reduction of the surface atoms at a specific potential is crucial for the rational design of active and stable electrocatalysts in the context of a transition towards green technologies. In this context, advances in tools and techniques for *ex-situ* and *in-situ* material characterization, as well as *operando* spectroscopies, have enabled insights, at the atomic and molecular scales, into the transient and steady-state behavior of materials under electrochemical reaction conditions [93,101–104]. Fascinatingly, the electrocatalytic properties of simple electrochemical reactions can unambiguously resolve and characterize the surface structure of metal electrodes in addition to approaches using anion adsorption or electrodeposition of foreign metals, e.g. by underpotential deposition (UPD) [105,106]. In this regard, both FAOR and HER are prominent structure-sensitive model reactions that allow for investigating the structure and dynamics of electrode surfaces [93,103]. For example, the electrocatalytic HER has been employed to probe the kinetics of potential-induced surface reconstruction of Au(111) in contact with either 0.1 M H_2SO_4 or 0.1 M $HClO_4$ [93]. The corresponding current density-time curves in 0.1 M H_2SO_4 are displayed in Fig. 7g. The current densities observed in the potential step series at both −0.3 V and −0.6 V *vs.* MSE exhibit a gradual decline in HER activity over time, indicating structural changes due to potential-induced reconstruction. Similar HER activity to that of the thermally reconstructed surface is not reached in these experiments, as the thermally induced reconstructed surface is quite ordered and shows fewer defect sites than the electrode surface after potential-induced reconstruction. The decline in activity is notably more pronounced for the more positive potential. This observation aligns with *in-situ* STM studies, which have demonstrated that at potentials nearing the point of reconstruction lifting, the reconstruction rows manifest more rapidly within minutes [62]. In addition, FAOR has been used to examine the alterations upon adsorption and self-assembly of the 4-mercaptopyridine on Au(111), as well as to monitor the kinetics of surface oxidation of Au(111) [103,104].

While Au provides an ideal model system for visualizing electrochemical restructuring due to its high resistance to bulk oxidation, platinum represents a technologically critical electrocatalyst for which surface oxidation and dissolution play a decisive role in long-term stability.

The degradation of Pt-based electrocatalysts, particularly under conditions relevant to oxygen reduction reaction (ORR) in fuel cell applications, is closely linked to the electrochemical oxidation and reduction of the Pt surface. A detailed mechanistic understanding of these processes has recently been provided by Fuchs *et al.*, who investigated the surface restructuring and dissolution behavior of a well-defined Pt(100) single-crystal electrode in 0.1 M $HClO_4$ electrolyte. By combining *operando* high-energy surface X-ray diffraction (HESXRD), online mass spectrometry, and density functional theory (DFT), the study resolves the atomic-scale origins of Pt dissolution during electrochemical cycling and reveals that anodic and cathodic dissolution are governed by fundamentally different oxide phases [88].

Fig. 8a shows the anodic Pt dissolution rate measured during a potential sweep from 0.17 V to increasingly positive upper potentials (1.07–1.57 V *vs.* RHE), followed by a potential hold of 30 min. Anodic dissolution is most pronounced during the initial stages of oxide formation and decays exponentially with time at constant potential, as evidenced by the fitted decay curves. This behavior indicates that anodic Pt dissolution is associated with transient surface restructuring during the nucleation and growth of surface oxides rather than with a fully developed, stable oxide layer. The corresponding cathodic dissolution rates measured during the reverse sweep back to 0.17 V are shown in Fig. 8b. Notably, a pronounced cathodic dissolution signal is observed during oxide reduction, demonstrating that Pt dissolution is strongly enhanced under reductive conditions following prior oxidation.

Further quantitative analysis of the anodic dissolution process is presented in Fig. 8c, which summarizes the maximum anodic dissolution rate $(dM/dt)_{max}$ as a function of the upper potential limit. The data reveal that the dissolution amplitude increases with increasing anodic potential until saturation is reached, indicating the formation of a critical oxide coverage beyond which additional oxidation does not further accelerate dissolution. Fig. 8d shows the corresponding time constants (τ) extracted from the exponential decay fits, demonstrating that the kinetics of anodic dissolution become potential independent once this critical oxide coverage is established. Together, these results indicate that surface restructuring and dissolution are governed by oxide phase evolution rather than by the absolute magnitude of the applied potential.

When combined with *operando* structural investigations, these dissolution measurements reveal that anodic and cathodic dissolution originate from different oxide species. Anodic dissolution is predominantly linked to the nucleation and growth of an ordered, stripe-like oxide formed at moderate positive potentials, whereas cathodic dissolution is associated with the reduction of a second, amorphous Pt oxide phase that resembles bulk PtO_2 and develops only after saturation of the stripe-like oxide. Importantly, cathodic dissolution does not occur on pristine metallic Pt but requires prior oxide formation, underscoring the decisive role of electrochemical history.

This study demonstrates that Pt degradation is not a single corrosion process but instead arises from oxide-specific, history-dependent restructuring pathways. Similar to the potential-induced reconstruction observed on Au surfaces, electrochemical cycling continuously reshapes the Pt surface. The results further establish that reductive conditions are not inherently stabilizing and that cathodic dissolution represents a distinct degradation mechanism that must be considered when assessing electrocatalyst stability under realistic operating conditions.

Complementary insight into Pt surface instability is provided by atomic-scale studies of electrochemical roughening, which demonstrate that repeated oxidation–reduction cycles (ORCs) induce irreversible nanoscale restructuring even in the absence of pronounced mass loss [107]. As illustrated by the *in-situ* STM images in Fig. 8e and 8f, successive ORCs lead to the nucleation, growth, and coalescence of nanoscale islands within the same surface region, evidencing progressive roughening driven by electrochemical cycling. The corresponding averaged atomic-scale island structures reveal a layer-by-layer growth mode with increasing structural complexity, indicating that ORCs promote systematic atomic rearrangement. These observations highlight that Pt degradation is not limited to dissolution processes, but also involves continuous morphological evolution that redistributes active sites and alters local coordination environments on experimentally relevant timescales.

Collectively, these results demonstrate that Pt dissolution is not a single corrosion process but instead arises from distinct, oxide-mediated pathways that operate under anodic and cathodic conditions. The study establishes a direct link between surface oxide chemistry, atomic-scale restructuring, and irreversible material loss. From a broader perspective, this behavior closely parallels the potential-driven reconstruction phenomena observed on Au surfaces, while emphasizing that for Pt, electrochemical restructuring is intrinsically coupled to dissolution. These insights underscore that electrode stability is governed by the dynamic evolution of surface oxide phases and electrochemical history, rather than by static thermodynamic considerations alone.

On the other hand, metal electrodes are supposed to remain stable in aqueous electrolytes by lowering the potential relative to the potential regime where the reconstructed surface is dominant, which is known as cathodic protection. In this potential range, the metal's oxidation becomes thermodynamically unfavorable, which might imply that cathodic protection indefinitely stabilizes the metal in its elemental state [108].

However, this assumption is not always correct: under sufficiently negative potentials in the presence of alkali metal cations, metals can experience structural surface transformations and corrosion through a phenomenon referred to as cathodic corrosion, as will be discussed in detail below [41,42,44,109,110].

4. Electrochemical methods for restructuring of metal electrodes

As highlighted in the previous section, various electrochemical treatments can lead to significant changes in the surface structure of metal electrodes. In this regard, several electrochemical strategies have been developed to restructure metal surfaces, enabling the rational tuning of activity, selectivity, and stability across a wide range of electrocatalytic reactions. Fig. 1 presents the key electrochemical methods that can be applied to tailor the surface structure of metallic electrodes [34,109,111–116]. These electrochemical methods can be classified as follows: (i) electrochemical deposition, (ii) anodic polarization, (iii) repetitive oxidation – reduction cycles (ORCs), (iv) square-wave potential program, (v) electrochemical dealloying, and (vi) cathodic corrosion.

Importantly, these approaches should not be viewed as isolated techniques. In practice, they are strongly interconnected: electrodeposited nanostructures may undergo further restructuring during ORCs; dealloying inherently involves repeated oxidation–reduction cycles; and cathodic corrosion can be triggered during aggressive negative polarization following deposition or anodic treatments. Thus, electrochemical restructuring is best understood as a continuum of potential-driven processes, rather than a set of discrete methods.

Compared to conventional electrocatalyst fabrication routes, electrochemical restructuring strategies offer several distinct merits: (i) direct growth of electroactive species on both rigid and flexible substrates, enabling the dispersion of active catalysts and consequently providing a greater abundance of active sites; (ii) elimination of polymeric binders, surfactants, and conductive additives, resulting in homogeneous and clean electrode surfaces, pivotal for achieving higher reproducibility and exposing more catalytically active sites; (iii) the rational design of appropriate nanostructures (1D, 2D, or 3D structures), leading to an enhanced electrochemically active surface area (EASA), swift charge, and mass transport, and superior reaction kinetics; and (iv) robust adhesion of nanostructures that prevents mechanical shedding, enhancing long-term cyclic stability [27,117–120]. In this section, we offer a comprehensive overview, accompanied by examples, of these approaches for restructuring and faceting metal surfaces.

4.1. Electrodeposition

Electrodeposition is one of the most versatile electrochemical strategies for restructuring metal electrodes, enabling precise control over surface composition, crystallography, and morphology through the electrochemical reduction of metal ions followed by electrocrystallization. Depending on the applied potential and electrolyte composition, electrodeposition can proceed via fundamentally different regimes, giving rise to low-dimensional overlayers, atomically dispersed metal species, or three-dimensional nanostructures. As such, electrodeposition provides a direct electrochemical route to generate metal electrodes with tailored atomic-scale structure, morphology, and composition under precisely controlled thermodynamic and kinetic conditions.

A unifying framework for understanding electrodeposition-induced restructuring is the competition between nucleation and growth [111,112,121–123]. In the underpotential deposition (UPD) regime, strong substrate–adatom interactions stabilize metal adlayers at potentials positive of bulk deposition, favoring lateral growth and the formation of atomically thin, two-dimensional structures. In contrast, overpotential deposition (OPD) occurs when the driving force for metal reduction exceeds this stabilization,

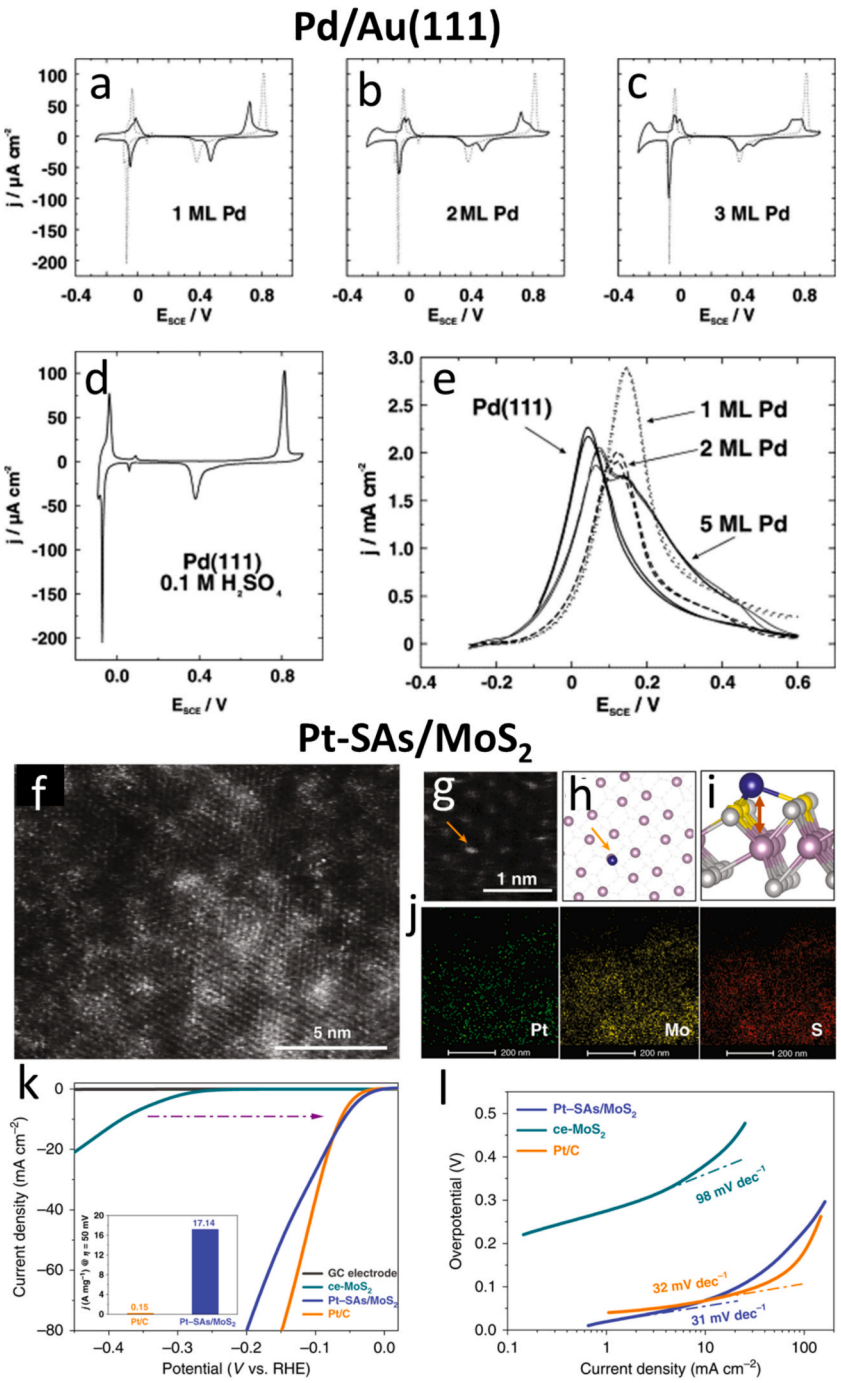

Fig. 9. Atomic-scale control of surface composition via underpotential deposition (UPD). Voltammetric profiles showcasing (a-c) controlled Pd overlayers on Au(111) in 0.1 M H_2SO_4 after deposition from a chloride-containing solution. A reference curve for bulk Pd(111) is represented in (d) and by a dotted line for comparative analysis. (e) Electrocatalytic activity of thin Pd overlayers on Au(111) and massive Pd(111) towards FAOR. UPD approach for atomically dispersed Pt catalysts on MoS_2 substrate. (f) HAADF-STEM image of Pt-SAs/MoS_2. (g) Magnified HAADF-STEM image of Pt-SAs/MoS_2 and its corresponding top (h) and front (i) views of DFT-optimized structural model (purple: Mo; grey: S; yellow: S for the Pt attachment; blue: Pt. (j) Mapping images of Pt, Mo, and S atoms. (k) HER polarization curves of bare, ce-MoS_2-, commercial Pt/C-, and Pt-SAs/MoS_2-covered GC electrodes in 0.5 M H_2SO_4 solution. Inset: the mass activity of Pt-SAs/MoS_2 normalized to the Pt loading at an overpotential of 50 mV *vs.* RHE in comparison with commercial Pt/C. (l) Tafel plots derived from the corresponding polarization curves.
Reproduced with permission from [126,131]

promoting three-dimensional nucleation and growth via Volmer–Weber-type mechanisms [28,111,121,122,124–127]. The balance between nucleation density and growth rate thus dictates whether deposition yields uniform monolayers, isolated nuclei, compact nanoparticles, or highly branched architectures.

Examples of the successful use of the UPD method include the synthesis of a two-dimensional (2D) Pd layer on Au single-crystal electrodes by Kibler et al. [126] as well as the 2D Pt layer on the Au electrode by the quenching effect of underpotential-deposited hydrogen by the Moffat group [128] and of various single-layer core–shell metallic nanostructures by the Adzic group [129]. Such electrochemical systems are of notable significance in the realm of electrocatalysis [124–126,130].

For instance, the electrochemical properties of palladium adlayers on Au(111), which were obtained by electrodeposition from either 0.1 M H_2SO_4 + 0.1 mM $PdCl_2$ + 0.2 mM HCl or 0.1 M H_2SO_4 + 0.1 mM $PdSO_4$ at +0.4 V *vs.* SCE, are compared with those of massive Pd(111) [126]. Cyclic voltammograms for Pd adlayers of 1, 2, and 3 ML thickness on Au(111) in 0.1 M H_2SO_4, deposited from chloride-containing solution, are shown in Fig. 9a-c, which reveal systematic changes with increasing coverage. For comparison, the voltammogram of Pd(111) in sulfuric acid is shown in Fig. 9d and as a dotted line in each frame.

For the first Pd monolayer, there is a complete coverage of the substrate, as indicated by the absence of characteristic peaks of the Au(111) surface (Fig. 9a). Additionally, the hydrogen absorption reaction, occurring at higher overpotentials compared to massive palladium, becomes more prominent as the film thickness increases. The peak for sulfate desorption/hydrogen adsorption in the pseudomorphic Pd monolayer is slightly more positive than that of massive Pd(111). Starting from 2 ML Pd on Au(111), there are two anodic peaks in the hydrogen adsorption range, one at −0.005 V, like for the first Pd monolayer, the other one at −0.035 V corresponding to hydrogen desorption/(bi) sulfate adsorption on massive Pd(111). Thicker Pd deposits exhibit only the latter peak, resembling the behavior of bulk palladium. The altered electrochemical behavior of the overlayer is attributed to changes in the electronic structure induced by lateral strain and the ligand effect. The influence of lateral strain is also explored on the reaction kinetics in the context of FAOR.

The curves in Fig. 9e show the cyclic voltammograms for FAOR on Pd(111) and on the Pd films on Au(111) deposited from chloride solution. The current maxima for a pseudomorphic Pd monolayer on Au(111) and for the massive Pd(111) electrode are located at 0.15 and 0.04 V, respectively (Fig. 9e). Like for hydrogen adsorption, there is a systematic change towards the behaviour of the massive

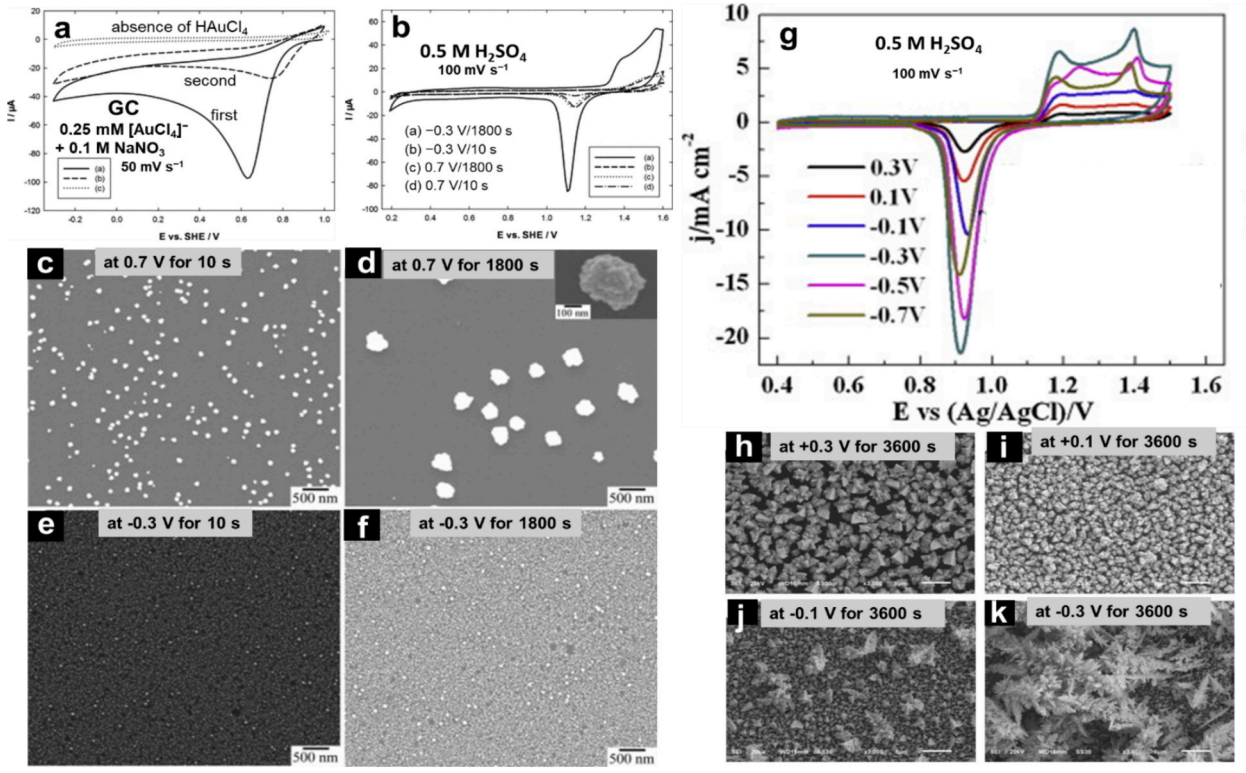

Fig. 10. Morphology control through electrodeposition. (a) Cyclic voltammograms of a GC electrode in a deaerated 0.1 M $NaNO_3$ solution in the presence and absence of 0.25 mM $HAuCl_4$ at 50 mV s^{-1}, (b) Last of the 30 consecutive scans recorded by cyclic voltammograms in a 0.5 M H_2SO_4 on AuNPs-GC electrodes prepared at different conditions. The corresponding SEM images of AuNPs-GC electrodes were synthesized at 0.7 V for (c) 10 s and (d) 1800 s and at −0.3 V *vs.* SHE for (e) 10 s and (f) 1800 s. (g) Cyclic voltammograms of dendrite-like gold nanostructures (DGNs)/GC electrodes under different electrodeposition potentials in a 0.5 M H_2SO_4 solution. The Au nanostructures were electrodeposited from a 0.1 M KCl solution containing 10 mM $HAuCl_4$. Typical SEM images of Au nanostructures electrodeposited for 3600 s at potentials of (h) E = +0.3 V, (i) E = +0.1 V, (j) E = -0.1 V, and (k) E = −0.3 V *vs.* Ag/AgCl.
Reproduced with permission from [134,135]

metal with increasing coverage of Pd on Au(111), the curve for 5 ML having two current peaks for oxidation on strained and unstrained parts of the Pd surface. Differences in the reaction kinetics for FAOR are interpreted in terms of a modified interaction between the Pd surface and the adsorbed species relevant for the rate-determining step, reflecting changes in the electronic structure of the metal overlayer.

Interestingly, beyond the conventional UPD method that produces a 2D single layer, the synthesis of atomically dispersed metal catalysts (ADMCs) is possible through site-specific electrodeposition on transition metal dichalcogenides (e.g., MoS_2, WS_2, $MoSe_2$, WSe_2) with isolated active sites for UPD [131]. The site-specific UPD enables the energetically favorable deposition of single-atom metal on the chalcogen sites, and then automatically terminates the sequential aggregation of metal atoms. For example, atomically dispersed Pt single-atoms on chemically exfoliated molybdenum disulfide (ce-MoS_2) were synthesized by first exploring the UPD of Cu atoms on (ce-MoS_2), followed by introducing $PtCl_4^{2-}$ ions into the Cu-SAs/MoS_2 system for the galvanic exchange of Cu atoms by Pt(II) [131]. No Pt-containing clusters or nanoparticles were observed, and the Pt atoms are atomically dispersed on ce-MoS_2, as confirmed by aberration-corrected high-angle annular dark-field-scanning TEM (HAADF-STEM) image in Fig. 9f. A magnified HAADF-STEM image (Fig. 9g) and its corresponding density functional theory (DFT)-optimized structural model (Fig. 9h and 9i) provide evidence for Pt attachment on the Mo top site. Moreover, analysis by STEM coupled with energy-dispersive X-ray spectroscopy (STEM-EDS) reveals that atomic Pt is homogeneously dispersed over the whole material (Fig. 9j). The electrocatalytic activity of the fabricated Pt-SAs/MoS_2 was evaluated towards HER. Compared to ce-MoS_2, Pt-SAs/MoS_2 shows exceptional electrocatalytic activity in the HER with low overpotential (Fig. 9k). Furthermore, Pt-SAs/MoS_2 shows higher electrocatalytic HER activity than commercial Pt/C, as normalized to the loading amount of Pt, the mass activity of Pt-SAs/MoS_2 at an overpotential of 0.05 V is 17.14 A mg^{-1}, exceeding that of commercial Pt/C by a factor of 114 (inset of Fig. 9k). Pt-SAs/MoS_2 exhibits a Tafel slope of 31 mV dec^{-1}, whereas ce-MoS_2 exhibits a much larger Tafel slope of 91 mV dec^{-1}, implying faster kinetics owing to single-atom Pt decoration.

Significantly, this approach can be expanded to synthesize a diverse range of ADMCs (Pt, Pd, Rh, Cu, Pb, Bi, and Sn), underscoring its versatility for manufacturing functional ADMCs in the field of electrocatalysis.

Furthermore, the electrodeposition of metal nanoparticles does not experience UPD and initiates the electrocrystallization process

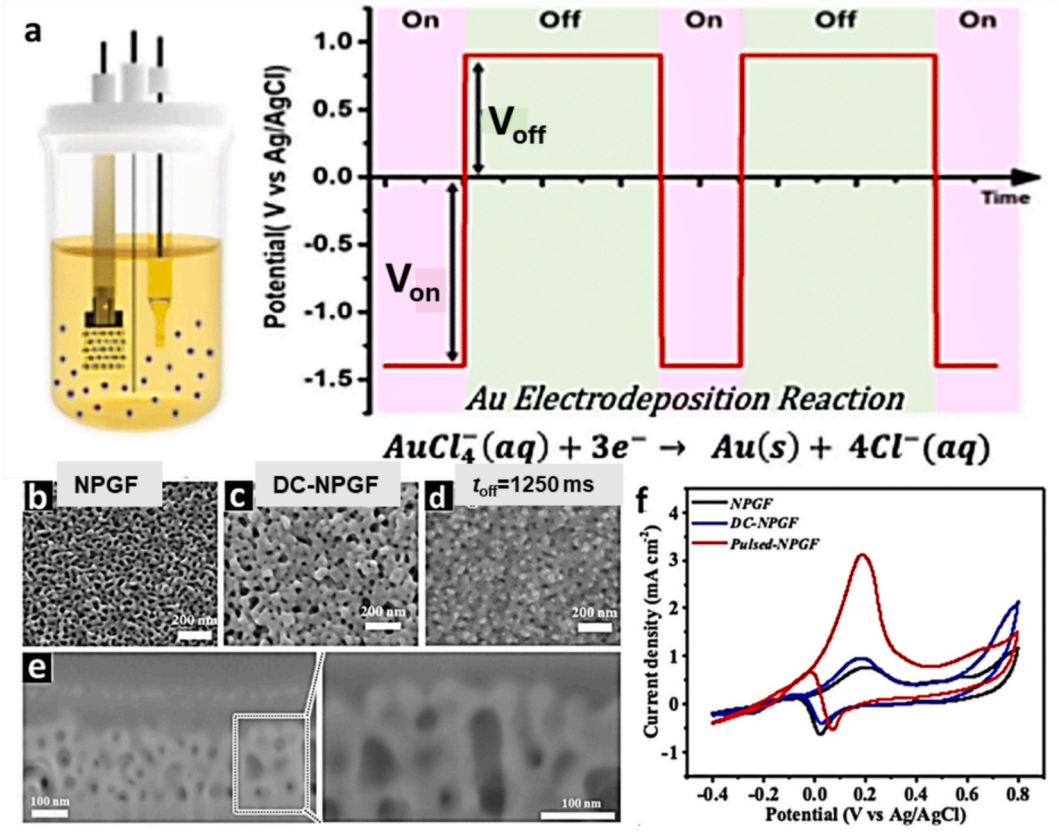

Fig. 11. Secondary pulsed electrodeposition for tailoring surface coordination and crystallographic orientation. (a) Schematic representation of the pulsed electrodeposition protocol, showing the time–potential waveform used to fabricate pulsed nanoporous gold films (pulsed-NPGF). SEM micrographs of (b) NPGF prepared without post-treatment, (c) DC-treated NPGF (DC-NPGF), and (d) pulsed-treated NPGF (pulsed-NPGF; t_{off} = 1250 ms). (e) FIB–SEM cross-section of the pulsed-NPGF, revealing the internal porous architecture. (f) Electrocatalytic performance of the three films, shown as cyclic voltammograms recorded in 0.5 M KOH containing 5 M methanol.
Reproduced with permission from [136].

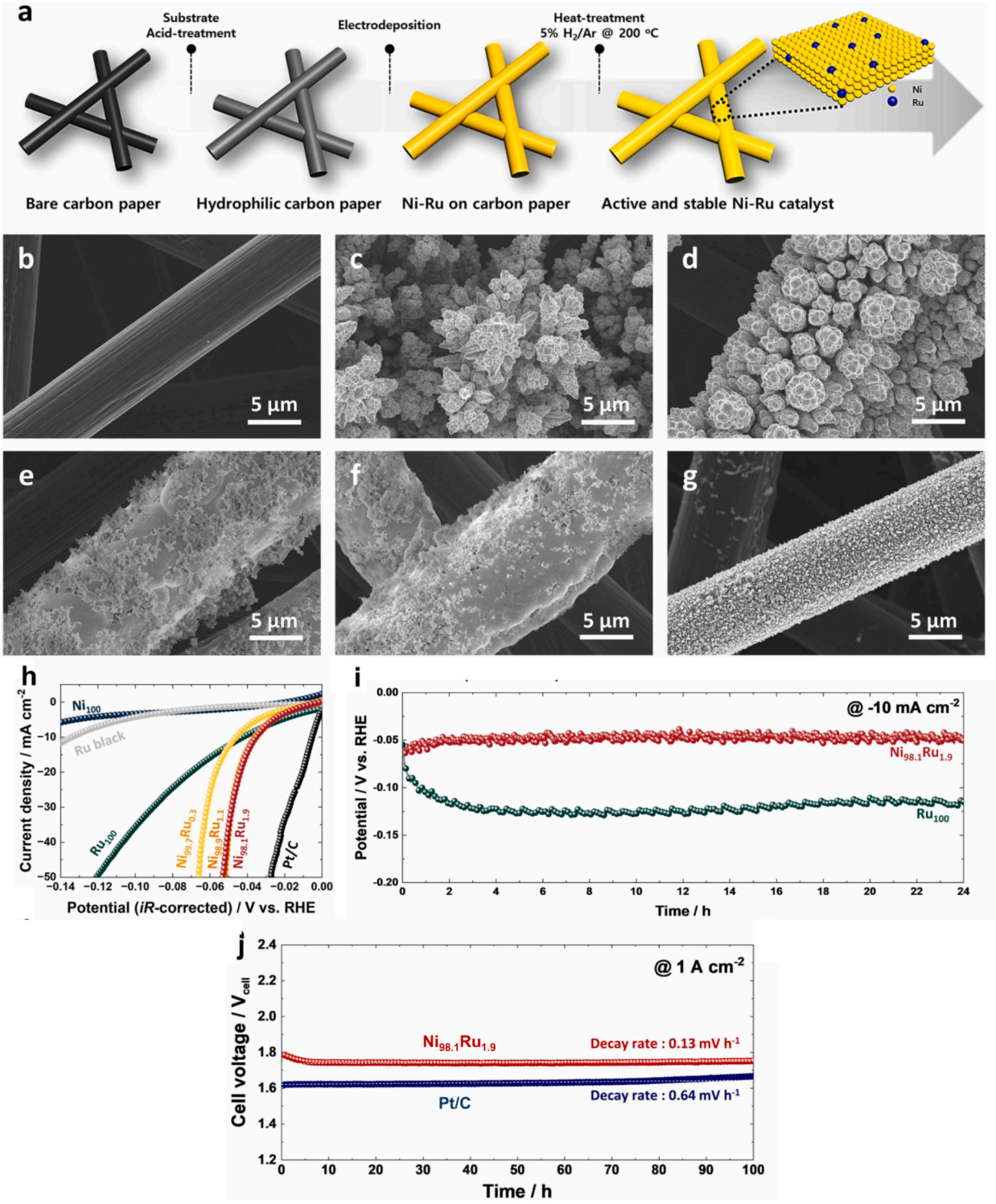

Fig. 12. Electrodeposited Ni–Ru porous transport electrodes for HER and PEMWE operation. (a) Schematic of the electrodeposition-based fabrication of Ni–Ru catalyst-integrated electrodes. FE-SEM images of (b) carbon paper, (c) Ni_{100}, (d) $Ni_{99.7}Ru_{0.3}$, (e) $Ni_{98.9}Ru_{1.1}$, (f) $Ni_{98.1}Ru_{1.9}$, and (g) Ru_{100} samples electrodeposited on carbon paper. (h) HER polarization curves demonstrating the strong activity enhancement upon Ru incorporation, approaching Pt-like performance at low Ru loadings. (i) Chronopotentiometric stability at − 10 mA cm^{-2} showing superior durability of $Ni_{98\cdot1}Ru_{1\cdot9}$ compared to pure Ru. (j) Long-term PEMWE operation at 1 A cm^{-2}, highlighting sustained performance under device-relevant conditions.
Reproduced with permission from [137]

in the overpotential deposition OPD range. This results in the formation and growth of three-dimensional metal nanoparticles, a phenomenon known as the Volmer-Weber growth mechanism [28,30,111,121,122,127,132,133]. The effective electrodeposition of nanoparticles with specific shapes and sizes relies on understanding the kinetics and mechanism of the initial electrocrystallization stages.

For instance, AuNPs were deposited from 0.1 M $NaNO_3$ solution containing 0.25 mM $HAuCl_4$ onto glassy carbon (GC) using various sets of potential and duration from −0.3 to 0.7 V *vs.* SHE and 10 to 1800 s, respectively (Fig. 10a-f) [134]. On the first forward scan in Fig. 10a (solid line), one single reduction peak was noticed at 0.63 V, which was absent for measurements with Au(III) ion-free $NaNO_3$ solution (Fig. 10a, dotted line). This reduction peak is related to the three-electron reduction process of Au(III), resulting in the formation of gold atoms that form metallic AuNPs on the electrode surface.

Fig. 10b presents the last of the 30 consecutive scans recorded for each deposit. It appears that the most efficient deposition is obtained at −0.3 V *vs.* SHE for 1800 s, considering the amount of deposited Au ($Q_{Au(III)} = 9.7$ mC). The electrodeposition at −0.30 V allows the formation of more numerous nuclei than when performed at 0.70 V *vs.* SHE, regardless of the electrolysis duration. As a consequence, the Au active surface area is much larger after depositing at −0.30 V *vs.* SHE, as can be seen by comparing curves in Fig. 10b. The four micrographs show that electrodeposition at −0.30 V affords much denser deposits of smaller AuNPs than those at 0.70 V *vs.* SHE (Fig. 10c-f). At −0.30 V, the AuNPs are relatively small and almost hemispherical-shaped, and homogeneously distributed on the GC surface. Furthermore, increasing the electrodeposition time leads to slightly bigger AuNPs and still homogeneous deposits. In comparison, performing electrodeposition at 0.70 V results in very sparse deposits of big AuNPs, even for low electrolysis time (Fig. 10c). Increasing the electrolysis duration induced a significant increase in the diameter of particles, leading to the formation of very big, raspberry-like AuNPs (Fig. 10d, inset). The smallest AuNPs (25 ± 12 nm) exhibit the highest electrocatalytic performance toward ORR in NaCl–$NaHCO_3$ (0.15 M/0.028 M, pH 7.4).

In a different study, dendrite-like gold nanostructures (DGNs) were directly electrodeposited from a 0.1 M KCl solution containing 10 mM $HAuCl_4$ for 3600 s at different potentials onto the surface of GCE [135]. Fig. 10g shows cyclic voltammograms of the DGNs/GC electrodes (with different electrodeposition potentials) in an aqueous 0.5 M H_2SO_4 solution. The typical anodic oxidation peak starting from 1.1 V and the cathodic reduction peak appearing at 0.90 V *vs.* Ag/AgCl are attributed to the formation of Au oxide and a subsequent reduction reaction, respectively. The enhancement in the peak at around 1.38 V *vs.* Ag/AgCl in the oxidation regime indicates the formation of (111)-facets. The EASA of dendrite structures prepared at −0.30 V is higher than that of the other morphologies, which is consistent with the morphology evolution observed in the SEM images (Fig. 10*h*-k). The DGNs as an electrocatalyst showed a quick response (less than 2 s) and a low detection limit (0.05 mM) for non-enzymatic glucose sensing.

A representative example highlighting the ability of electrodeposition to precisely tailor surface coordination and crystallographic selectivity is provided by the secondary pulsed electrodeposition of nanoporous gold films for methanol electrooxidation [136]. In this study, nanoporous Au electrodes were modified via pulsed cathodic deposition from an $HAuCl_4$-containing electrolyte, where alternating deposition and relaxation periods enabled repeated nucleation while suppressing unrestricted growth (Fig. 11a). Structural characterization reveals that this protocol preserves the bicontinuous nanoporous architecture (Fig. 11b-e) while inducing the formation of nanoscale features on the ligament surfaces, accompanied by a pronounced redistribution of exposed facets. X-ray diffraction analysis shows a significant enhancement of the Au(111) reflection relative to Au(220), evidencing that the pulsed deposition selectively favors low-index, catalytically active facets through kinetic control of electrocrystallization. These structural modifications translate directly into improved electrocatalytic performance toward methanol electrooxidation in alkaline electrolyte, manifested by a lower onset potential and higher peak current density compared to pristine and continuously deposited nanoporous Au electrodes (Fig. 11f). Importantly, the enhanced activity cannot be attributed solely to increased electrochemically active surface area, but reflects intrinsic changes in surface coordination and facet-dependent adsorption energetics. In addition to improved activity, the pulsed-deposited electrodes exhibit superior operational stability, as demonstrated by reduced current decay during prolonged polarization, indicating that electrodeposition-induced restructuring can simultaneously optimize activity and durability. This example underscores electrodeposition as a powerful electrochemical strategy for modulating atomic-scale surface motifs and crystallographic orientation, thereby enabling direct structure–function correlations in electrocatalytic alcohol oxidation.

A compelling demonstration of the potential of electrodeposition for industrially relevant electrocatalysis is provided by the development of atomically dispersed Ru on Ni catalyst-integrated porous transport electrodes (Ni–Ru/PTE) for proton exchange membrane water electrolysis (PEMWE) [137]. As illustrated in Fig. 12**a–g, a** one-step electrodeposition strategy enables the direct fabrication of binder-free and self-supported catalyst layers on carbon paper, yielding uniform and conformal coatings with tunable morphology.

The SEM analysis reveals a clear morphology–composition relationship governed by deposition kinetics. The Ni_{100} catalyst (Fig. 12c) exhibits radially grown dendritic structures, characteristic of mass-transfer-limited electrodeposition at highly negative potentials (−1.7 V *vs.* SCE), where H^+ supplied from NH_4^+ further promotes dendritic growth. With the introduction of small amounts of Ru ($Ni_{99.7}Ru_{0.3}$, Fig. 12d), the deposits become more uniform with smoother edges, indicating a transition toward kinetically controlled growth. This behavior is attributed to the formation of Ru–amine complexes in the presence of NH_4Cl, which retard deposition kinetics and reduce mass-transfer limitations. Increasing the Ru content ($Ni_{98.9}Ru_{1.1}$ in Fig. 12e and $Ni_{98.1}Ru_{1.9}$ in Fig. 12f) leads to a pronounced morphological transition from dendritic clusters to compact, film-like structures. The Ru_{100} sample obtained after 10 min deposition consists of sparsely distributed nanoparticles with very low loading (0.004 mg cm^{-2}). In the absence of complex formation, the deposition kinetics are markedly enhanced, leading to higher growth rates. Accordingly, extending the deposition time to 30 min (Fig. 1g) enables comparable Ru loadings to those in $Ni_{98.1}Ru_{1.9}$, facilitating a meaningful comparison of catalytic performance. This structural evolution is directly linked to catalytic performance, as shown in Fig. 12**h**, where even minimal Ru incorporation (≤1.9 at%) dramatically reduces the HER overpotential from 171 mV for pure Ni to ~ 35 mV at − 10 mA cm^{-2},

approaching Pt-like activity.

Equally important, the catalyst exhibits remarkable durability, as evidenced in Fig. 12**i**, where the $Ni_{98.1}Ru_{1.9}$ electrode maintains stable operation at −10 mA cm^{-2} over 24 h with negligible degradation, in contrast to the pure Ru electrocatalyst that exhibits rapid performance loss. Most significantly, when integrated into a full PEMWE device, the electrodeposited Ni–Ru/PTE achieves industrially relevant performance, delivering current densities up to 6.0 A cm^{-2} at 2.25 V and stable operation at 1 A cm^{-2} with a low degradation rate of 0.13 mV h^{-1} over 100 h (Fig. 12j). These values not only surpass previously reported non-Pt systems but also compete with the commercial Pt/C electrodes at high current densities. This example highlights the strength of electrodeposition as a scalable and versatile fabrication route for advanced electrocatalysts, demonstrating precise compositional tuning, direct integration into device-relevant architectures, and elimination of binders.

Despite its apparent controllability, electrodeposition is often interpreted using simplified nucleation and growth models that may not fully capture the dynamic nature of electrochemical interfaces. In practice, factors such as local pH fluctuations, ion depletion, and electric field gradients can lead to non-uniform growth and metastable structures. Importantly, electrodeposited structures should not be regarded as static entities. Under electrocatalytic operating conditions, deposited overlayers, nanoparticles, and even single-atom sites may undergo dynamic restructuring driven by potential cycling, surface oxidation and reduction, dealloying, or cathodic corrosion. As a result, electrodeposition often defines an initial structural state that subsequently evolves through the electrochemical processes discussed in later sections of this review. Recognizing this dynamic interplay is essential for rational catalyst design, as catalytic performance ultimately reflects not only the as-deposited structure, but also its transformation under realistic operating conditions.

4.2. Repetitive oxidation–reduction cycles

Conducting repetitive oxidation–reduction cycles, involving both anodic and cathodic processes, can trigger the restructuring of metal electrodes. Several physical reasons underlie the transformations observed in the surface structure of metal electrodes. For instance, repetitive cycling results in a flux of adatoms and vacancies; thus, the developing structure changes can, in principle, be

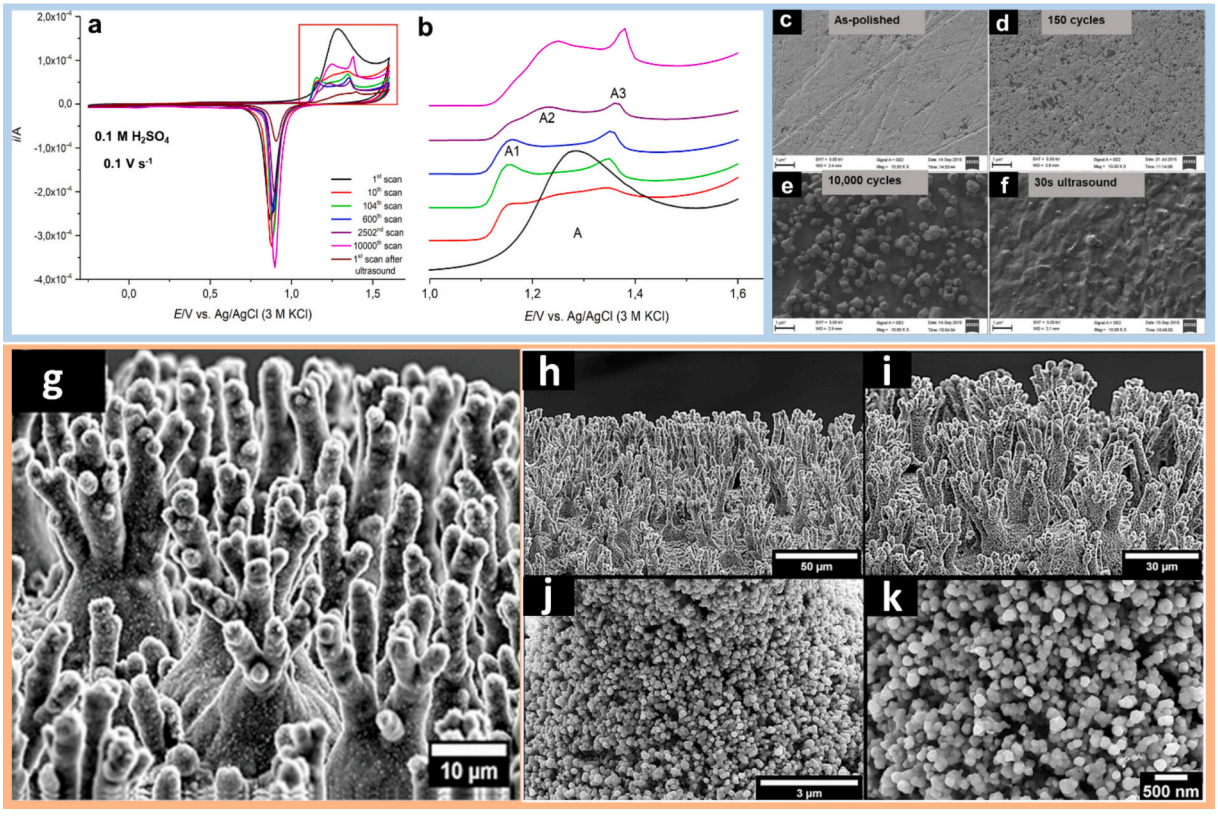

Fig. 13. Surface restructuring induced by repetitive electrochemical cycling. (a) Cyclic voltammograms of polycrystalline Au electrodes in 0.1 M H_2SO_4, as a function of cycling number from −0.25 V to +1.6 V *vs.* Ag/AgCl at 0.1 V s^{-1}. A closer look at the marked potential range is shown in (b). SEM images of the electrodes at various stages: (c) as-polished surface, (d) after 150 cycles, (e) after 10,000 cycles, and (f) after 30 s of ultrasound post 10,000 cycles. Scale bar: 1 µm. (a-f) are reproduced with permission from [89]. (g) SEM images of Cu surface after polarization at 525 V for 60 s in 0.01 M KOH + 0.001 M SiO_2. Subsequent to electrochemical potential cycling, the SEM images (k-h) captured at various magnifications showcase the emergence of nanospheres across the coral-like structure. Reproduced with permission from [34,140].

described by (homoepitaxial) film and crystal growth theories [138,139]. In this respect, the original surface undergoes a surface reaction, where atoms from the original terrace are displaced and pushed to the top of the surface. During the restoration or reduction, the atoms on top of the surface nucleate into islands and vacancies, leading to the formation of vacancy islands on the original surface. Upon repeated cycling, the structural changes are more pronounced [138,139]. Additionally, electrochemical cycling could lead to the dissolution and re-deposition of metal ions, leading to the growth of metal nanoparticles.

The effect of repeated oxidation and reduction cycles on the surface structure of polycrystalline Au electrodes was examined [34]. Repetitive electrochemical potential cycling of a polycrystalline Au electrode in 0.1 M H_2SO_4 from − 0.25 V to + 1.6 V *vs.* Ag/AgCl at 0.1 V s^{-1} results in a distinctly different set of cyclic voltammograms (Fig. 13a,b). The EASA increases with an increasing number of cycles. Additionally, the distribution of facets changes cycling, notably with the development of (111) facets, evident in the oxide regime, as indicated in Fig. 13a and 12b.

The SEM images show the emergence of pits after 150 cycles, as compared to the as-polished Au electrode (Fig. 13c and 13d). Furthermore, the Au surface is covered with distinct nano- and microcrystallites of varying shapes and sizes after 10,000 cycles (Fig. 13e). After the removal of these nanoparticles from the surface through sonication (Fig. 13f), the cyclic voltammograms remain similar to those of the 10,000th cycle (refer to Fig. 13a and 13b). However, the currents observed are notably reduced due to the decreased EASA.

Furthermore, electrochemical cycling can lead to the removal of the oxide layer for the pre-oxidized surface, and thus induce structural changes, as illustrated in Fig. 13g-k [140]. For example, homogeneously distributed 3D coral-like microstructures are formed on Cu surfaces after in-liquid plasma treatment in the presence of SiO_2 nanoparticles at 525 V for 60 s (Fig. 13g). The microstructured copper electrode is composed of CuO as a thin outer layer and a significant amount of inner Cu_2O. Remarkably, the fabricated microstructures are transformed to nanospheres assembled in coral-like microstructures after electrochemical cycling in the potential range between −0.2 and 0.4 V *vs.* RHE (Fig. 13h-k). Such structural transformations lead to a significant increase in the EASA. Furthermore, not only is the surface morphology altered after the electrochemical cycling, but also the chemical composition at the interface, in which the oxygen content is massively decreased due to the reduction of the oxide layer.

A recent study provides a clear and quantitatively compelling demonstration of how electrochemical potential cycling can be used to enhance both the activity and stability of noble-metal catalysts (Pd, Au, and Pt) for the electrochemical oxidation of ethylene glycol (EG) to glycolic acid (GA) [141]. Unlike conventional constant-potential electrolysis, the potential cycling strategy deliberately alternates anodic and cathodic potentials to dynamically regulate the surface oxidation state of the catalyst during operation (Fig. 14). Under anodic polarization, EG oxidation proceeds on metallic noble-metal sites but is progressively hindered by the formation of surface metal oxides, which block active sites and lead to rapid catalyst deactivation. Potential cycling overcomes this limitation by incorporating a cathodic step in each cycle, during which the surface oxide layer is reduced, thereby regenerating a metallic surface that is catalytically active for EG oxidation in the subsequent anodic scan. *In-situ* Raman spectroscopy and X-ray absorption spectroscopy (XAS) directly confirm that the enhanced performance under potential cycling originates from the suppression of persistent

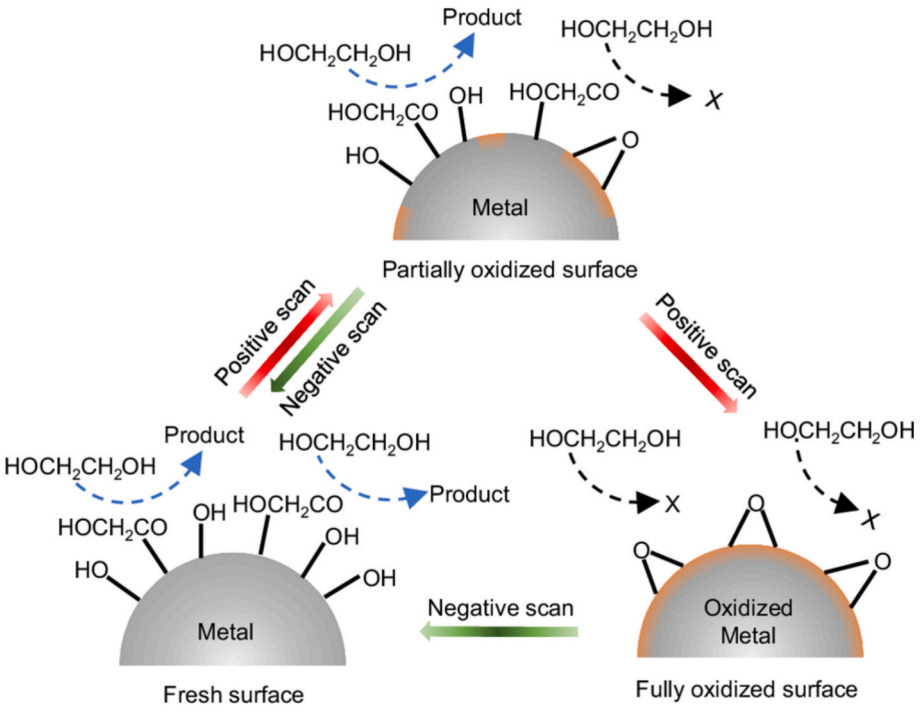

Fig. 14. Schematic illustration of the EGOR deactivation over noble metal (M = Pd, Pt, Au) catalyst during EPC electrolysis. Reproduced with permission from [141]

surface oxides, rather than from changes in catalyst composition or morphology. As a result of this dynamic surface-state control, EPC enables a ~ 20-fold increase in EG conversion rate compared to constant-potential EG oxidation (CP-EGOR), while maintaining exceptionally high GA selectivity exceeding 95%. Remarkably, potential cycling-EGOR achieves the same conversion rate using approximately 90% less noble metal loading than CP-EGOR, underscoring the efficiency gains associated with maintaining the catalyst in its optimal surface state rather than maximizing surface area alone. The stabilizing effect of EPC is particularly striking. Continuous operation under potential cycling conditions sustains high catalytic activity for at least 60 h with no detectable deactivation, whereas the same electrodes operated under constant potential lose activity completely within minutes. This contrast highlights that catalyst degradation during EGOR is not intrinsic to the material, but rather to the electrochemical protocol, emphasizing the importance of dynamic potential control as a stability-preserving strategy. Importantly, the authors further demonstrate the scalability and practical relevance of potential cycling by implementing the approach in a flow-cell configuration, achieving a high EG-to-GA conversion rate of 1.70 mmol h^{-1} mg^{-1}, among the highest reported values in the literature. These results establish potential cycling not merely as a laboratory optimization technique, but as a broadly applicable methodology for the electrochemical upgrading of alcohols and other oxygenated feedstocks.

Of note, the stochastic nature of repeated oxidation–reduction processes can lead to limited reproducibility and poor control over the final surface structure. It remains unclear to what extent these dynamically generated active sites persist under steady-state operation, or whether they represent transient states that continuously evolve. Addressing these questions requires time-resolved and *operando* approaches capable of linking dynamic structural changes to catalytic function.

4.3. Anodic polarization

Anodic polarization represents a powerful electrochemical strategy for restructuring metal electrodes through oxidation-driven surface and near-surface transformations. Depending on the applied potential (or voltage), electrolyte composition, and duration, anodic polarization can induce markedly different restructuring pathways, ranging from subtle surface roughening to the formation of highly porous or composite architectures. Conceptually, anodic polarization regimes can be categorized into three distinct ranges: (i) moderate anodic polarization leading to reversible oxide formation and reduction [142–144], (ii) high-voltage anodization in the presence of fluoride-containing electrolytes [145–150], and (iii) extreme anodic polarization resulting in plasma-assisted electrochemical processes [140,151]. Each regime is governed by different physicochemical mechanisms and produces distinct surface structures.

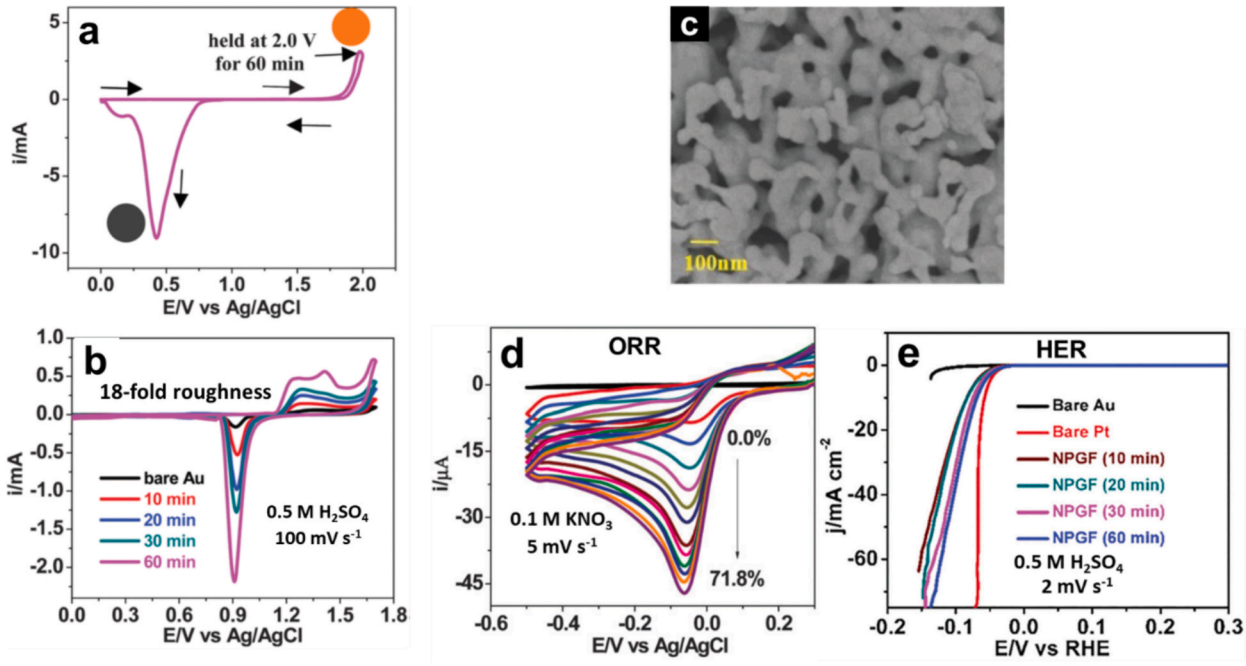

Fig. 15. Formation and electrocatalytic activity of nanoporous gold electrodes. (a) Cyclic voltammetric fabrication of a nanoporous Au film electrode at the scan rate of 20 mV s^{-1}, (b) Electrochemical responses of bare gold and nanoporous gold film electrodes after different polarization times. (c) FE-SEM image of the nanoporous gold film electrode prepared at a polarization time of 60 min. (d) Cyclic voltammograms of nanoporous gold film electrode for dissolved oxygen in 0.1 M KNO_3 solution at several concentrations. (e) HER activity of bare Au, Pt, and nanoporous gold film electrodes in 0.5 M H_2SO_4 solution.
Reproduced with permission from [142,143]

4.3.1. Moderate anodic polarization: Oxide-mediated surface restructuring

At moderate anodic potentials, metals undergo electrochemical surface oxidation without dielectric breakdown of the electrolyte. In this regime, anodic polarization promotes the formation of surface oxide layers, accompanied by metal atom removal, vacancy generation, and stress accumulation within the near-surface region. Subsequent electrochemical reduction of these oxide layers can result in pronounced surface restructuring, including roughening, faceting, and nanopore formation, driven by mass redistribution during oxide growth and collapse [142–144].

For instance, an Au electrode was subjected to polarization from 0.0 to 2.0 V *vs.* Ag/AgCl at a scan rate of 20 mV s^{-1} in a 0.5 M H_2SO_4 solution [142,143]. Following the forward scan, the Au electrode potential was held at 2.0 V *vs.* Ag/AgCl for various durations ranging from 10 to 60 min to form an Au oxide film, characterized by an orange-yellowish colour on the electrode surface. The selection of 2.0 V as the potential was slightly more positive than the threshold for gas evolution to ensure the uniform structure and stability of the nanoporous Au film, since more positive potentials lead to the observation of gas bubble evolution on the electrode surface, potentially affecting the formation and stability of the nanoporous structure. Subsequently, the generated oxide layer was reduced to create a nanoporous Au film, which appears black during the reverse scan, as illustrated in Fig. 15a. Cyclic voltammetric profiles of both bare Au and nanoporous Au electrodes, fabricated with different holding times (10, 20, 30, and 60 min), in a 0.5 M H_2SO_4 solution at a scan rate of 0.1 V s^{-1} are depicted in Fig. 15b. Notably, the EASA of the nanoporous Au electrodes increases as a function of the holding time. The EASA is determined by integrating the charge associated with the reduction of Au oxide. The roughness factor, calculated as the ratio between EASA and the geometrical area (0.07065 cm^2), is determined to be 4.68, 14.5, 21.5, 44, and 86, respectively, for bare gold and nanoporous Au electrodes fabricated with holding times of 10, 20, 30, and 60 min, respectively. Furthermore, the SEM image of the fabricated nanoporous Au electrode (60 min holding time) reveals the formation of nanoporous structures with an average pore size of approximately 32 nm (Fig. 15c).

The response of the fabricated nanoporous Au electrode was evaluated for 0.1 M KNO_3 solutions containing varying concentrations of molecular oxygen (ranging from 0 to 71.8%). Voltammograms in Fig. 15d demonstrate that the current increases linearly with the concentration of dissolved oxygen. This indicates that the nanoporous Au electrode can serve as a probe for continuous monitoring of changes in the concentration of dissolved oxygen, with a limit of detection (LOD) of 35 μM and a correlation coefficient of 0.9983. Moreover, it exhibits high electrocatalytic activity for the reduction of dissolved oxygen at a low overpotential in a neutral 0.1 M KNO_3 solution.

Additionally, the electrocatalytic activity of the fabricated nanoporous Au electrodes with different holding times was assessed for the HER (Fig. 15e). It is observed that with an increase in the holding time from 10 to 60 min, the overpotential for HER shifts towards less negative potentials. In contrast, a bare Au electrode exhibits poor HER activity. Particularly noteworthy are the very low overpotential values of −0.070 V at 10 mA cm^{-2} and −0.083 V at 20 mA cm^{-2} recorded for the nanoporous gold electrode fabricated with 60 min holding time. Beyond these overpotentials, the cathodic current increases significantly at more negative potentials. This high performance closely approaches that of a Pt electrode, attributable to the higher number of active sites in the nanoporous structure, characterized by a high surface area and/or high roughness factor.

4.3.2. High-voltage anodization in fluoride-containing electrolytes

At higher applied voltages, particularly in electrolytes containing fluoride ions, anodic polarization transitions into classical electrochemical anodization [145–150]. In this regime, field-assisted ion migration and localized oxide dissolution dominate, leading to the formation of self-organized oxide architectures such as nanopores, nanotubes, nanowires, and nanoflowers on valve metals and their alloys. The presence of fluoride ions is critical, as they chemically dissolve the growing oxide, enabling a dynamic balance between oxide formation and dissolution that governs morphology and ordering.

While anodization in fluoride-containing electrolytes has enabled the fabrication of highly ordered oxide nanostructures with applications in biomedicine, photoelectrochemical energy conversion, and supercapacitors, this regime primarily yields thick oxide films rather than metallic or metal–oxide hybrid surfaces. As such, fluoride-assisted anodization falls outside the main focus of the present review, which emphasizes electrochemical strategies for restructuring metallic electrodes and metal–metal oxide interfaces relevant to electrocatalysis. Accordingly, this regime is acknowledged here for completeness but is not discussed in detail.

4.3.3. Extreme anodic polarization: Plasma-assisted electrochemical restructuring

At even higher voltages, anodic polarization can exceed the dielectric breakdown threshold of the electrolyte, giving rise to plasma formation at the electrode–electrolyte interface. This regime, commonly referred to as plasma electrolytic oxidation, contact glow discharge electrolysis, or in-liquid plasma, enables restructuring pathways that are inaccessible under conventional electrochemical conditions [151–157]. The localized plasma generates highly reactive species, extreme electric fields, and transient high temperatures, driving rapid oxidation, melting, and resolidification processes at the electrode surface.

Plasma-assisted anodic polarization enables the formation of metal surfaces with a high degree of porosity and tunable morphology and chemical state, as well as a controllable oxide film, depending on the experimental conditions, such as the electrolyte composition, electrode material, and applied voltage [151–157]. For example, plasma electrolysis has been used to fabricate carbon-coated Janus metal/oxide hybrids, such as CoMo/CoMoOx@C, in which metallic and oxide domains coexist within a single particle separated by an exposed metal–oxide interface [158]. The electrolyte was prepared by mixing 125 ml of deionized water and 125 ml of ethylene glycol, with the addition of 25 mmol of $Co(NO_3)_2$, 25 mmol of Na_2MoO_4, and 12.5 mmol of trisodium citrate. During cathodic polarization, metal ions were reduced to metallic particles. Simultaneously, a significant amount of active oxygen and carbon atoms were generated through the plasma-induced dissociation of water and organic solvents. These active species rapidly reacted with the just-reduced metal, resulting in the formation of M/MO@C. In this structure, a thin carbon layer served as the shell, encapsulating a Janus

metal/oxide hybrid core. The Janus metal/oxide structure comprises metal on one side and oxide on the other, with the metal/oxide interface left exposed, a crucial factor for maximizing the synergistic effects. Fig. 16a illustrates a schematic representation of the fabrication process of CoMo/CoMoOx@C. After plasma electrolysis, aggregates of clump-like microparticles were uniformly deposited on a Cu foil with a film thickness of 4.7 μm (Fig. 16b). Some pores are observed within the film, attributed to the release of gas bubbles during deposition. These clumps consist of numerous small nanoparticles (Fig. 16c and 16d). Furthermore, the inset of Fig. 16d shows a

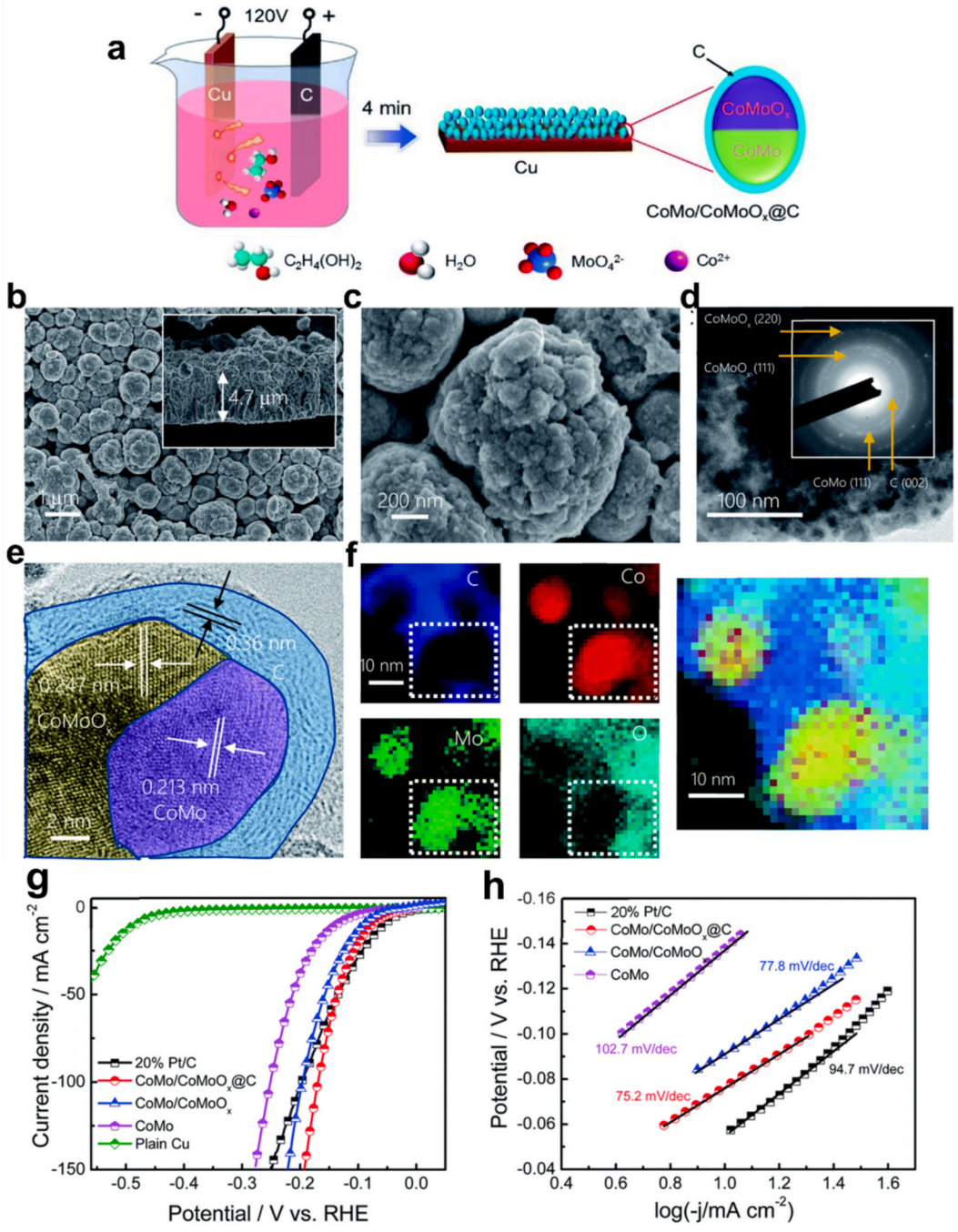

Fig. 16. Plasma-assisted synthesis of hierarchical CoMo/CoMoOx@C structures. (a) Schematic illustration of the fabrication of CoMo/CoMoO$_x$@C by plasma electrolysis process. (b) Low and (c) high magnification SEM images of CoMo/CoMoO$_x$@C. (d) Low magnification TEM image with the corresponding electron diffraction pattern. (e) HRTEM image displaying the carbon-coated Janus structure. (f) Elemental mapping images of C, Co, Mo, and O. Inset of (b) shows the cross-sectional image of CoMo/CoMoO$_x$@C. (g) The iR-corrected linear sweep voltammetry curves measured at a scan rate of 5 mV s^{-1} and (h) the corresponding Tafel plots.
Reproduced with permission from [158]

designated area electron diffraction pattern, which revealed diffraction rings corresponding to the (002) plane of graphite, the (111) and (220) planes of CoMoOx, and the (111) plane of CoMo. This pattern confirmed the composite formation of carbon, metal (CoMo), and oxide (CoMoOx). A thin carbon layer, approximately 3 nm in thickness, covered the surface of these nanoparticles (Fig. 16e). Elemental mapping with electron energy loss spectroscopy (EELS) further elucidates the spatial distribution of C, Co, Mo, and O (Fig. 16f). This analysis identifies a core@shell structure, with Co, Mo, and O comprising the core and only C forming the shell. The distribution of O was non-uniform across the core particle, being rich on one side and less abundant on the other side. In contrast, both Co and Mo were more evenly distributed throughout the core. Based on these characterizations, it was confirmed that a core@shell structured CoMo/CoMoOx@C, with a carbon shell and a Janus particle CoMo/CoMoOx core, was successfully synthesized. The synthesized CoMo/CoMoO$_x$@C hybrid was compared with the control samples as an alkaline HER electrocatalyst (Fig. 16g and 16 h). The plain Cu foil demonstrated negligible HER activity, while electrodeposited CoMo showed an enhanced performance (138 mV @ 10 mA cm^{-2}). As for CoMo/CoMoO$_x$, the overpotential was further reduced to 90 mV by the synergistic effect between the metal and oxide (Fig. 16g). CoMo/CoMoO$_x$@C showed an even better performance of 76 mV at 10 mA cm^{-2}. The Tafel slope decreased from 102.7 to 75.2 mV dec^{-1} for CoMo/CoMoOx@C compared to for CoMo, indicating faster HER kinetics (Fig. 16h). This makes CoMo/CoMoOx@C a promising electrocatalyst for alkaline HER applications.

Although plasma-assisted anodic polarization offers exceptional flexibility in tuning surface morphology and chemical state, it

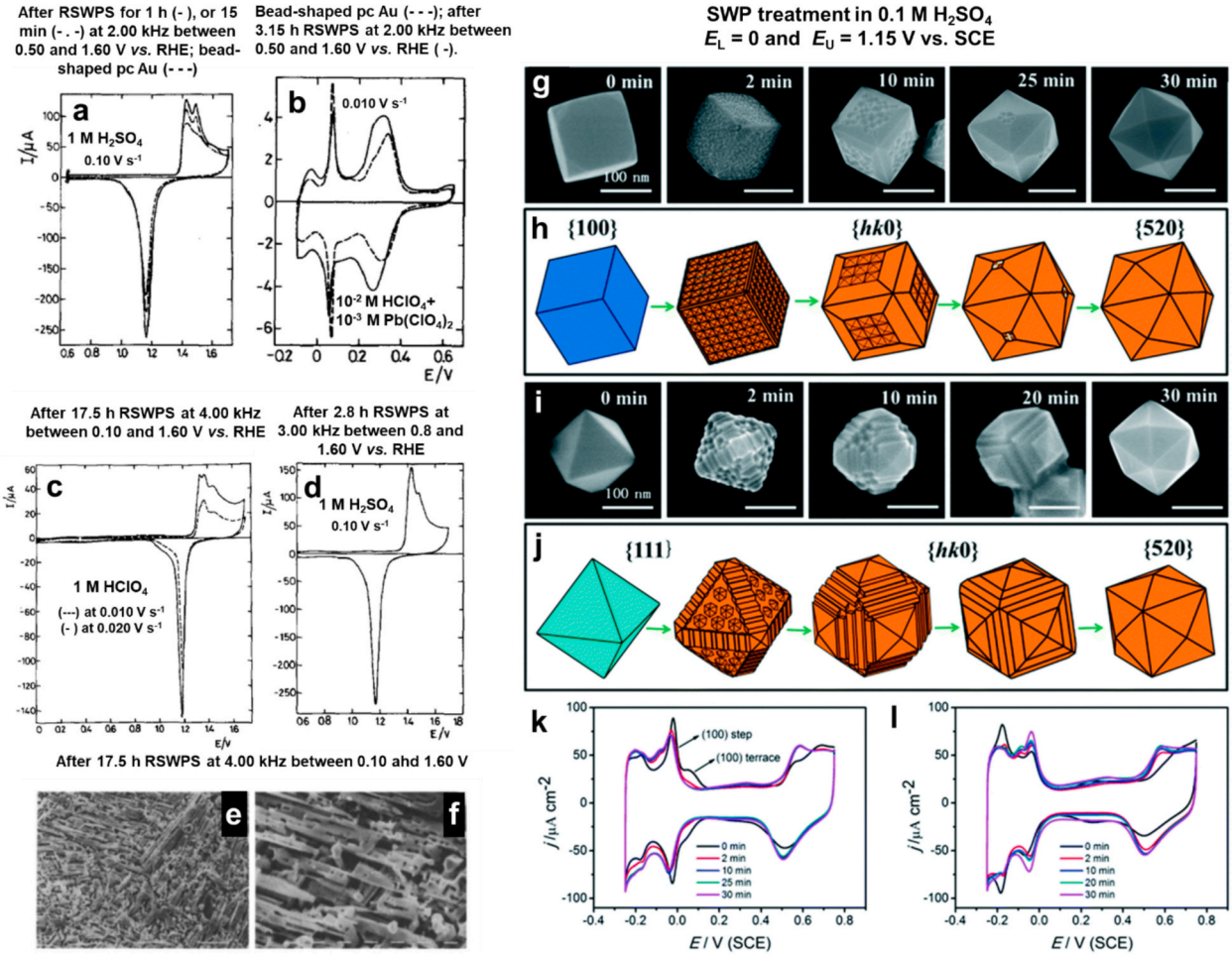

Fig. 17. Surface restructuring under square-wave potential perturbations. Cyclic voltammograms of polycrystalline Au electrodes (a) in 1 M H_2SO_4 at 0.1 V s^{-1} after 1 h repetitive square wave potential signal (RSWPS) at 2.00 kHz between 0.50 and 1.60 V *vs.* RHE and after 15 min RSWPS at 2.00 kHz between 0.50 and 1.60 V *vs.* RHE; (– – –) bead-shaped polycrystalline Au electrode as well as (b) in 10^{-2} M $HClO_4$ + 10^{-3} M $Pb(ClO_4)_2$ at 0.010 V s^{-1}, (– – –) Bead-shaped polycrystalline Au electrode; (–) after 3.15 h RSWPS at 2.00 kHz between 0.50 and 1.60 V *vs.* RHE. Cyclic voltammograms of Au electrodes (c) after 17.5 h RSWPS at 4.00 kHz between 0.10 and 1.60 V *vs.* RHE and (d) after 2.8 h RSWPS at 3.00 kHz between 0.8 and 1.60 V *vs.* RHE. SEM images of Au electrodes after (e and f) 17.5 h RSWPS at 4.00 kHz between 0.10 and 1.60 V *vs.* RHE. (a-f) are reproduced with permission from [88,110]. Structural evolution of Pt nanocrystals, transitioning from (g) cube and (i) octahedron to tetrahexahedron at various periods of square wave potential treatment. Illustration of the shape transformation process from (h) cube and (j) octahedron to tetrahexahedron. Cyclic voltammograms of Pt nanocrystals from (k) cube and (l) octahedron to tetrahexahedron in 0.1 M H_2SO_4 at 50 mV s^{-1}. Reproduced with permission from [114,162].

operates under extreme conditions that differ fundamentally from conventional electrochemical environments. Consequently, this regime is best viewed as the upper boundary of anodic polarization strategies rather than a direct extension of standard electrochemical surface restructuring. Nonetheless, it illustrates the broad continuum of anodic polarization processes and underscores how increasing applied voltage progressively unlocks new restructuring mechanisms.

4.4. Square-wave potential programming

Square-wave potential (SWP) programs represent a distinct and highly dynamic electrochemical regime in which the working electrode is subjected to periodic potential pulses between two defined limits (E_L and E_U) at controlled frequencies. In contrast to slow cyclic voltammetry or static polarization, SWP imposes abrupt transitions between oxidizing and reducing conditions. These rapid potential switches generate complex, non-equilibrium perturbations at the electrode/electrolyte interface, strongly influencing interfacial electric fields, surface oxidation states, double-layer structure, and adsorption–desorption equilibria. Importantly, the potential pulses modulate the coverage and binding strength of adsorbates (e.g., H*, OH*, anions, or metal precursors), periodically forcing their adsorption, reorganization, or removal. During the anodic half-cycle, surface atoms may partially oxidize or interact strongly with specifically adsorbing anions, whereas the cathodic half-cycle can induce reduction, desorption, or re-nucleation processes. Because these perturbations occur on short time scales, often in the kHz regime, the system does not fully relax to thermodynamic equilibrium. Instead, kinetically accessible surface configurations become stabilized. As a result, SWP enables precise control over the surface structure and properties of grown particles, particularly during electrodeposition, where nucleation density, growth direction, and facet stabilization are highly sensitive to instantaneous potential. The amplitude (E_U–E_L), frequency, duty cycle, and total treatment time collectively determine whether atom migration, facet redistribution, or particle reshaping dominates [29,81,114,115,159–163].

In an earlier study, the electrochemical faceting of polycrystalline Au wires and bead-shaped electrodes in 1 M H_2SO_4 was explored using a repetitive symmetrical square wave potential signal (RSWPS) in the 2–4 kHz range, with upper and lower potential limits ranging between 1.44 and 1.60 V and 0.10 and 1.10 V *vs.* RHE, respectively (Fig. 17a-f) [114]. The resulting voltammogram after the electrochemical faceting, produced by RSWPS between $E_L = 0.50$ V and $E_U = 1.60$ V *vs.* RHE at $f = 2.0$ kHz in 1 M H_2SO_4 (Fig. 17a), exhibits a substantial change in the shape of the anodic peak compared to pristine Au electrodes. The new voltammogram possesses two distinct peaks, one at 1.43 V and the other at 1.49 V *vs.* RHE, and there is a considerable increase in both the anodic and cathodic voltammetric charge (by a factor of about 1.5) after 3 h of RSWPS, while the anodic to cathodic charge ratio remains equal to one. These voltammetric changes became more pronounced with longer RSWPS treatment. Similar changes in voltammetry are observed for the UPD of lead (Pb) (Fig. 17b). In this case, the blank exhibits a pair of conjugated sharp peaks at 0.065 V and a second pair of broad peaks at 0.34 V *vs.* RHE. After RSWPS treatment, the height of the former peak decreases, while that of the latter peak substantially increases, indicating the formation of (110)-facets under these conditions. Furthermore, the entire voltammetric charge enhances with the duration of RSWPS treatment, revealing the increase of the EASA. Similar voltammetric responses were observed for $f = 3$ and 4 kHz. The voltammetric profile of RSWPS-treated Au electrodes was also examined in 1 M $HClO_4$, at 10 and 20 mV s^{-1} (Fig. 17c). The RSWPS-treated Au electrodes display three anodic peaks at 1.44, 1.48, and 1.55 V *vs.* RHE, respectively, demonstrating the development of a stable (100)-site preferred orientation. The relative heights of these peaks are very sensitive to the voltammetric sweep rate. Lastly, for $E_L = 0.80$ V, $E_U = 1.60$ V *vs.* RHE, and f between 3 and 4 kHz, a different distribution of the anodic voltammetric peaks is observed (Fig. 17d), with a prevalence of peaks at 1.43 V *vs.* RHE, a shoulder at the upper potential side, and a relatively large increase in the voltammetric charge. These results indicate that the RSWPS treatment could significantly alter the facet distribution, resulting in the formation of either (110)- or (100)-facets, depending on the applied parameters. However, the formation of (111)-facets has not been reported following this treatment. SEM images in Fig. 17e and 17f demonstrate substantial changes in the surface morphology of Au electrodes after 17.5 h of RSWPS at 4.00 kHz between 0.10 and 1.60 V *vs.* RHE.

Even more striking effects of SWP are observed for shape-controlled Pt nanocrystals. Recently, the shape transformation of Pt nanocrystals between high- and low-index facets under the SWP treatment has been investigated [162]. The starting Pt nanocrystals were electrodeposited on a glassy carbon electrode through the SWP technique in a Pt plating solution. Fig. 17g demonstrates the shape transformation from Pt cube to faceted tetrahexahedron (THH) by the SWP treatment ($E_L = 0$ V and $E_U = 1.15$ V *vs.* SCE) in 2 mM H_2PtCl_6 + 0.1 M H_2SO_4 solution. After 2 min of SWP treatment, the flat {100} facets turn rough, characterized by the presence of abundant small pyramids. After 10 min of SWP treatment, new facets emerge near the cubic edges, while small pyramids remain around the center of {100} facets. Following 25 min of SWP treatment, the cubic Pt nanocrystals nearly transform into {*hk*0}-faceted THH nanocrystals, only with their pyramidal vertices being concaved. After 30 min of SWP treatment, well-defined THH nanocrystals with {520} facets are formed. The shape transformation process from cube to THH is shown in Fig. 17h. This surface predominantly consists of (100) terraces and (110) steps. On the {520} facets, the outermost atoms are all kink atoms with a coordination number (CN) of 6, while the CN of {100} facets is 8. The surface structure was characterized by cyclic voltammetry (Fig. 17k). Cubic Pt nanocrystals display a sharp peak at about −0.02 V, and a broad peak between 0.01 V and 0.14 V *vs.* SCE, attributed to hydrogen adsorption on short-range ordered (100) domains ((100) steps) and long-range ordered (100) domains ((100) terraces), respectively, specifying that the cubic Pt nanocrystals have ordered (100) facets. After 2 min of SWP treatment, the peak of the (100) terrace nearly disappeared, revealing the disruption of the long-range ordered surface structure. Furthermore, the peak corresponding to (100) steps at around −0.02 V slightly decreases, while the peak corresponding to (110) at −0.20 V is enhanced. The current of oxygen adsorption at Pt step sites at around 0.55 V rises, similar to that of THH (30 min). These results reveal that the {100} facets transform into high-index facets rapidly (about 2 min), although the surface morphology changes slowly.

The shape transformation from octahedron to THH is also achieved using SWP with E_L and E_U of 0 V and 1.15 V *vs.* SCE,

respectively (Fig. 17i). After 2 min of SWP treatment, the surface of the Pt octahedron becomes considerably rough. A new small pyramid appears at each vertex, and the octahedral edges are substituted by a staircase structure, so-called crystal macro-steps. The attained THH Pt nanocrystals are bound by {520} facets. The cyclic voltammetry profile of the rough Pt nanocrystals obtained after 2 min of SWP treatment resembles that of the final perfect THH Pt nanocrystals and is significantly different from that of the initial Pt octahedron (Fig. 17l). This result shows that the change in the surface structure from {111} to {*hk*0} high-index facets is much faster than the shape change from octahedron to THH. As shown in Fig. 17j, this transformation involves the formation of small pyramids and narrow staircases of {hk0} facets. Such a change from {111} to {hk0} facets requires the migration of only a small number of Pt atoms, making it a rapid process.

From a catalytic perspective, high-index surfaces generated under SWP are particularly relevant for structure-sensitive reactions such as alcohol oxidation, formic acid oxidation, and certain oxygenated intermediate transformations. The increased density of step and kink atoms modifies adsorption energetics and often lowers activation barriers. Therefore, SWP provides not only morphological control but also deterministic tuning of catalytic functionality through dynamic surface engineering.

Overall, square-wave potential programs highlight how dynamic potential control can access surface configurations that are not attainable under steady-state conditions. Rather than merely reshaping electrodes, SWP enables kinetic stabilization of specific crystallographic orientations and defect motifs, providing a direct link between electrochemical perturbation parameters and atomic-scale structure. This establishes dynamic potential engineering as a deliberate strategy for tailoring catalytic surfaces beyond equilibrium limitations.

4.5. Dealloying

Although electrochemical dealloying is frequently implemented using potential cycling protocols, it is mechanistically distinct from repetitive oxidation–reduction cycling of monometallic electrodes. While cycling of pure metals primarily induces restructuring through oxide formation, dissolution–redeposition, and vacancy condensation, dealloying is driven by compositional heterogeneity and the selective dissolution of the less noble component. The resulting structural evolution emerges from the coupled interplay of dissolution kinetics, surface diffusion of the more noble element, and vacancy condensation processes.

Electrochemical dealloying proceeds when the applied potential exceeds the dissolution potential of the less noble component but remains below that of the noble element. Selective dissolution generates a supersaturation of surface vacancies. Rather than collapsing the structure, these vacancies condense into nanoscale voids, while the more noble atoms undergo rapid surface diffusion to minimize surface energy. This self-organized reconfiguration leads to the formation of a bicontinuous ligament–pore network, characteristic of nanoporous metals [164,165].

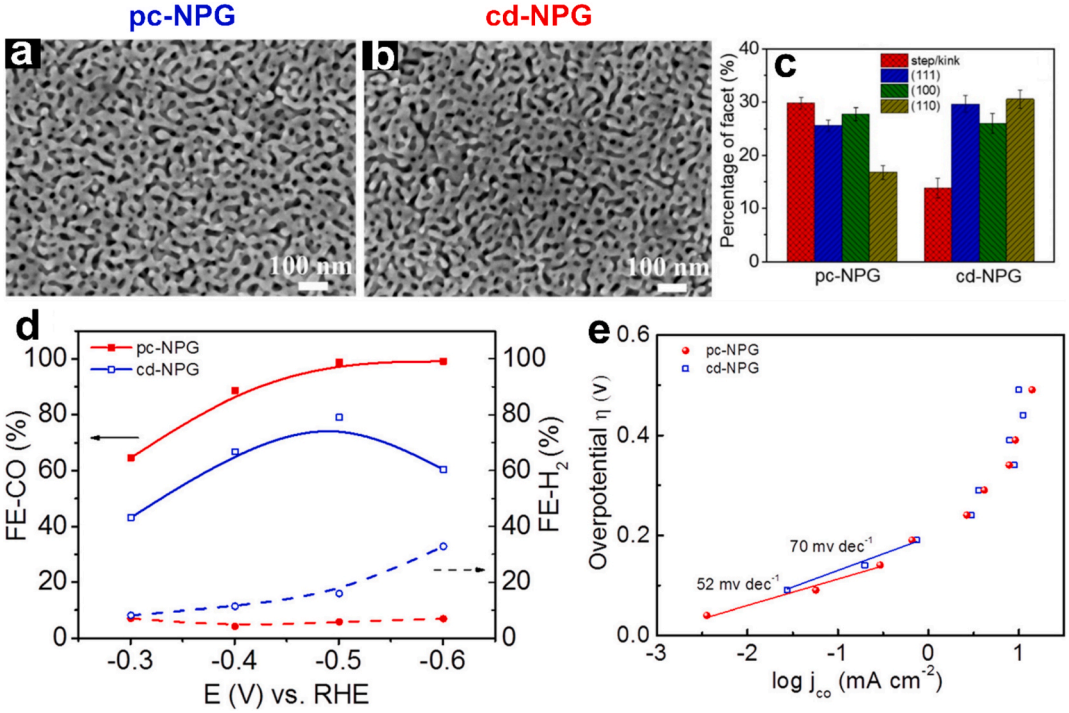

Fig. 18. SEM images of (a) pc-NPG and (b) cd-NPG, respectively. (c) Percentages of different facets in pc-NPG and cd-NPG. (d) Faradaic efficiencies for CO and H_2 at several potentials for pc-NPG and cd-NPG. (e) Tafel plots of CO product on pc-NPG and cd-NPG.
Reproduced with permission from [118]

The evolution of porosity is governed by several key parameters:

- The parting limit, *i.e.*, the minimum concentration of the less noble component required for continuous dissolution pathways.
- The applied potential, which determines dissolution rate and penetration depth.
- Surface diffusion rates of the noble element, which stabilize the evolving ligament structure.
- Scan rate or polarization protocol (potentiostatic *vs.* cyclic), which controls whether the system forms porous networks, hollow core–shell structures, or partially dealloyed surfaces.

Unlike simple surface roughening, dealloying intrinsically couples chemical selectivity and morphological instability, producing structures with high densities of low-coordination sites, residual strain, and altered electronic properties.

Although electrochemical dealloying is frequently implemented using potential cycling protocols, it is conceptually distinct from repetitive oxidation–reduction cycling of monometallic electrodes, as it relies on selective dissolution driven by compositional

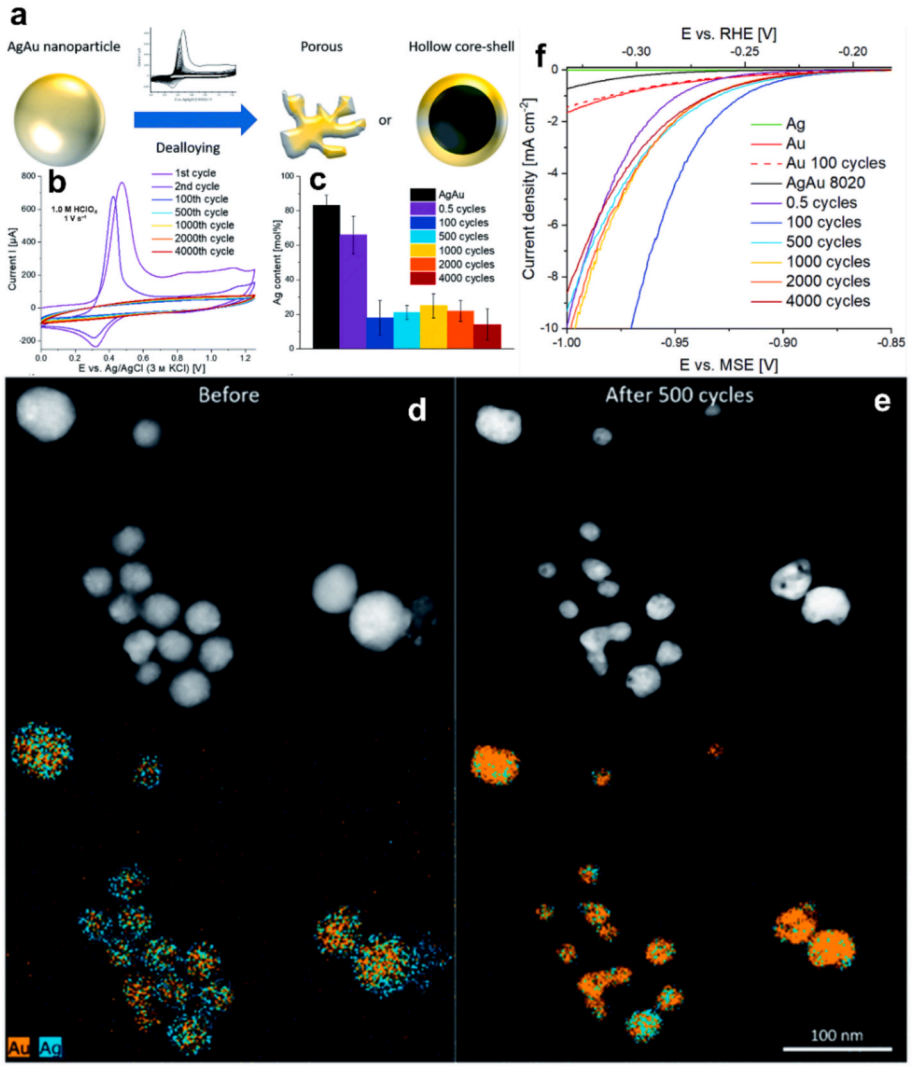

Fig. 19. Electrochemical dealloying as a route to nanoporous or hollow core–shell electrocatalysts. (a) Schematic depiction of an Ag–Au nanoparticle with a core rich in Au, enveloped by an Ag-rich shell before dealloying (left), and the potential formation of a porous or hollow structure following the dealloying process (right). (b) Cyclic voltammetric dealloying of AgAu alloy nanoparticles in 1.0 M $HClO_4$ at 1 V s^{-1} at different cycle numbers, and (c) relative molar amount of Ag retained in the nanoparticles after dealloying, detected by electrochemical dissolution (coulometry) in HCl. TEM and STEM images with EDS mapping at the same position, captured (d) before and (e) after 500 cycles of dealloying in 1 M $HClO_4$. (f) Averaged electrocatalytic linear sweep voltammetry curves from multiple independent experiments at 2 mV s^{-1} in 0.5 M H_2SO_4 using pure Ag and pure Au; 100 cycles "dealloyed" Au, non-dealloyed AgAu 80: 20 and dealloyed AgAu nanoparticles after different numbers of dealloying cycles. The plotted currents are normalized to the EASA of the nanoparticles.
Reproduced with permission from [113].

heterogeneity rather than surface oxide dynamics alone. Dealloying refers to the deliberate dissolution of specific components from an alloy, and it has been applied to various alloy systems. The mechanisms behind the development of porosity and changes in the surface morphology during dealloying are well-understood, particularly for bulk materials and thin films on a microscale. In this context, models to describe how pores evolve have been established [166,167].

In recent years, there has been growing interest in dealloying at the nanoscale, particularly after the discovery that CuPt nanoparticles created through dealloying demonstrated exceptional catalytic properties for the ORR [168]. This has prompted investigations into both chemical and electrochemical dealloying processes for a wide range of alloy compositions and catalytic applications. Electrochemical dealloying offers distinct advantages over chemical methods because it allows for precise control over key factors such as the electrolyte composition, duration, and the potential applied during the process [113,167–170]. This enhanced level of control facilitates the selective dissolution of alloy components and the subsequent restructuring of the nanoparticle surface with high accuracy.

For example, a self-supported 3D nanoporous gold was fabricated by electrochemical dealloying Ag-Au alloy in 0.1 M H_2SO_4 solution with potential cycling (50 cycles) [118]. The chosen cycling potential window of 0.74–1.74 V *vs.* RHE covers the entire redox peaks of Ag and Au elements. The resulting nanoporous gold, termed pc-NPG (potential cycling-NPG), displayed abundant step/kink sites, leading to a significant enhancement in catalytic activity toward CO_2RR when compared to conventional NPG obtained through chemical dealloying (cd-PNG). Both samples exhibit bicontinuous skeletons and interconnected channels, as revealed by the SEM images in Fig. 18a and 18b.

Furthermore, as displayed in Fig. 18c, the fractions of step/kink sites and {111}, {100}, and {110} facets in the pc-NPG electrode are estimated as 29.8%, 25.6%, 27.8%, and 16.8%, respectively. In comparison, for the cd-NPG electrode, the fractions of step/kink sites and {100} facets are lower, whereas the fractions of {111} and {110} facets are higher.

The CO_2RR performance of the NPG electrodes was evaluated in CO_2-saturated 0.5 M $KHCO_3$ (pH ~7.2). The pc-NPG electrode exhibits an ~20% enhancement in Faradaic efficiency (FE_{CO}) at a potential range of −0.3 to −0.6 V *vs.* RHE in comparison with the chemically fabricated one (Fig. 18d). Notably, the FE_{CO} value for the pc-NPG electrode can reach up to 98% at −0.5 V *vs.* RHE. Besides, Tafel analysis revealed that electrochemically fabricated NPG had a Tafel slope of 52 mV dec^{-1}, which was lower compared to the 70 mV dec^{-1} for the chemically fabricated one, indicating the intrinsically higher activity of the pc-NPG electrode (Fig. 18e).

Remarkably, electrochemically dealloying can also be applied to alloy nanoparticles to enhance their electrocatalytic activity. For instance, using AgAu alloy nanoparticles and the HER as a model system, the impact of cyclic voltammetry parameters on the electrocatalytic activity upon electrochemical dealloying was explored [113]. The process of electrochemical dealloying of the AgAu nanoparticles is schematically illustrated in Fig. 19a. Typically, Ag is selectively leached out of the alloy, and a porous or hollow Au-rich structure is formed. This dealloying process is performed with 1.0 M $HClO_4$ at 1 V s^{-1} using various numbers of cycles between E_L = 0 V and E_U = 1.3 V *vs.* Ag/AgCl. In the first cycle, the cyclic voltammogram of AgAu nanoparticles shows a distinct Ag oxidation peak, starting at around 0.3 V *vs.* Ag/AgCl (Fig. 19b). Another peak, associated with the surface oxidation of Au, is observed at around 1.1 V *vs.* Ag/AgCl. Notably, no dissolution of Au was observed in $HClO_4$, consistent with prior studies [171,172]. A cathodic peak detected around 0.3 V *vs.* Ag/AgCl during the reverse scan is attributed to the partial reduction of Ag^+ ions back to $Ag_{(s)}$ at the electrode. In the second cycle, a slightly shifted Ag oxidation peak is observed between 0.3 V and 0.4 V *vs.* Ag/AgCl but no dealloying region is visible in the cyclic voltammogram. Starting from the 70th to the 100th cycle, peaks are no longer discernible in the cyclic voltammogram, and subsequent cycles closely resemble one another. This suggests that further dealloying does not occur. Moreover, the overall Ag content in the nanoparticles, measured using electrochemical methods, remains relatively unchanged after 100 cycles, demonstrating that the nanoparticle composition remains stable during further cycling (Fig. 19c). STEM images and EDS mapping of AgAu nanoparticles before and after 500 cycles of dealloying are presented in Fig. 19d and 19e. These nanoparticles exhibit visible porosity and do not appear to be hollow core–shell structures. Additionally, some nanoparticles undergo significant size reduction (shrinking to about half their original size), while others remain almost unchanged. The EDS mappings reveal a substantial reduction in the Ag content of the nanoparticles.

The electrocatalytic activity of these nanoparticles is assessed for the HER in 0.5 M H_2SO_4 at a scan rate of 2 mV s^{-1} (Fig. 19f). Notably, the same electrochemical cycling treatment used for dealloying does not enhance the activity of pure Au nanoparticles, regardless of the number of cycles. This confirms that the increased electrocatalytic activity of Ag-Au nanoparticles is attributed to the leaching of Ag during dealloying. Interestingly, even a short dealloying treatment of 0.5 cycles resulted in a ten-fold increase in current at −1.0 V *vs.* MSE. However, further dealloying beyond a certain point did not increase catalytic activity, indicating that there is an optimal number of cycles for dealloying. The highest electrocatalytic activity was achieved after 100 cycles (Fig. 19f).

It is worth noting that a study of the dealloying behavior of Ag-Au nanoparticles during potentiostatic dealloying has also been reported [167]. Under constant potential conditions, pore formation was observed, and a similar dealloying behavior as that achieved through cyclic voltammetry at scan rates below 0.1 V s^{-1} was observed. Conversely, for higher scan rates, the authors predicted the formation of hollow core–shell nanoparticles with an Au-enriched outer shell.

Beyond Au-based systems, electrochemical dealloying plays a central role in the design of high-performance fuel cell catalysts. In Pt–Ni, Pt–Co, and Pt–Cu alloys, selective removal of the less noble component generates a Pt-enriched surface layer (often termed a "Pt-skin") atop a subsurface alloy core. This architecture introduces two critical effects [173–175]:

Compressive/expansive lateral lattice strain, modifying the d-band center of Pt and weakening/strengthening oxygen binding, respectively.
Ligand effects, arising from subsurface alloy atoms, alter the Pt electronic structure.

Together, these effects optimize adsorption energetics for the oxygen reduction reaction (ORR), leading to dramatic activity enhancements compared to pure Pt. Importantly, dealloying does not merely roughen the surface; it induces strain-engineered electronic restructuring, demonstrating that electrochemical dealloying is both a morphological and electronic tuning strategy.

The structural outcome of electrochemical dealloying is strongly dependent on the polarization protocol:

- Potentiostatic dealloying at constant potential favors steady dissolution and diffusion-controlled ligament formation.
- Cyclic voltammetry at low scan rates yields similar porous structures.
- High scan rates or pulsed protocols may limit diffusion, promoting hollow or core–shell morphologies.
- Narrow potential windows may induce only partial surface dealloying, producing strained surface layers without bulk porosity.

Therefore, electrochemical dealloying should be viewed not as a single method, but as a family of dynamic restructuring pathways

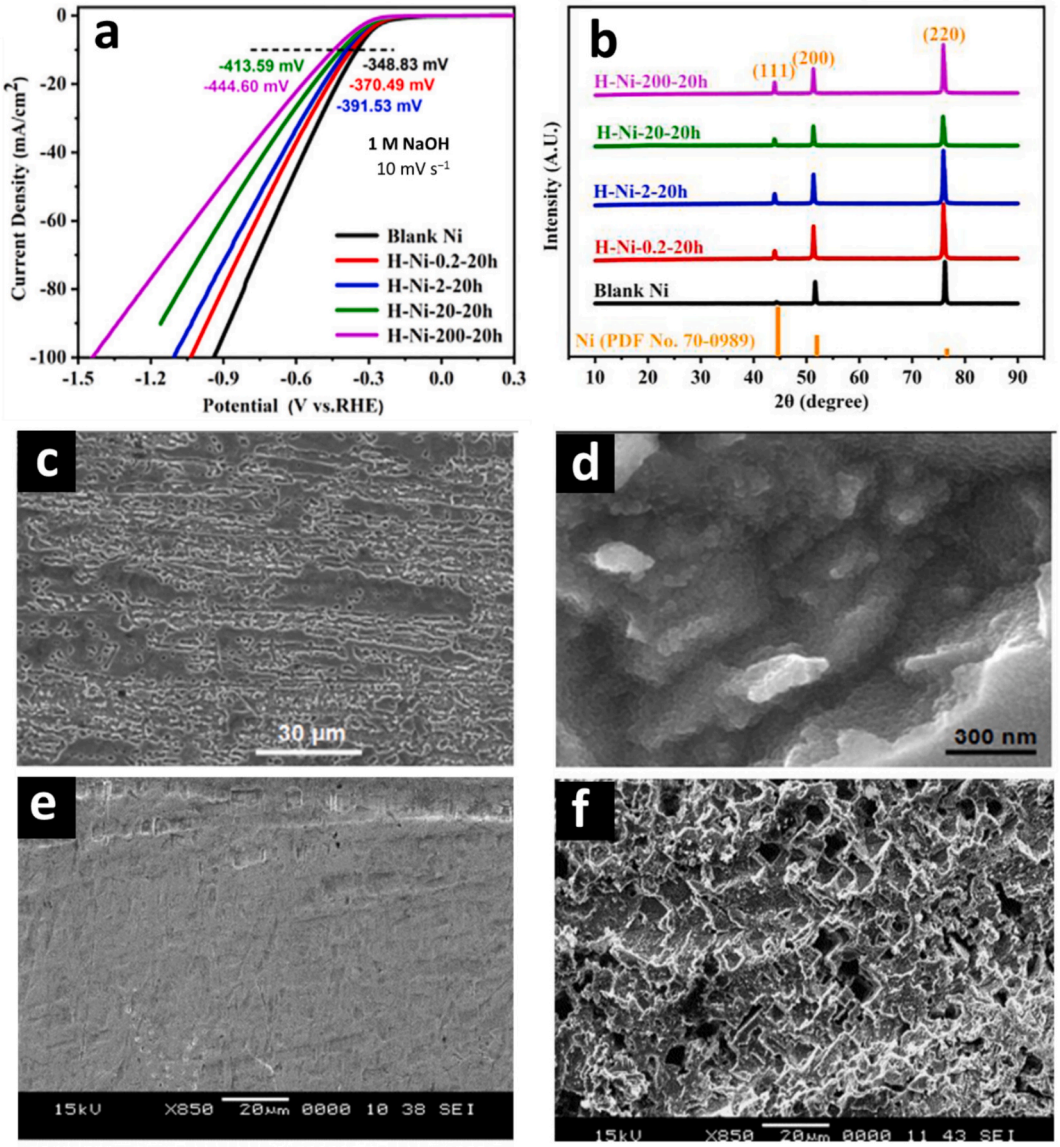

Fig. 20. Electrochemical restructuring under sustained operation highlights the strong coupling between applied current density, surface evolution, and catalytic performance. (a) LSV curves (after iR-correction) at a scan rate of 10 mV s^{-1} for the HER performances of the blank Ni electrode and the Ni cathodes after holding at several current densities (0.2, 2, 20, and 200 mA cm^{-2}) for 20 h in 1 M NaOH at 25 °C under N_2 and (b) the corresponding XRD analysis. SEM images of (c and d) copper cathode after electrolysis in CO_2-saturated DMF (0.1 M $TMABF_4$) at −1.8 V *vs.* Ag/AgCl, besides (e) an unused and (f) an extensively used tin cathode for electrochemical reduction of nitrate at −2.9 V *vs.* Ag/AgCl in 0.1 M K_2SO_4 + 0.05 M KNO_3 for 2.5 h.
Reproduced with permission from [183–185]

controlled by time, potential amplitude, and diffusion kinetics.

As such, electrochemical dealloying represents one of the most powerful electrochemical routes for generating metastable, high-energy surfaces with tunable catalytic properties. Its impact extends from nanoporous metals to advanced fuel cell catalysts and nanoscale hollow architectures, making it a central strategy in electrochemical surface engineering.

4.6. Cathodic corrosion

The cathodic corrosion phenomenon was discovered more than a century ago when Fritz Haber observed clouds dispersing from negatively polarized metals [176,177]. Haber attributed these clouds to the formation and succeeding destruction of alloys between the polarized metal and alkali metal cations. Afterward, cathodic corrosion was shortly reconsidered in the mid-1900 s [178,179]. Nevertheless, it remained mostly an empirical observation during the 20th century and only received growing attention in recent years [41,42,44,109,110,180]. Cathodic corrosion is an ambiguous electrochemical process that induces notable alterations in the surface structure of metal electrodes when exposed to sufficiently negative potentials, particularly in the presence of non-reducible cations such as alkali metal cations [42,44,109,110]. This phenomenon typically occurs at potentials below the equilibrium potential of the hydrogen evolution reaction. The expression "onset potential", while not precisely defined, is commonly used to refer to the least negative potential at which noticeable changes in the electrode surface become evident [33,109,110,116,181]. Typically, the surface of the cathodically corroded electrodes is marked by structural transformations and distinct etching features, including the formation of etching pits and/or nanoparticles. As a consequence, the EASA and the facet distribution of the electrodes are affected, but to a

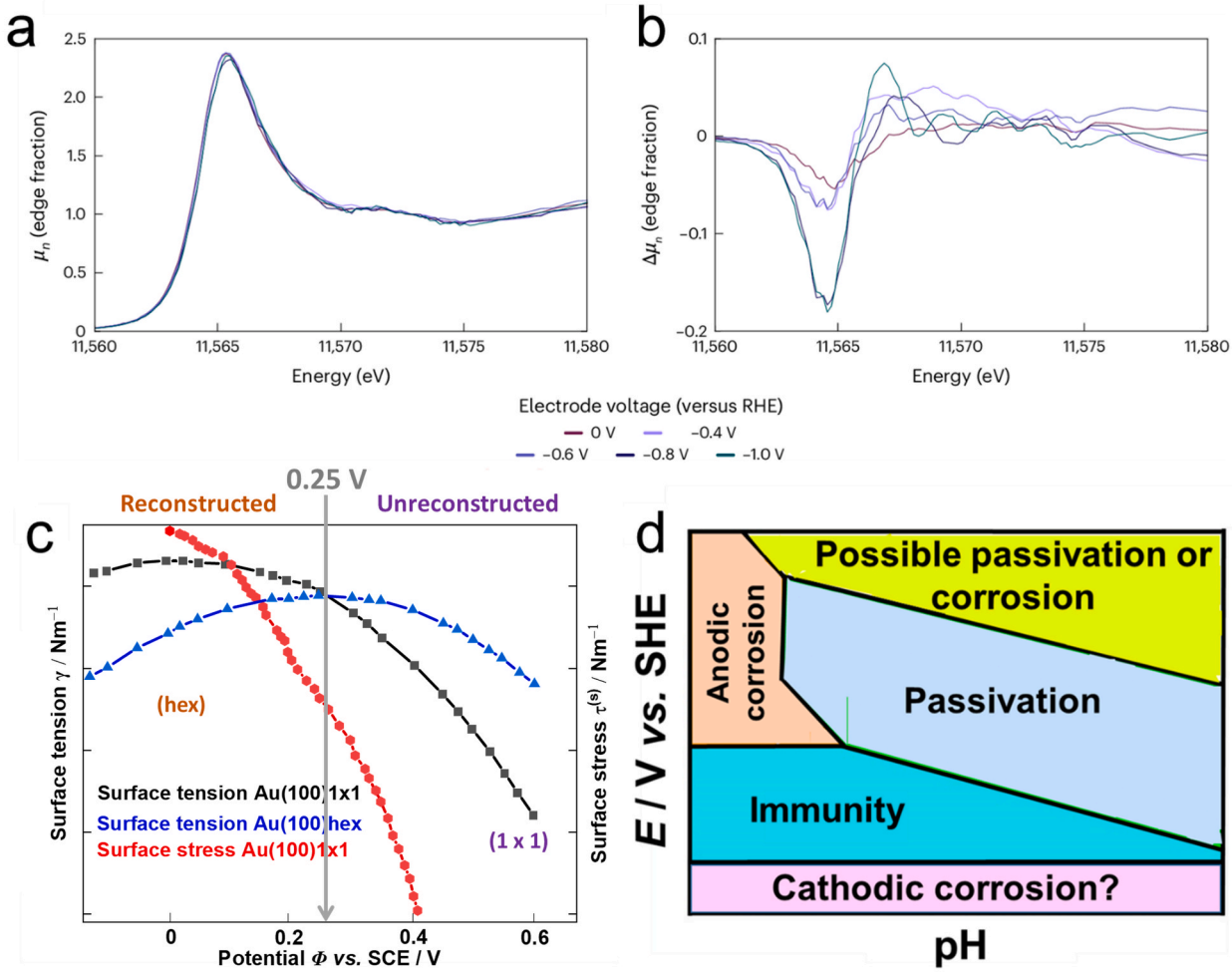

Fig. 21. HERFD-XANES of platinum nanoparticles and complementary interfacial properties. (a) Pt L_{III}-edge HERFD-XANES spectra of electrodes polarized at cathodic potentials in 10 M NaOH. The spectra shown are unsmoothed. (b) Corresponding smoothed difference spectra obtained by subtracting the smoothed spectrum at 0.4 V *vs.* RHE from each smoothed spectrum in (a). (c) Surface tension of Au(100) measured in 0.01 M $HClO_4$. (d) Schematic Pourbaix diagram for platinum, including the cathodic corrosion domain, with an approximate boundary separating the "immunity" region from the corrosion regime (for qualitative illustration only).
Reproduced with permission from [91,109,187]

variable extent depending on the applied electrochemical conditions [31,33,42,181]. Normally, these changes in the surface structure are connected to both the activity for a given reaction and the electrode stability. Hence, cathodic corrosion can be used to tailor metal surfaces, thus flexibly designing electrodes for various electrochemical systems. Furthermore, cathodic corrosion has been recognized as a facile surfactant-free top-down synthetic approach for fabricating shape- and size-controlled nanoparticles of metals, metal oxides, or alloys from bulk wires. The electrogenerated catalysts exhibit enhanced (electro)catalytic activity and/or selectivity for many energy conversion-related reactions [44,46,48,182].

4.6.1. Fundamental insights into the cathodic corrosion process

While cathodic corrosion can be applied to tailor the surface structure of metal electrodes and to the synthesis of nanoparticles, it also presents a significant challenge in various electrochemical conversion reactions that take place at high cathodic currents in the presence of alkali metal or organic cations. These reactions include HER, CO_2RR to hydrocarbons, nitrogen reduction reaction (NRR), ORR, and cathodic electro-conversion in organic electrosynthesis, among others. In this context, cathodic corrosion can lead to (undesired) substantial alterations in the surface structure of electrocatalysts, which may impact their stability and long-term performance. For example, the effects of applying different current densities (0.2, 2, 20, and 200 mA cm^{-2}) for 20 h on the HER performance of Ni electrodes in alkaline solutions have been examined. After Ni was used as an HER electrode, the intensity of the XRD diffraction peak of the Ni(111) facet increased, and the HER performance of the Ni electrode decreased by increasing the applied current density during the pre-electrolysis treatment, as shown in Fig. 20a and 20b [183]. This is a clear example of the changes in the surface structure, e.g., the crystallographic orientation of surface facets of Ni electrode upon cathodic polarization in the hydrogen evolution regime, in which this behaviour can be explained in the light of cathodic corrosion. Moreover, the Cu cathode corroded under prolonged electrolysis in DMF containing 0.1 M $TMeABF_4$ at −1.8 V *vs.* Ag/AgCl due to cathodic corrosion, which can be seen in Fig. 20c and 20d [184]. Furthermore, the electrochemical reduction of nitrate on a tin (Sn) cathode at −2.9 V *vs.* Ag/AgCl has been studied in 0.1 M K_2SO_4/0.05 M KNO_3 electrolyte [185]. An enhancement by a factor of 1.5 was noticed in the total electrolysis current between the first and the third experiment. The rise in both the reaction rate and the electrolysis current is attributed to the increase in the EASA of the electrode, due to the formation of small particles of Sn, caused by cathodic corrosion, something which could also be observed visually (Fig. 20e and 20f).

Given these considerations, advancing our fundamental understanding of the mechanisms, processes, and key parameters governing cathodic corrosion is critically important for research, development, and technological applications. Such insights can enable us to exert control over cathodic corrosion, either to prevent it and stabilize electrode surfaces during electrochemical reactions or to employ it to tailor metal surfaces and fabricate metal nanoparticles.

4.6.2. Mechanistic framework

Cathodic corrosion is a quite complex process; its mechanism involves numerous steps. The phenomenon is not yet fully resolved and is still under investigation. The phenomenon is not yet fully resolved and is still under investigation. Experimental and theoretical investigations have proved the requisite role of non-reducible cations (e.g., alkali metal cations) in triggering cathodic corrosion since no cathodic corrosion features were observed in the absence of cations [33,44]. Furthermore, density functional theory (DFT) calculations of the effect of adsorbed hydrogen (H_{ad}) on the potential-dependent surface energy show an equally crucial role of H_{ad} in cathodic corrosion [33]. In this respect, we have investigated the relevance of water and hydrogen evolution in the cathodic corrosion process [186]. Notably, cathodic corrosion does not take place in the absence of water. The presence of water at the interface is essential to obtain high surface excess charge densities in combination with strong hydrogen evolution. The role of water is discussed in detail in section 4.6.5.4. Furthermore, recent experimental evidence provides strong support for hydrogen-stabilized intermediates under cathodic polarization through X-ray absorption spectroscopy [187]. In this study, *operando* high-energy-resolution X-ray absorption near-edge structure experiments (HERFD-XANES) measurements reveal systematic electronic changes for platinum under strong cathodic polarization that are characteristic of hydride formation (Fig. 21a and 21b). As the electrode potential is shifted systematically from positive values to negative potentials, the Pt whiteline progressively broadens while the absorption edge shifts slightly to higher energies. Difference spectra referenced to a moderate potential display a distinct negative peak accompanied by a broad positive shoulder at higher energies, with the magnitude of these features increasing monotonically as the potential becomes more negative. Importantly, the overall peak area remains essentially unchanged, indicating that the spectral evolution reflects a redistribution of unoccupied electronic states rather than a simple change in oxidation state. The persistence, shape, and potential dependence of these features are consistent with hydrogen incorporation into the Pt lattice, leading to the formation of hydrogen-rich PtH_x phases. To put it simply, metal cations and hydrogen atoms are co-adsorbed on the corroding surfaces, typically at potentials lower than the pzc of the polarized metal, as illustrated by theoretical computations [33]. As shown in Fig. 21c, the surface tension shows a maximum at the pzc, where the surface has no excess charge. Lowering the electrode potential relative to the pzc induces large surface stress [91]. As such, surface stress is altered as a function of the applied potential, which is supposed to influence cathodic corrosion. This stress, together with strong adsorption effects, can destabilize the surface lattice and promote atomic rearrangement. Consequently, the pronounced structural transformations observed during cathodic corrosion can be understood as the combined result of extreme surface charging, hydrogen incorporation, cation stabilization, and stress-induced lattice weakening.

Under sufficiently negative potentials, this destabilization leads to the detachment of metal atoms from the parent surface. Interestingly, investigations of the structural evolution of Au electrodes during cathodic corrosion, particularly the early stages of octahedral nanocrystal formation, demonstrate that nanocrystal growth proceeds through a coupled dissolution–redeposition process [188]. The initial stages of cathodic corrosion of Au at sufficiently negative potentials in NaOH solutions are characterized by the formation of etching pits resulting from the dissolution of Au species. As corrosion proceeds, the concentration of dissolved Au species

near the interface increases, eventually reaching a critical value at which electrocrystallization is initiated, preferentially at the wire tip. This region is especially susceptible to corrosion due to its high electric field strength and elevated density of surface defects, which promote nucleation. In general, both the applied potential and the NaOH concentration influence the rates of Au dissolution and redeposition and thus govern the nucleation density and growth of nanocrystals. To illustrate the temporal evolution at a fixed potential, Fig. 22a–22r present SEM micrographs of Au electrodes polarized at −1.5 V *vs.* RHE in 10 M NaOH for durations ranging from 2 s to 30 min. After only 2 s of polarization (Fig. 22a and 22b), octahedral nanocrystals with imperfect shapes already appear at the tip region of the wire (approximately 8 μm in length), coexisting with pronounced etching pits. At locations farther from the tip (orange-rimmed area), etch pits dominate the surface morphology (Fig. 22a and 22c), indicating that metal dissolution initially exceeds redeposition. These observations confirm that the two processes occur simultaneously, but with dissolution prevailing at the onset of corrosion. With increasing polarization time up to 60 s, the density of octahedral nanocrystals increases substantially, and their shapes become progressively better defined (Fig. 22a–i), indicating that redeposition becomes increasingly important relative to dissolution. After approximately 5 min of polarization, the surface morphology changes markedly: the area covered by octahedral nanoparticles decreases, while new fractal nanostructures begin to grow away from the tip region (Fig. 22j–l). Further extension of the polarization time to 15 min leads to a dramatic increase in the density of these fractal structures, while only a limited region (about 10 μm near the tip) retains octahedral nanocrystals (Fig. 22m–o). After 30 min of polarization, homogeneously distributed multi-armed nanostructures are observed across the entire surface exposed to the electrolyte (Fig. 22p–r). The emergence and growth of fractal and multi-armed morphologies for polarization times ≥ 5 min indicate a pronounced enhancement of redeposition rates over time. Beyond approximately 30 min, no significant additional morphological changes are detected, suggesting the establishment of a diffusion-

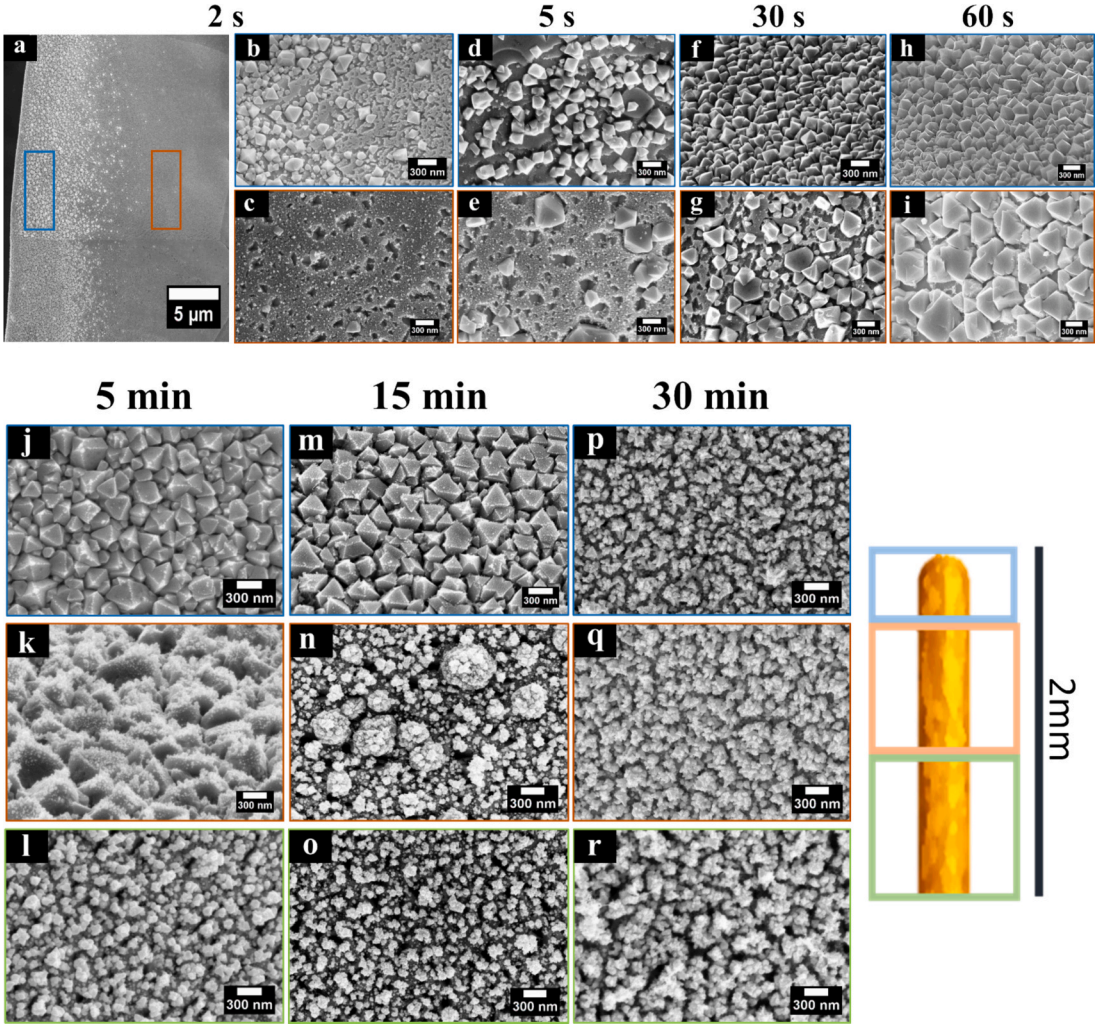

Fig. 22. Time-dependent evolution of Au surface morphology during cathodic corrosion in 10 M NaOH at −1.5 V *vs.* RHE. SEM images of Au electrodes after polarization for (a–c) 2 s, (d,e) 5 s, (f,g) 30 s, (h,i) 60 s, (j–l) 5 min, (m–o) 15 min, and (p–r) 30 min. A schematic representation of the corresponding local structural transformation of the Au wire is shown alongside the SEM series.
Reproduced with permission from [188]

limited regime. These structural trends are consistent with independent measurements of facet distribution and electrochemically active surface area. The highest contribution of (111) facets corresponds to surfaces densely covered with well-defined octahedral nanocrystals. At the same time, the progressive increase in EASA with polarization time reflects the formation of high-surface-area fractal and multi-armed structures. Overall, the systematic evolution from etch pits to faceted nanocrystals and ultimately to hierarchical nanostructures provides compelling evidence that cathodic corrosion–induced nanocrystal growth is governed by a dynamic interplay between metal dissolution and redeposition.

Taken together, the emerging mechanistic picture of cathodic corrosion is schematically illustrated in Fig. 23.

Panel 1 depicts the initial state under extreme cathodic polarization in alkaline solution (e.g., NaOH), at potentials well below 0 V versus the reversible hydrogen electrode (RHE). Under these conditions, the Au surface carries a high excess negative charge density and supports vigorous hydrogen evolution. The surface becomes densely covered with adsorbed hydrogen (H_{ad}), while alkali metal cations (e.g., Na^+) accumulate within the electrical double-layer to compensate for the interfacial charge. At sufficiently negative potentials and high hydrogen chemical potential, hydrogen is not limited to surface adsorption but can penetrate the near-surface region, leading to the formation of hydrogen-rich or hydride-like surface phases. This hydrogen incorporation modifies the electronic structure of Au and induces lattice expansion and strain.

Panel 2 represents the onset of structural destabilization. The combined effects of extreme cathodic polarization, subsurface hydrogen incorporation, and cation stabilization weaken Au–Au bonding at the interface. Rather than simple dissolution of neutral atoms, the process is thought to involve transient, negatively charged Au species, which are stabilized within the highly polarized double-layer. These species may be viewed as hydrogen-stabilized, anionic Au intermediates whose formation becomes energetically accessible only under intense electric fields and high surface hydrogen coverage.

Panel 3 illustrates the migration of these transient species away from the immediate surface region. As they diffuse into regions of lower field strength or encounter interfacial water molecules, charge redistribution occurs. In this step, water reduction continues to generate H_2 and OH^-, while the hydrogen-stabilized Au species are oxidatively converted back to metallic Au. This step highlights the intrinsically non-equilibrium nature of cathodic corrosion: reduction and reoxidation processes occur locally and dynamically within the interfacial region.

Panel 4 shows the fate of the regenerated metallic Au atoms. They may redeposit onto the parent surface, contributing to roughening and faceting, or nucleate in solution to form nanoparticles. The competition between redeposition and nucleation depends on local mass transport, electric field gradients, and interfacial supersaturation conditions.

Taken together, this scheme reflects a unified mechanistic framework in which four elements act cooperatively: (i) extreme cathodic polarization generating high excess surface charge, (ii) intense hydrogen adsorption and subsurface incorporation leading to hydride-like surface phases, (iii) stabilization of negatively charged intermediates by non-reducible electrolyte cations within the electrical double-layer, and (iv) stress-induced lattice destabilization that facilitates atom detachment and restructuring.

Despite efforts to simplify the mechanism of cathodic corrosion, as illustrated in Fig. 23 based on accumulated experimental evidence, a unified mechanistic description remains elusive. A central challenge arises from the fact that different mechanistic pathways may dominate depending on the material system and electrochemical conditions. While hydride-stabilized intermediates under cathodic polarization have been supported by X-ray absorption spectroscopy, providing a compelling explanation for Pt electrodes, their relevance is less clear for systems such as Au, where stable hydride formation is unlikely. This observation indicates that hydride formation cannot be considered a universal requirement and that alternative pathways must contribute to surface destabilization. A major limitation in resolving these mechanistic questions is the scarcity of direct *operando* insights. Cathodic corrosion proceeds under

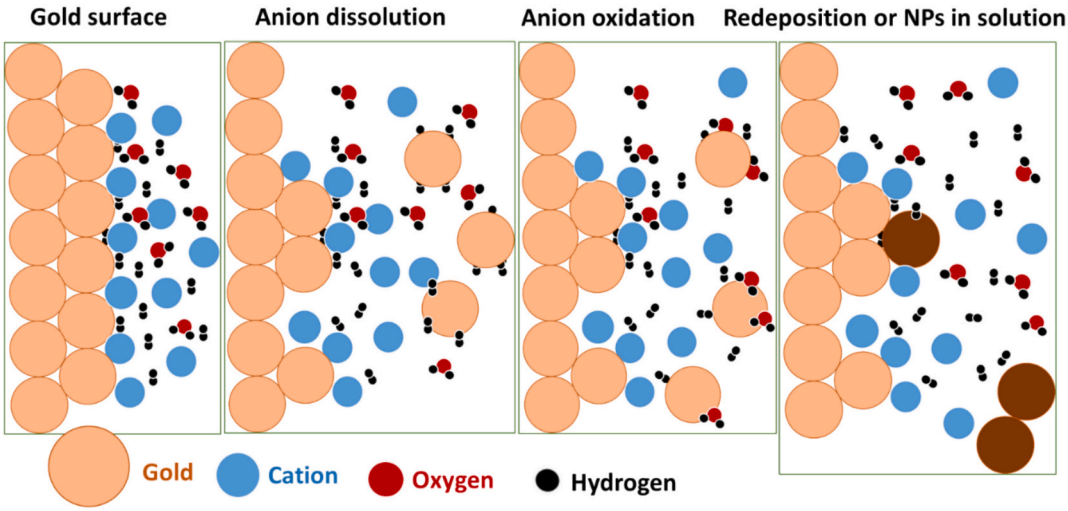

Fig. 23. Schematic illustration of the proposed mechanism of cathodic corrosion of Au under cathodic polarization in alkali metal hydroxide electrolyte, showing hydrogen adsorption and incorporation, cation accumulation in the electrical double-layer, formation and migration of intermediate Au species, and their subsequent redeposition or nanoparticle nucleation.

particularly harsh conditions, including highly alkaline environments, vigorous hydrogen evolution, and large current densities, which complicate the application of conventional *in-situ* techniques. As a result, transient intermediates and rapid structural transformations remain difficult to capture experimentally. Addressing these challenges will require the development of advanced *operando* approaches capable of probing electrified interfaces under such extreme conditions.

4.6.3. *Pourbaix diagram of cathodic corrosion*

Pourbaix diagrams, also known as electrochemical equilibrium or *E*-pH diagrams, are valuable tools for understanding the surface structure and thermodynamic stability of diverse species, including metals, oxides, ions, and hydroxides, in aqueous solutions [189]. These diagrams can identify spontaneous electrochemical reactions, predict their products, and determine the corrosive conditions for a given material based on electrode potential and pH. However, it is worth noting that despite the availability of numerous Pourbaix diagrams for various systems, they do not include the cathodic corrosion process. In this respect, a tentative version of the Pourbaix diagram that incorporates the cathodic corrosion regime is presented in Fig. 21d. This updated diagram builds upon the standard Pourbaix diagram for Pt [189] but takes into account the determined onset of cathodic Pt corrosion in alkaline solutions [110]. Notably, cathodic corrosion also occurs at lower pH values [44]. The process of hydrogen evolution, which is associated with cathodic corrosion, leads to the generation of OH^- ions, significantly elevating the near-electrode pH relative to the bulk pH [190,191]. To account for this effect, the cathodic corrosion onset at lower pH values is illustrated in the diagram, assuming a hypothetically high near-electrode pH, resulting in a constant onset potential with respect to the normal hydrogen electrode. However, it is important to acknowledge that Pourbaix diagrams are representations of systems in thermodynamic equilibrium. Therefore, the inclusion of cathodic corrosion onset potentials, similar to those shown in Fig. 21d, may not stringently align with the principles of equilibrium thermodynamics. These onset potentials were determined for systems with unknown concentrations of metastable reaction species and under conditions where the near-electrode pH deviates from the bulk pH. In addition to identifying onset potentials, future research should aim to establish equilibrium potentials for cathodic corrosion. Furthermore, updated Pourbaix diagrams could explicitly consider the role of electrolyte cations. This could, for example, be achieved by introducing a cation concentration axis. Despite the need for further refinement, the current illustrative Pourbaix diagram highlights that the cathodic behavior of metals can be more complicated than commonly assumed in the context of cathodic protection [109].

4.6.4. *The metal-electrolyte interface*

The core principle of electrochemistry is located at the interfacial boundary between an electron-conducting surface and an ionic solution, governing the observable outcomes of electrochemical reactions. To illustrate, we propose a schematic model of the double-layer region during cathodic corrosion (without hydrogen adsorption and hydrogen evolution), as depicted in Fig. 24. Given that the metal surface becomes negatively charged during cathodic corrosion, a balancing countercharge arises from the alkali metal cations in the electrolyte. This charge separation results in the formation of the so-called electrical double-layer, which can most simply be described as a plate capacitor, with the electrode on one side and the adsorbed ions on the other side [192–194]. This configuration

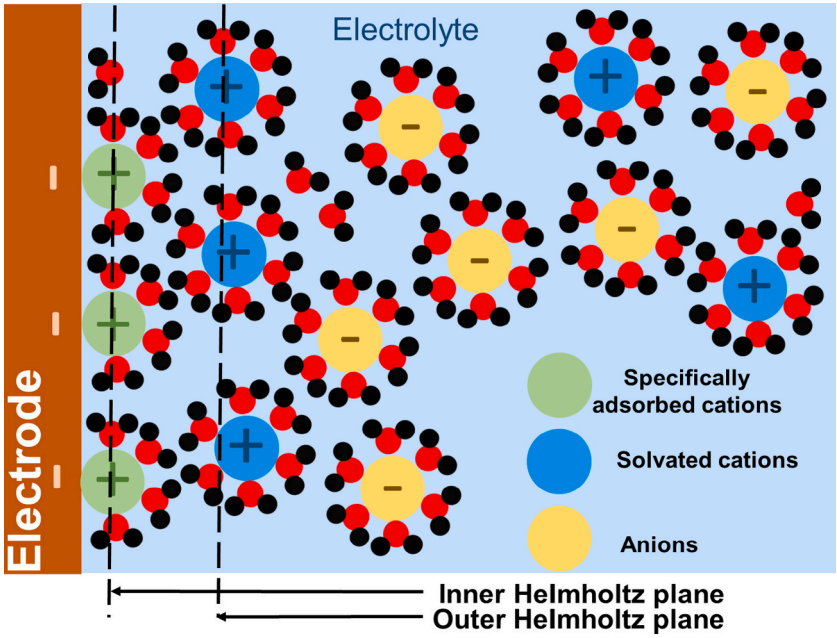

Fig. 24. Schematic depiction of the Stern–Gouy–Chapman model illustrating a negatively charged metal–electrolyte solution interface. The inner Helmholtz plane denotes the location of specifically adsorbed and partially solvated cations, while the outer Helmholtz plane represents the plane of closest approach for the hydrated cations.

aligns with the rigid Helmholtz double-layer model [195]. Previous theoretical studies have shown that alkali metal cations can specifically adsorb onto metal electrode surfaces at low overpotentials within the hydrogen evolution region [41]. Consequently, during cathodic corrosion, alkali metal cations are anticipated to lose part of their hydration shell and become specifically adsorbed to the metal electrodes, as proposed in Fig. 24. This ion adsorption at the electrode surface occurs when electron transfer reactions are absent, effectively compensating for the excess charge on the electrode and maintaining electroneutrality. The plane where the charge centers of the specifically adsorbed ions are located constitutes the inner Helmholtz plane (IHP). Moreover, the layer containing the heavily charged solvated ions is referred to as the outer Helmholtz plane (OHP) [194].

4.6.5. *Parameters influencing cathodic corrosion*

The surface structure of cathodically corroded metal electrodes is influenced by a wide range of experimental parameters. These include the electrode material and its initial surface facets, the applied potential, the nature and concentration of cations, as well as the

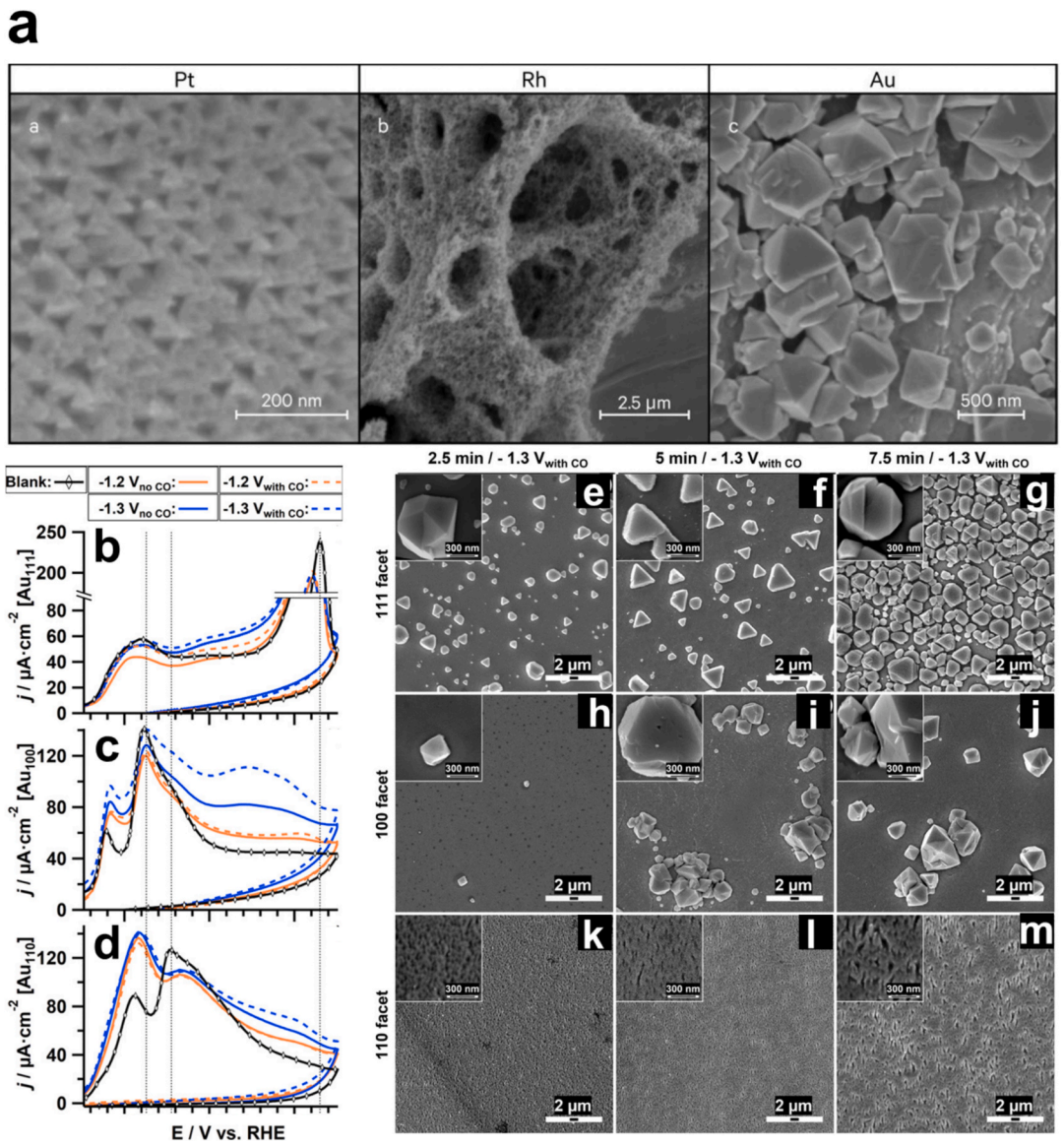

Fig. 25. Cathodic corrosion as a material- and facet-dependent restructuring process. (a) SEM images of Pt, Rh, and Au after cathodic corrosion for 1 min in 5 M NaOH. Pt and Rh were corroded at −0.8 V *vs*. RHE, whereas Au was corroded at −1.5 V *vs*. RHE. Cyclic voltammograms of Au single crystals in 0.05 M H_2SO_4 before and after cathodic polarization in 10 M NaOH for 2.5 min in the absence and presence of CO at −1.2 V and −1.3 V *vs*. RHE (85% IR-corrected) for (b) Au(111), (c) Au(100), and (d) Au(110) electrodes. SEM images of the 111 facet (e-g), 100 facet (h-j), and 110 facet (k-m) of anisotropic surface corrosion in the form of pitting and nanocrystal formation as a function of time (2.5–7.5 min) at a corrosion potential of −1.3 V *vs*. RHE in 10 M NaOH in the presence of CO.
Reproduced with permission from [109,116]

choice of solvent.

4.6.5.1. Electrode material and initial surface facets. The surface orientation preferences and corrosion features produced by cathodic corrosion exhibit pronounced variations depending on the electrode material. Moreover, cathodic corrosion occurs on metal electrodes with widely differing structural complexity, ranging from extended bulk surfaces and well-defined single crystals to nanoscale architectures. These distinct initial states vary in crystallographic orientation distribution, defect density, grain boundary content, surface area, and thermodynamic stability, all of which govern atomic mobility, surface reconstruction, and dissolution behavior under cathodic polarization.

SEM images depicting Pt, Rh, and Au electrodes, cathodically corroded in 5 M NaOH for 60 s, are displayed in Fig. 25a [33,109]. Of note, Pt and Rh were corroded at −0.8 V *vs.* RHE, while Au was corroded at −1.5 V *vs.* RHE. Importantly, cathodic corrosion in 5 M NaOH for 60 s favorably leads to (111) sites on Au and (100) sites on Pt and Rh. Additionally, the SEM micrographs reveal different etching features depending on the electrode material. Furthermore, the onset of cathodic corrosion varies by metal polarized under the same conditions: Pt and Rh initiate corrosion at −0.4 V *vs.* RHE, while Au begins at −0.7 V *vs.* RHE. These distinctions between Pt, Rh, and Au underscore the metal-specific response to cathodic corrosion. These variations arise from differences in the mobility of surface atoms of the metals during cathodic polarization and the preferential adsorption of sodium on the types of steps that match the types of sites formed.

Interestingly, cathodic corrosion features are influenced not only by the electrode material but also by the initial surface facets, revealing a crucial aspect of cathodic corrosion: it occurs anisotropically [42,116]. For example, the cathodic corrosion of Au surfaces as a function of crystal orientation in 10 M NaOH was investigated to determine to what extent cathodic corrosion is anisotropic (Fig. 25b-m). Additional experiments were performed to gain insights into the effect of the presence of CO during cathodic corrosion [116].

In Fig. 25a–d, cyclic voltammograms obtained before and after cathodic corrosion experiments at −1.2 V and −1.3 V *vs.* RHE in 10 M NaOH for 2.5 min in the absence (solid lines) and the presence (dashed lines) of CO are depicted for the (111), (100), and (110) basal planes. For an Au(111) surface, the distinguishing feature of an infinite (111) terrace at 1.63 V *vs.* RHE is a decrease in current density and shifts to less positive potentials after cathodic corrosion. This shift indicates the generation of large finite-length (111) terraces with step defects. Therefore, this particular change in the voltammogram reveals the introduction of step-site defects in the extended (111) plane upon corrosion. These formed stepped facets likely correspond to the nanocrystallite formation on the gold surface (Fig. 25e-g). Furthermore, the imperfections in the Au(111) surface display nonmonotonic behavior as a function of the applied potential.

For the (100) surface, the characteristic feature at 1.42 V *vs.* RHE primarily slightly decreases in peak intensity upon cathodic corrosion (Fig. 25c). Nevertheless, surfaces corroded more pronouncedly by lowering the applied potentials, exhibiting less of a decrease in the number of (100) terraces than surfaces corroded under milder conditions. Despite this, the peak is still lower than that observed for an uncorroded surface. Corrosion of the (100) terraces is further supported by an enhancement of step-site defects (feature at 1.38 V *vs.* RHE) upon increasing the applied negative potentials. It is observed that corrosion of the (100) plane results in a considerable increase in the number of stepped (111) terrace sites, as revealed by an increase in charge in the $1.46 < E < 1.62$ V *vs.* RHE regime. Seemingly, corrosion generates specifically (111)-type step defects into the (100) surface and thus transitions the overall surface morphology in the direction of the {111} plane (Fig. 25h-j).

Regarding the cathodic corrosion features on the most open of the basal planes, (110), Fig. 25d illustrates two distinctive features concerning infinite terrace lengths: a weaker one at 1.41 V *vs.* RHE and a stronger one at 1.45 V *vs.* RHE. After cathodic corrosion, the stronger feature displays a decrease in current density. However, similar to what is noticed for the corrosion of the (100) plane, this decrease in peak current density is less pronounced when more negative potentials are applied. As for the weaker feature, it consistently rises with the corrosion potential, with no observable shift. There is also an increase in charge within the regime characteristic of finite-length stepped (111) terraces. These observations can be attributed to the transformation of the (110) plane into a surface enriched with (111)-type sites. The primary (110) peak exhibits a lesser decrease in current density as more corrosive potentials are applied, likely because finite-length (111) terraces contribute charge over a broad potential range. Although the number of (110) terrace sites is expected to decrease further by lowering the applied potentials, the contribution of charge by finite-length (111) terraces increases.

Notably, all surfaces exhibit a similar trend when comparing cyclic voltammograms of crystals corroded in the absence and presence of CO. Taking the Au(100) surface as an example, it is observed that there is a slight increase in charge when CO is present during corrosion, especially at −1.3 V *vs.* RHE (Fig. 25c). However, although the peak charge rises (indicative of an increase in active sites), the overall shape of the voltammograms is similar, with only minor alterations in the stepped (111) regime. Consequently, it can be concluded that the presence of CO enhances the rate of corrosion, but the types of sites generated during the corrosion process are very similar, with a slight increase in stepped (111) sites. This conclusion can be extended to the other basal planes as they exhibit a similar trend to that discussed for the (100) face.

Additional insights into the facet-dependent behavior of cathodic corrosion can be gleaned from the SEM images, which depict the time-dependent evolution of the different basal planes (Fig. 25e-m). These SEM images reveal that the morphological changes of the basal planes vary depending on the facet as a function of corrosion time. For the initially flat (111) face, only minor signs of pitting and etching are observed, but triangular and octahedral nanocrystals form after cathodic polarization at −1.3 V *vs.* RHE. In contrast, the {100} facet shows minor surface pitting before nanocrystal formation under sufficiently negative potentials, particularly at −1.3 V *vs.* RHE for more than 5 min. Notably, there are some differences in the nanocrystal formation between (100) and (111). On the {100}

facet, nanocrystals tend to cluster together, and the resulting nanocrystallites have shapes influenced by a truncation process (partial cutting of polyhedron vertices, resulting in new faces) and/or form aggregates of crystallites, with some of the smaller individual crystallites adopting octahedral shapes. In contrast, the corrosion behavior of the (110) facet is characterized by surface etching and pitting, as evident in Fig. 25k–m. Importantly, the SEM images of corroded electrodes in the absence and presence of CO are mostly identical. These findings highlight that cathodic corrosion is a structure-selective process that reshapes surfaces according to thermodynamic stability and atomic mobility under extreme cathodic polarization.

Strong crystallographic anisotropy in cathodic corrosion has also been directly demonstrated by another example using spherical monocrystalline platinum electrodes, which expose multiple low-index facets within a single continuous surface [42]. Under strongly cathodic polarization in alkaline electrolyte, corrosion does not proceed uniformly but develops through facet-dependent pathways that reflect the atomic structure of each orientation. The earliest stage is characterized by the formation of symmetry-specific etch pits: square pits on Pt(100), triangular pits on Pt(111), and rectangular pits on Pt(110). These geometries indicate that atom removal is governed by surface symmetry and coordination rather than by isotropic dissolution. Notably, the relative corrosion resistance differs from anodic conditions, with Pt(111) exhibiting the highest susceptibility and Pt(110) the greatest stability. As corrosion progresses, the pit morphology evolves in a facet-dependent manner. On Pt(100) and nearby high-index surfaces, initially well-defined pits destabilize preferentially along (111) directions, producing concave octagonal shapes that subsequently develop branched features resembling diffusion-limited growth. In contrast, pits on Pt(111) primarily increase in density and eventually overlap, while those on Pt(110) remain comparatively sparse and evolve more gradually. These observations demonstrate that cathodic corrosion proceeds through orientation-dependent stages controlled by crystallography, highlighting the central role of surface atomic structure in determining both corrosion kinetics and resulting nanostructure formation.

Fig. 26 illustrates the time-resolved morphological evolution of a spherical Pt single crystal polarized at −1.0 V for durations ranging from 1 to 25 min. The top row presents low-magnification images of the entire electrode surface, revealing progressive roughening with time. Roughening is most pronounced in the region between the (100) and (111) facets, where the affected zone broadens substantially during polarization, whereas transitions involving the (110) facet show comparatively minor changes. This behavior indicates that stepped surfaces inherit the anisotropic corrosion tendencies of the adjacent basal planes. Higher-

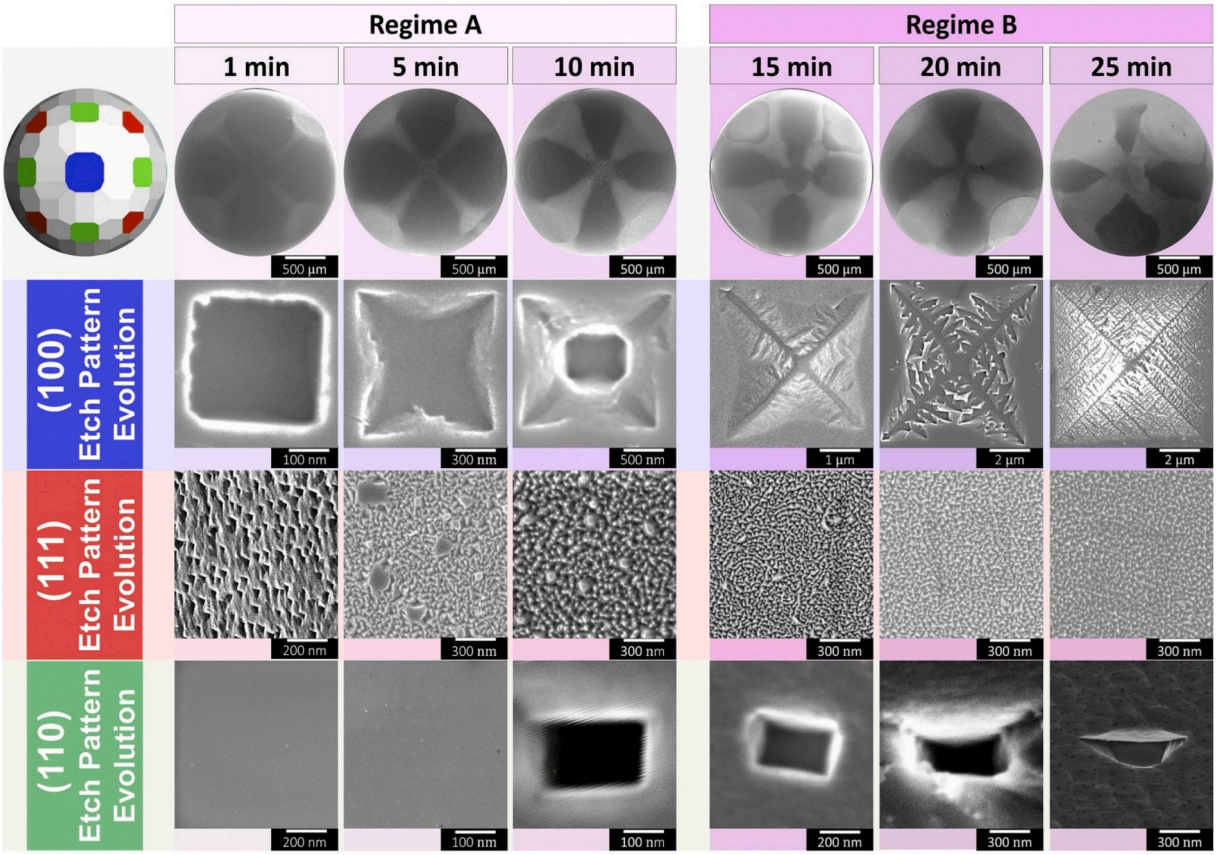

Fig. 26. Time-dependent evolution of surface morphology during cathodic corrosion at E = − 1.0 V, shown by SEM images of a spherical Pt electrode after 1, 5, 10, 15, 20, and 25 min of polarization. The top row presents the entire electrode, while the lower rows display higher-magnification views of the (111), (100), and (110) facets.
Reproduced with permission from [42]

magnification images of the individual facets (rows two through four) reveal distinct facet-specific corrosion patterns. On the Pt(100) surface, corrosion begins with isolated square pits having smooth, well-defined edges. With increasing polarization time, these pits deepen and transform into pyramidal pits. At longer times, the pit walls destabilize and develop branching arms that produce a self-similar roughened morphology, consistent with directional growth along preferred crystallographic orientations. The Pt(111) facet initially exhibits triangular pits whose number increases steadily with time. Rather than forming branched structures, these pits expand laterally and eventually merge, resulting in generalized surface roughening. In contrast, the Pt(110) surface shows rectangular pits that are fewer in number and evolve more slowly, gradually becoming elongated or wedge-like without pronounced fractal development.

Across all facets, pit size, pit density, and apparent roughness increase with polarization time, but the evolution pathways differ markedly between orientations. The images therefore reveal two distinct corrosion regimes: an early stage dominated by isolated, symmetry-controlled pit formation and a later stage characterized by more complex roughening processes whose nature depends strongly on the crystallographic orientation.

Recent *operando* studies further demonstrate that cathodic corrosion happens across length scales to nanoscale catalysts (Fig. 27a-f)

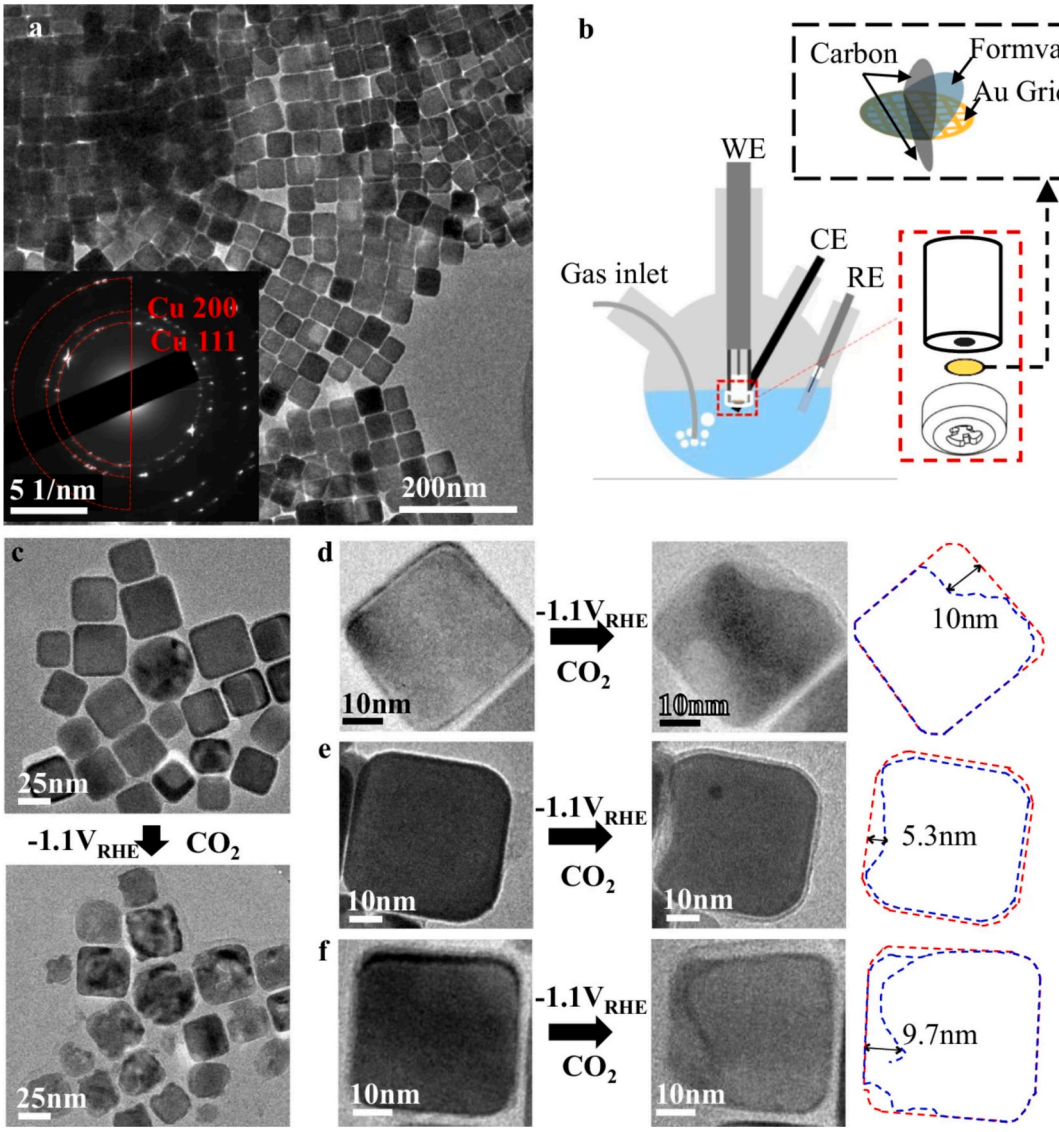

Fig. 27. Structural evolution of Cu nanocubes under cathodic CO_2 reduction conditions. (a) Representative bright-field TEM image of ~ 40 nm Cu nanocubes; the inset shows the selected-area electron diffraction pattern confirming metallic Cu. (b) Schematic of the identical-location TEM (IL-TEM) setup for studying Cu catalysts under cathodic conditions using a rotating disk electrode with a PTFE cap and a carbon-coated Au TEM grid. (c–f) IL-TEM bright-field images before and after treatment at −1.1 V *vs.* RHE in CO_2-saturated 0.1 M $KHCO_3$ for 20 min, highlighting morphology changes (outlined) that exceed the thickness of the native surface oxide layer.
Reproduced with permission from [86]

[86]. Using identical-location transmission electron microscopy (IL-TEM) (see Fig. 27b) combined with *in-situ* spectroscopic measurements and theoretical analysis, Cu nanocubes were shown to undergo pronounced structural reconstruction when polarized beyond a critical cathodic threshold (approximately −0.4 V *vs.* RHE in 0.1 M $KHCO_3$), a process attributed to alkali cation–induced cathodic corrosion. The presence of non-reducible alkali cations is found to be essential, consistent with the broader mechanistic picture of cathodic corrosion in alkaline and near-neutral electrolytes. Direct IL-TEM observations before and after polarization at −1.1 V *vs.* RHE in CO_2-saturated 0.1 M $KHCO_3$ for 20 min revealed that nearly all Cu particles within the same field of view exhibited clear morphological changes, irrespective of their initial size and shape (Fig. 27c). Importantly, for Cu nanocubes, these structural modifications were not limited to the surface but extended deep into the particle core, significantly exceeding the estimated thickness of pre-existing oxide layers, indicating that simple reduction or dissolution of surface oxides cannot account for the observed transformation. These findings demonstrate that cathodic corrosion can dominate catalyst restructuring even under moderate reaction potentials and that controlling the initial morphology alone is insufficient for achieving long-term stability. Conversely, operation at less negative potentials during CO reduction preserved the nanocube geometry and enabled a more stable selectivity advantage over spherical nanoparticles. This study highlights that cathodic corrosion is not restricted to bulk electrodes but is a general phenomenon affecting nanoscale electrocatalysts, thereby linking classical corrosion processes to the dynamic restructuring of catalytic materials under reducing conditions.

4.6.5.2. Electrode potential. The applied electrode potential is a central parameter governing cathodic corrosion, as it directly controls hydrogen evolution, interfacial charge density, surface stress, and ultimately atomic mobility. Corrosion typically initiates only beyond a material-dependent threshold located below the hydrogen evolution equilibrium potential. Although the precise "onset potential" cannot be rigorously defined due to the unknown concentration and nature of transient intermediates under strongly reducing conditions, cyclic voltammetry combined with SEM analysis provides reliable indicators through changes in facet distribution, EASA, and morphology [109,181,188]. Importantly, the onset potential depends on the electrode material and shifts moderately with electrolyte concentration and cation identity, reflecting the coupled nature of potential and interfacial environment.

Platinum provides a clear example of this threshold behavior [110]. SEM micrographs of Pt electrodes polarized between −0.2 and −0.8 V *vs.* RHE show virtually no detectable morphological changes at mild negative potentials. Surfaces treated at −0.2 to −0.5 V appear essentially flat at the SEM scale, despite voltammetric evidence for subtle structural changes, highlighting that early stages of corrosion may occur below the spatial resolution of conventional microscopy (Fig. 28a-c). Pronounced roughening becomes evident only at potentials lower than −0.6 V, where the surface develops significant nanoscale corrugation across grains and grain boundaries, consistent with modest increases in electrochemically determined roughness factors (Fig. 28d-f). At these potentials, well-defined etch

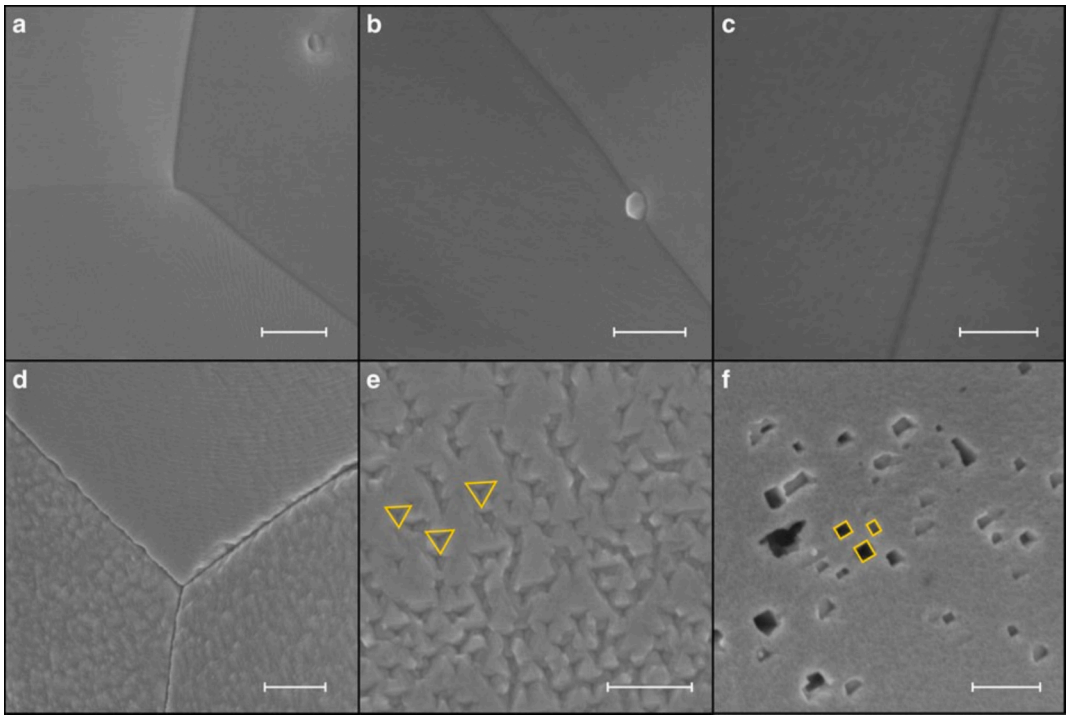

Fig. 28. SEM images of Pt electrodes after polarization at −0.2 V (a), −0.4 V (b), −0.5 V (c), −0.6 V (d,e), and −0.8 V (f) *vs.* RHE. Panels (e,f) highlight three representative etch pits (outlined) demonstrating similar shape and crystallographic orientation. Scale bars: 300 nm (a,b,d–f) and 100 nm (c).
Reproduced with permission from [110]

pits also emerge. Triangular pits and quasi-rectangular pits with ~ 90° angles appear on different grains, with identical orientation within each grain, demonstrating that corrosion proceeds anisotropically along crystallographic directions. Notably, no nanoparticles are observed, indicating that the surface area increase originates primarily from pit formation and corrugation rather than dissolution–redeposition processes.

Additionally, gold electrodes provide a particularly clear illustration of the influence of electrode potential on cathodic corrosion because their surface evolution proceeds through well-defined morphological stages. In concentrated alkali metal hydroxide electrolytes, mild cathodic polarization initially produces etching pits indicative of localized metal dissolution. As the potential becomes more negative, the corrosion process intensifies and transitions to the formation of faceted nanostructures generated through coupled dissolution and redeposition. SEM micrographs recorded after 60 s polarization in 10 M NaOH at potentials between −1.0 and −1.9 V *vs.* RHE reveal a clear evolution in surface morphology (Fig. 29a-j). At −1.0 V, the surface exhibits etch pits across the immersed region, indicating the onset of Au dissolution. The pit density is higher at the wire tip than along the rest of the wire, due to the higher local electric field at regions of high curvature. As the potential becomes more negative, cathodic corrosion changes from simple etching to a dissolution–redeposition process, leading to the nucleation and growth of octahedral nanocrystals. At moderately negative potentials (e.g., at −1.2 V), these nanocrystals form preferentially near the tip, while rectangular etch pits remain dominant elsewhere. At −1.5 V and beyond, octahedral nanocrystals cover most of the corroded region. Their size decreases and their density increases as the potential is further lowered, indicating that stronger driving forces favor rapid nucleation over slower, more ordered crystal growth. Interestingly, particles formed at intermediate potentials (around −1.5 V) are often more well-defined than those produced at more extreme polarization, suggesting that excessively high driving forces promote structural disorder.

A similar potential dependence is observed in 10 M KOH, although with distinct morphological details. At −1.1 V *vs.* RHE, corrosion affects only part of the immersed wire, producing a corrugated tip region and triangular pits further away (Fig. 30 a-j). As the potential becomes more negative, the corroded length increases until the entire wire is affected ($E \leq -1.4$ V). Simultaneously, the morphology evolves from isolated pits to surfaces increasingly covered by nanoparticles. At intermediate potentials, irregular nanoparticle clusters form at the tip, while triangular pits become more numerous along the wire. Further lowering the potential leads to dense, preferentially oriented nanoparticles extending over the full surface, though still more concentrated at the tip. At very negative potentials ($E < -1.6$ V), the number of well-ordered triangular pits decreases, indicating a transition toward more disordered, highly roughened structures.

Across both NaOH and KOH electrolytes, two consistent trends emerge. First, the spatial distribution of corrosion features reflects geometric electric-field effects: regions of higher curvature, such as the wire tip, experience intensified local fields that enhance hydrogen evolution, cation accumulation, and atom detachment. Second, increasing the applied negative potential systematically intensifies corrosion, increases surface roughness and EASA, and drives a transition from pit formation to nanoparticle nucleation and eventually to more disordered nanostructures. These observations are consistent with the expectation that more negative potentials increase adsorbed hydrogen coverage, cation accumulation within the double-layer, and interfacial stress, thereby promoting higher

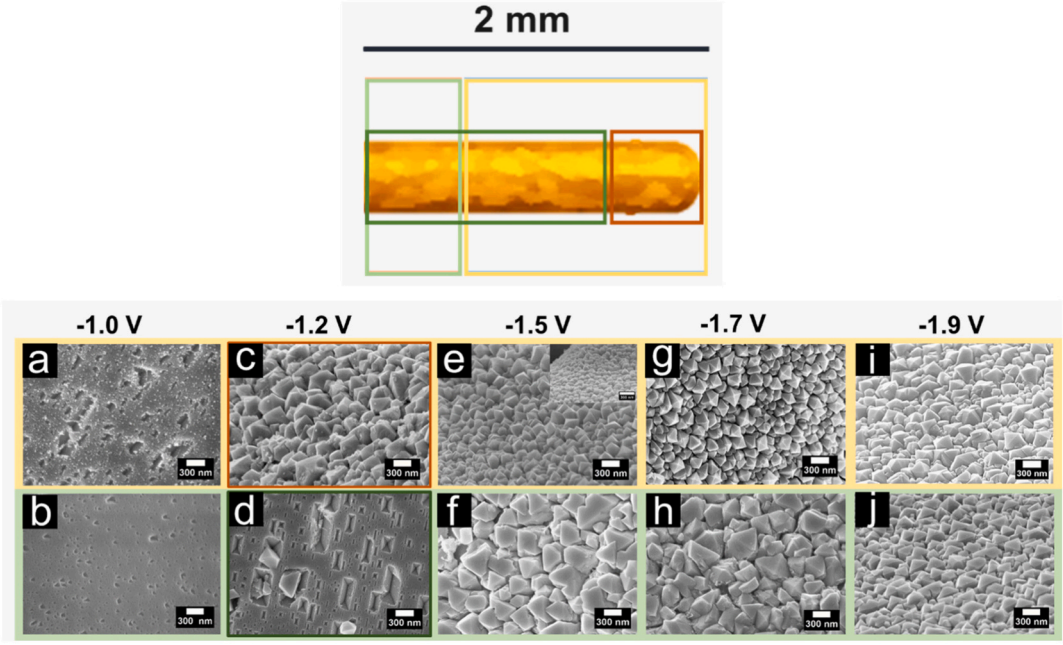

Fig. 29. Cathodic polarization of Au surfaces in 10 M NaOH as a function of applied potential. SEM micrographs of Au electrodes following 60 s of cathodic polarization in 10 M NaOH at −1.0 V (a,b), −1.2 V (c,d), −1.5 V (e,f), −1.7 V (g,h), and −1.9 V (i,j) *vs.* RHE. All scale bars are 300 nm. A schematic depicting the corresponding local structural evolution of the corroded wire is shown above the SEM images.
Reproduced with permission from [32]

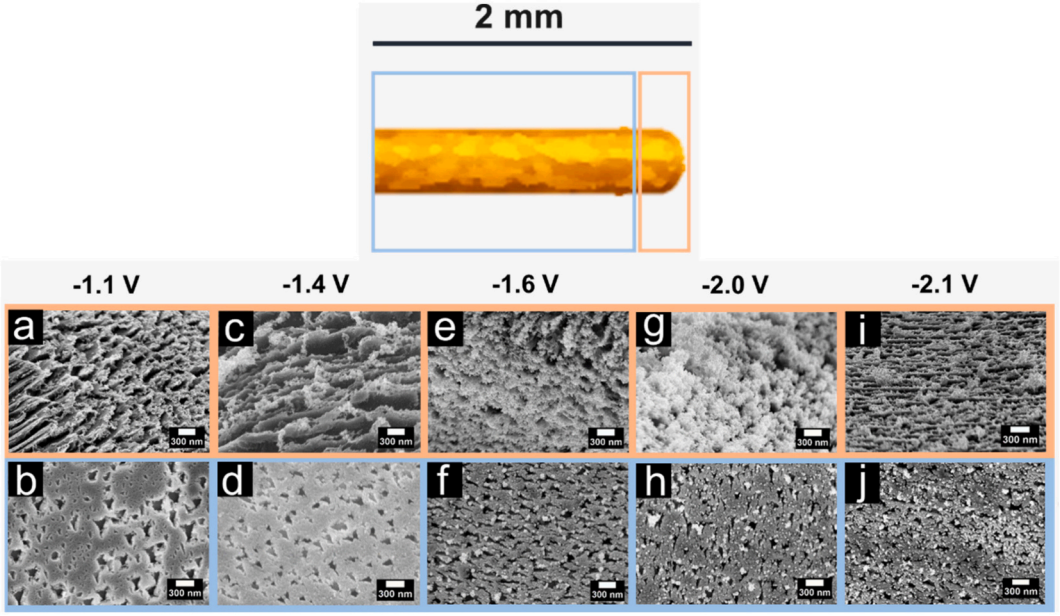

Fig. 30. Cathodic polarization of Au surfaces in 10 M KOH as a function of applied potential. SEM micrographs of Au electrodes after 60 s of cathodic polarization in 10 M KOH at −1.1 V (a,b), −1.4 V (c,d), −1.6 V (e,f), −2.0 V (g,h), and −2.1 V (i,j) *vs.* RHE. Scale bars: 300 nm. The schematic above the images illustrates the associated local structural transformation during corrosion.
Reproduced with permission from [32]

surface atom mobility.

Overall, the electrode potential acts as a master variable that not only determines the onset of cathodic corrosion but also governs its kinetic regime, morphological changes, and spatial distribution. Rather than simply increasing the rate of dissolution, increasingly negative polarization shifts the system from localized etching to dynamic dissolution–redeposition and nanoparticle growth, while extreme conditions promote structural disorder and diffusion-limited restructuring.

4.6.5.3. The nature and concentration of cations. A defining characteristic of cathodic corrosion is that it does not occur in the absence of non-reducible cations in the electrolyte. Experiments performed in acidic media without alkali content, or electrolytes containing only reducible species, consistently show no corrosion, even at highly negative potentials [44]. In contrast, the introduction of non-reducible cations, particularly alkali metal ions, immediately triggers the process. This observation demonstrates that cations are not passive spectators but essential components of the corrosion mechanism. A high local concentration of cations near the electrode surface is particularly important because it provides the countercharge required to stabilize extremely negative potentials, thereby enabling the corrosion process to proceed. In addition, adsorbed cations stabilize charged surface intermediates, modify interfacial water structure, and influence hydrogen adsorption and incorporation into the metal lattice. Consequently, the presence of non-reducible cations is critical for cathodic corrosion, distinguishing it fundamentally from conventional anodic dissolution processes.

Furthermore, the identity and concentration of alkali metal cations exert a decisive influence on cathodic corrosion, strongly affecting the onset potential, rate, facet distribution, EASA, and the resulting surface morphology.

Systematic investigations demonstrate that alkali metal cations exert a profound and highly specific influence on cathodic corrosion, producing markedly different electrochemical signatures and surface morphologies even under otherwise identical conditions [196,197]. To elucidate these effects, Au electrodes were polarized for 60 s at strongly negative potentials in concentrated alkaline electrolytes (5 M and 10 M *A*OH; *A* = Li, Na, K, Cs). The resulting surfaces were subsequently characterized in 0.1 M H_2SO_4 to probe facet distribution and electrochemically active surface area (EASA).

Fig. 31a and 31b present cyclic voltammograms recorded in H_2SO_4 before and after cathodic polarization at −1.6 V *vs.* RHE in 5 M LiOH, NaOH, KOH, and CsOH. Pronounced changes in both the double-layer and surface oxidation regions indicate substantial restructuring of the Au surface. Characteristic voltammetric features associated with anion adsorption, adlayer transitions, and reconstruction lifting reveal the formation of well-ordered (111) facets after polarization in LiOH, NaOH, and KOH, whereas electrodes treated in CsOH exhibit minimal changes, consistent with the persistence of predominantly (100) domains. Analysis of the voltammograms demonstrates a strong dependence of facet distribution (Fig. 31c) and EASA (Fig. 31d) on cation identity and applied potential. Polarization in LiOH, NaOH, and KOH leads to a progressive enrichment of (111) sites with increasing cathodic potential, reaching a maximum near −1.6 V *vs.* RHE, followed by a decline at more negative potentials. The extent of (111) enrichment and EASA enhancement follows the trend LiOH > NaOH > KOH, while CsOH produces little to no measurable restructuring over the same potential range.

Direct morphological evidence for these trends is provided by SEM images (Fig. 31e–h), which reveal cation-dependent corrosion

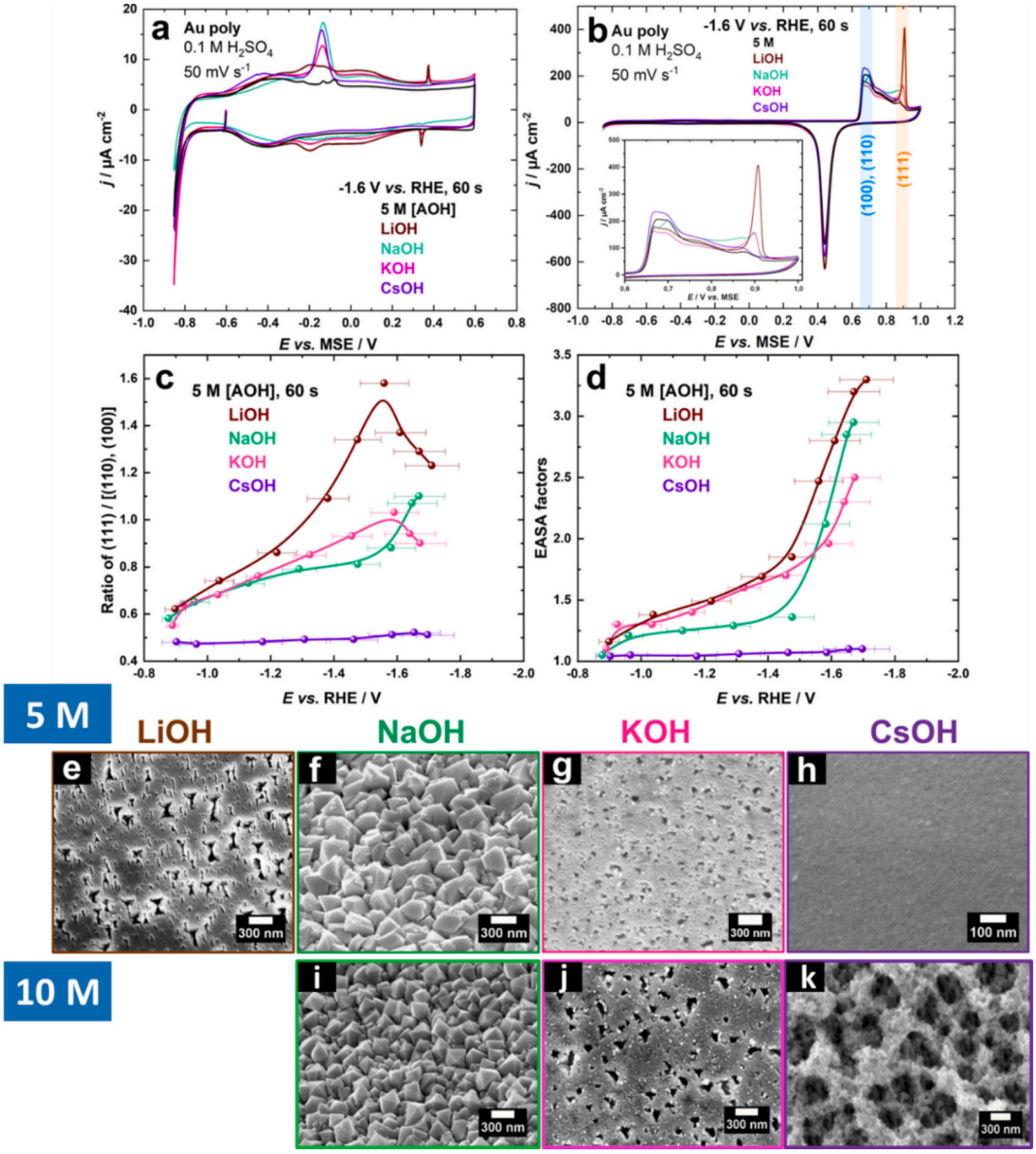

Fig. 31. Effect of alkali metal cations on cathodic corrosion of Au surfaces. Cathodic polarization of Au in concentrated alkali hydroxides. Cyclic voltammograms recorded in 0.1 M H_2SO_4 (50 mV s^{-1}) showing the double-layer region (a) and the oxide formation region (b) before and after polarization in 5 M LiOH, NaOH, KOH, and CsOH at −1.6 V *vs* RHE for 60 s. Panel (c) summarizes the ratio of (111) to [(110),(100)] surface facets, and (d) the corresponding enhancement in electrochemically active surface area (EASA) as a function of applied potential. SEM images after polarization in 5 M LiOH (e), NaOH (f), KOH (g), and CsOH (h), and in 10 M NaOH (i), KOH (j), and CsOH (k), all at −1.6 V *vs*. RHE for 60 s. Reproduced with permission from [32,43]

structures after polarization at −1.6 V *vs.* RHE in 5 M solutions. LiOH produces well-defined triangular etch pits. NaOH leads to the formation of faceted octahedral nanoparticles, suggesting significant dissolution followed by redeposition and crystallite growth. KOH yields irregular pits, whereas CsOH induces only slight surface roughening with minimal nanostructuring. Overall, the severity of cathodic corrosion in 5 M solutions follows the clear trend: LiOH > NaOH > KOH > CsOH, indicating that smaller, strongly hydrated cations promote more pronounced restructuring under these conditions. Cathodic corrosion is also highly sensitive to cation concentration. Increasing cation concentration generally enhances corrosion features, reflecting changes in both ionic strength and interfacial water structure. When NaOH, KOH, and CsOH concentrations are raised to 10 M (LiOH being already near saturation at 5 M), the resulting morphologies differ substantially from those observed at lower concentrations. Higher NaOH concentrations produce more sharply defined octahedral nanoparticles, KOH favors the formation of well-developed triangular pits, and concentrated CsOH, previously relatively inactive, induces the formation of a highly rough nanoporous surface. These observations indicate that increasing

cation concentration enhances atom detachment and redeposition kinetics, even for cations that produce only weak effects at lower concentrations. The observed trends cannot be explained solely by cation size or accumulation at the interface. Hydration energies decrease monotonically with increasing ionic radius, meaning that large, weakly hydrated cations such as Cs^+ can partially shed their solvation shell and approach the electrode surface more closely than small, strongly hydrated cations like Li^+. This proximity should, in principle, increase interfacial charge density and strengthen the electric field, thereby stabilizing negatively charged corrosion intermediates. However, the experimental observation that CsOH produces weaker corrosion than LiOH at 5 M demonstrates that additional factors are operative. In particular, the availability of free (uncoordinated) water molecules appears to play a critical role. Highly concentrated LiOH solutions contain comparatively fewer free water (unbound) molecules than NaOH, KOH, or CsOH at the same concentration, and increasing the concentration of the latter electrolytes to 10 M similarly lowers the amount of free water. Under such conditions, more pronounced corrosion features are observed, suggesting that an optimal balance between free water and ion-bound water is required for cathodic corrosion (Fig. 31 i-k). Taken together, these results demonstrate that cathodic corrosion is governed by a complex interplay between cation identity, concentration, hydration properties, and interfacial water structure.

A complementary example highlighting the decisive role of cations is provided by cathodic corrosion of Pt electrodes [33]. Cathodic polarization at −1.0 V *vs*. RHE in NaOH solutions of increasing concentration (1, 5, and 10 M) reveals a strong correlation between electrolyte concentration and surface restructuring. As shown in Fig. 32a, cyclic voltammograms recorded after corrosion exhibit progressively higher hydrogen adsorption–desorption charges with increasing NaOH concentration, indicating a substantial rise in electrochemically active surface area and thus enhanced roughening. The corrosion onset, marked by attenuation of characteristic (110) features and the emergence of (100) contributions, shifts toward less negative potentials at higher concentrations, demonstrating that concentrated electrolytes facilitate corrosion. Although (100) sites increase monotonically with concentration, the population of (110) sites decreases from 1 to 5 M and rises again at 10 M, suggesting that the surface generated in highly concentrated solutions becomes increasingly disordered.

Microscopic observations corroborate these electrochemical trends (Fig. 32b–g). At 1 M NaOH, the surface shows only mild nanoscale roughening with triangular pits, whereas 5 M NaOH produces extended etch lines and well-defined pits with near-rectangular geometry characteristic of (100)-type orientations. Further increasing the concentration to 10 M leads to larger, less

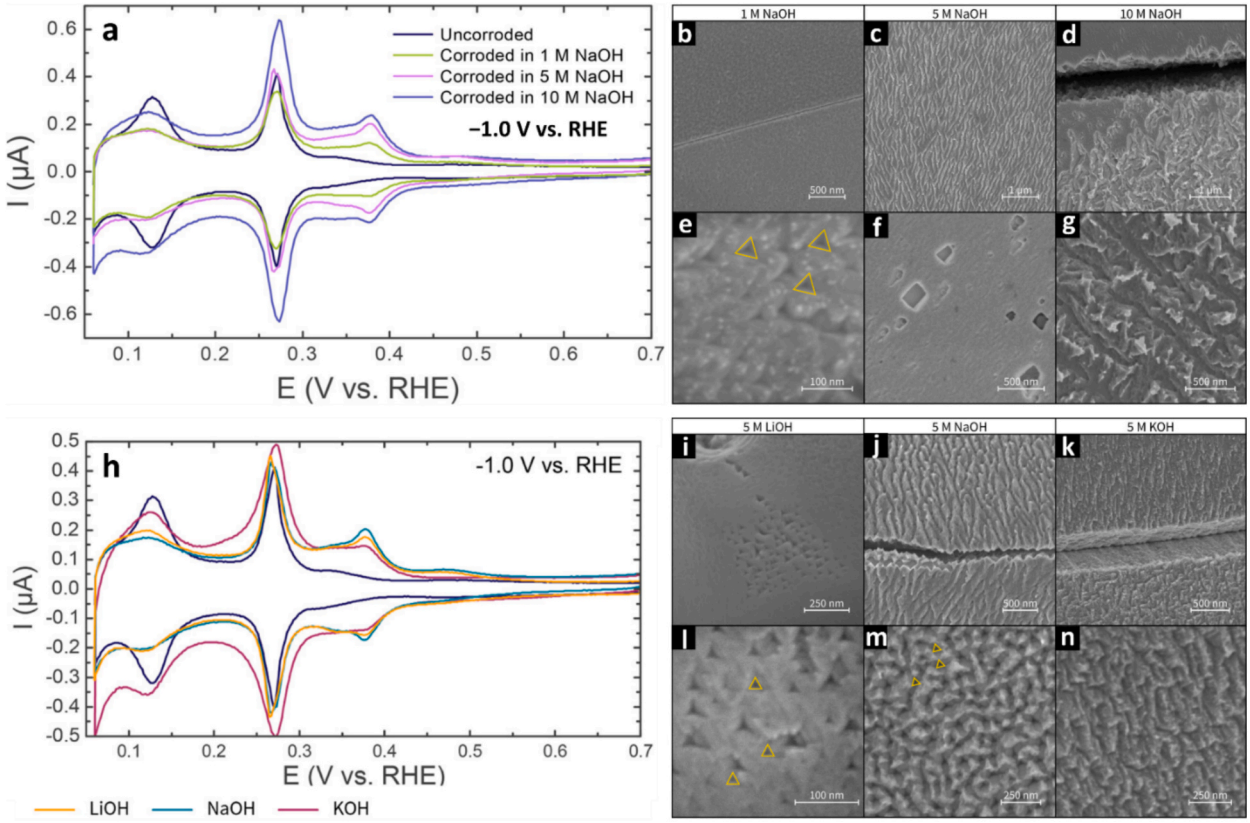

Fig. 32. Cathodic corrosion of Pt as a function of electrolyte concentration and cation identity. (a) Cyclic voltammograms of Pt electrodes polarized at −1.0 V *vs* RHE in NaOH of different concentrations, recorded in 0.5 M H_2SO_4 at 50 mV s^{-1}. SEM images of Pt corroded in 1 M (b,e), 5 M (c,f), and 10 M NaOH (d,g). (h) Voltammograms of Pt corroded in 5 M LiOH, NaOH, and KOH. Corresponding SEM micrographs after polarization in 5 M LiOH (i,l), NaOH (j,m), and KOH (k,n). Characteristic triangular surface features are indicated.
Reproduced with permission from [33]

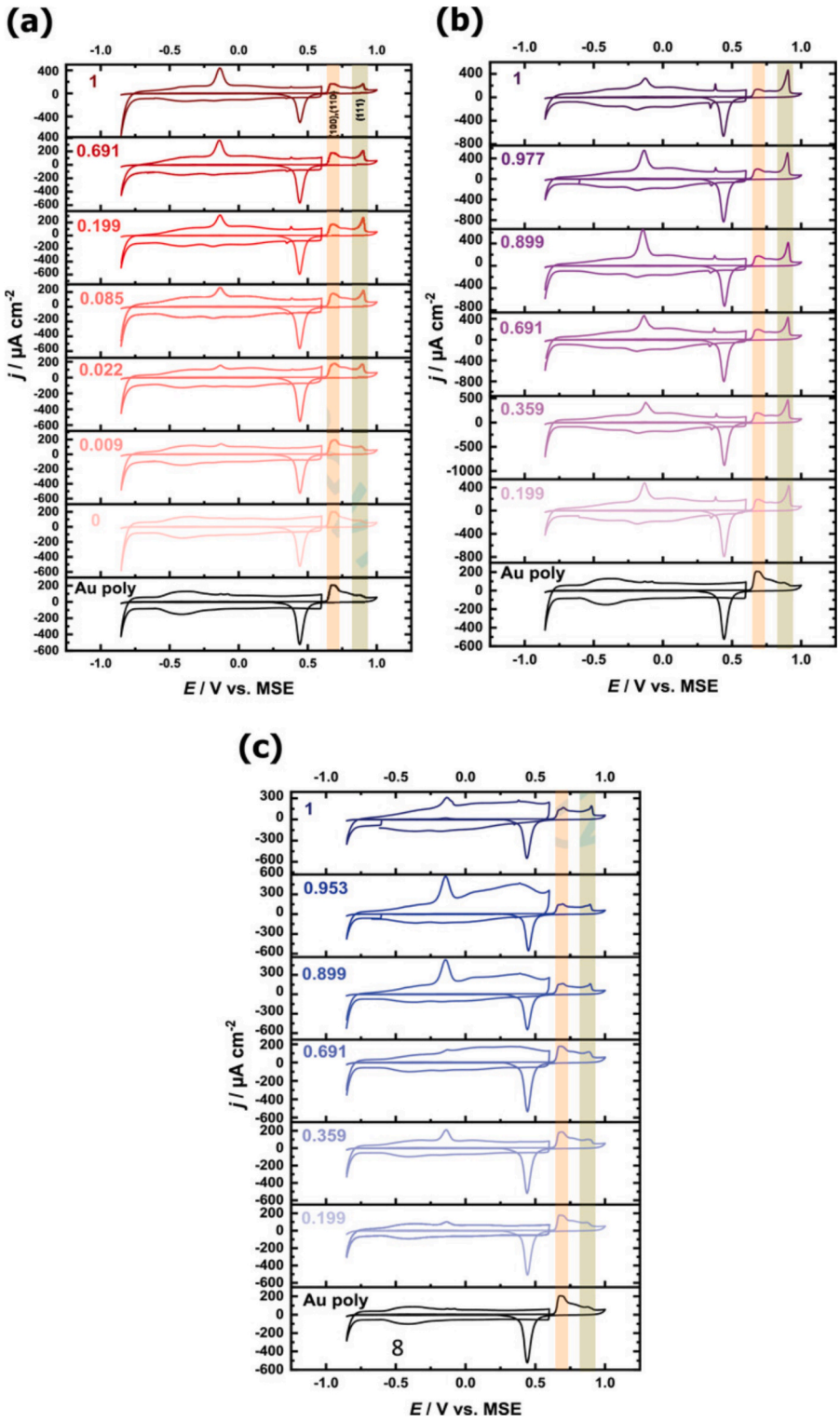

Fig. 33. Electrochemical fingerprints of Au surfaces after cathodic polarization as a function of water content. Cyclic voltammograms of an Au wire in 0.1 M H_2SO_4 at 50 mV s^{-1} before and after polarization at −1.6 V *vs* RHE for 60 s in (a) 5 M KOH, (b) 10 M KOH, and (c) 10 M NaOH, shown as a function of water content in methanol–water mixtures. Currents are normalized to the electrochemically active surface area; the double-layer region is magnified.
Reproduced with permission from [186]

regular features with poorly defined edges, consistent with the formation of highly rough and structurally disordered surfaces. Thus, both electrochemical signatures and SEM imaging confirm that increasing cation concentration intensifies corrosion and drives a transition from localized faceted etching toward more ill-defined dissolution patterns.

Cathodic corrosion is likewise highly sensitive to cation identity [33]. At identical conditions (5 M *A*OH, *A* = Li, Na, K) at −1 V *vs.* RHE, the extent of surface area generation follows the order KOH > NaOH > LiOH, different from the trend observed for Au surfaces. Changes in facet distribution reveal that NaOH produces slightly more (100) terraces than LiOH, whereas KOH favors the formation of step-rich surfaces, including increased (110) and (100) step sites, indicative of higher disorder (Fig. 32h). SEM analysis (Fig. 32i-n) reveals distinct morphologies associated with each cation. Corrosion in LiOH generates relatively triangular pits attributed to (100)-type features, while NaOH produces widespread etch lines, rectangular pits, and corrugated regions containing triangular motifs that likely act as nucleation sites for further etching. In contrast, KOH leads to the most severe restructuring, characterized by deep troughs along grain boundaries and highly rough surfaces lacking well-defined crystallographic features. Together, these observations demonstrate that both cation size and concentration govern not only the rate of cathodic corrosion but also the resulting facet distribution and degree of structural order, reinforcing the central role of alkali metal cations in shaping cathodically corroded metal surfaces.

4.6.5.4. The role of the solvent. The nature of the solvent plays a decisive role in cathodic corrosion, governing both the availability of reactive species and the stability of intermediate products. While cathodic corrosion in aqueous alkaline media is now well established, earlier studies demonstrated that metal dissolution under strongly negative potentials can also occur in non-aqueous environments. In anhydrous aprotic solvents such as DMF or diglyme, several metals (*e.g.*, Pb, Ga, In, Cr, Pt) undergo cathodic etching only in the presence of tetraalkylammonium (R_4N^+) electrolytes [196–199]. Under these conditions, the corrosion products were identified as polynuclear metal anions with empirical compositions of $(R_4N)_n(M_m)$, indicating the formation of electron-rich metal clusters stabilized by bulky organic cations [200,201]. Similarly, in liquid ammonia containing KI, gold can dissolve cathodically via the formation of auride (Au^-) [202,203]. Cathodic corrosion has also been reported in ionic liquids, where negative oxidation states of noble metals and nanostructured products can form [204,205].

Despite these observations, the mechanism operating in aqueous alkaline electrolytes is fundamentally different. In such systems, water is not merely a passive solvent but an active participant that enables hydrogen evolution and dynamic interfacial restructuring. A recent study provides direct experimental evidence that water is essential for triggering cathodic corrosion of Au in alkali metal hydroxide electrolytes. When aqueous KOH or NaOH is progressively replaced by methanol, the corrosion activity decreases dramatically and ultimately disappears under nearly anhydrous conditions, even though the electrolyte still contains high concentrations of cations. This finding demonstrates that the presence of alkali cations alone is not sufficient; instead, the presence of water molecules at the interface is required to sustain the corrosion process.

Fig. 33 illustrates this behavior electrochemically. Cyclic voltammograms obtained after cathodic polarization in aqueous methanolic KOH or NaOH at different concentrations show a systematic decrease in characteristic surface features as the water content decreases (Fig. 33a-c). In water-free electrolytes, the voltammograms resemble those of untreated electrodes, confirming the absence of significant corrosion. In comparison, the voltammetric profiles reveal pronounced changes associated with surface restructuring and increased EASA as the mole fraction of water increases. Morphological evidence from SEM (Fig. 34) corroborates the electrochemical observations. The surface structure of Au electrodes was examined after polarization at −1.6 V *vs.* RHE for 60 s in 10 M NaOH containing systematically varied mole fractions of water (x_{H2O} = 0, 0.009, 0.199, 0.359, 0.691, and 1). The corresponding SEM micrographs (Fig. 34a−x) provide direct evidence for the critical role of water in enabling cathodic corrosion.

In purely methanolic electrolyte (x_{H2O} = 0) and at very low water contents ($x_{H2O} \leq 0.691$), the Au surface exhibits only minor morphological alterations after polarization (Fig. 34a–d). The characteristic octahedral nanocrystals typically observed after cathodic

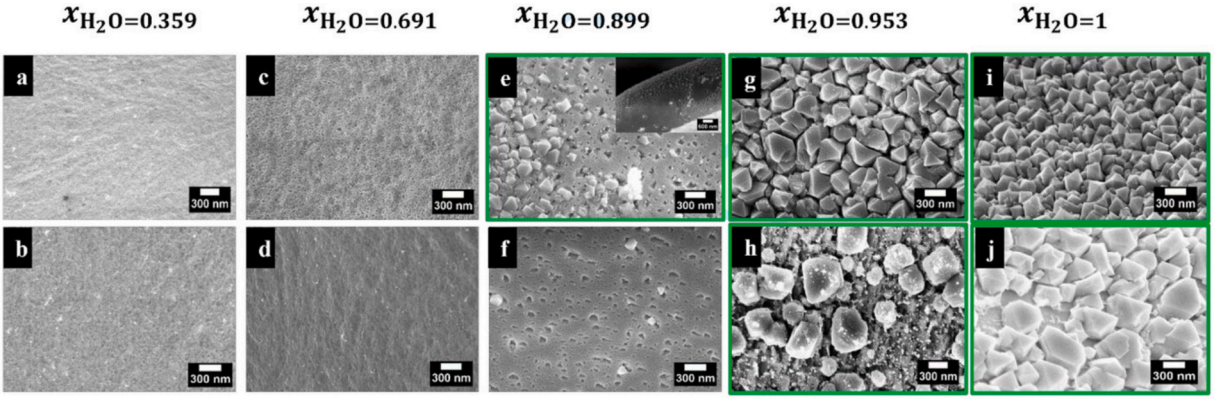

Fig. 34. SEM micrographs of Au electrodes after cathodic corrosion at −1.6 V *vs.* RHE for 60 s in 10 M NaOH containing water at mole fractions of water of (a, b)x_{H_2O} = 0.359, (c, d)x_{H_2O} = 0.691, (e, f)x_{H_2O} = 0.899, (g, h)x_{H_2O} = 0.953, and (i, j)x_{H_2O} = 1.
Reproduced with permission from [186]

corrosion in concentrated aqueous NaOH are essentially absent under these conditions. A clear transition occurs at $x_{H2O} = 0.899$. At this composition, octahedral nanocrystals first emerge at the extreme tip region of the wire (Fig. 34e and inset), while etching pits become visible along the remaining surface (Fig. 34f). Upon further increasing the water fraction to $x_{H2O} \geq 0.953$, the density of octahedral nanocrystals increases markedly (Fig. 34g–j). Well-defined octahedral particles cover a substantial portion of the corroded surface (approximately 60%), whereas the remaining regions display less ordered or partially developed nanostructures. In fully aqueous solution ($x_{H2O} = 1$), the octahedral nanocrystals are most uniformly distributed and exhibit the highest degree of geometric definition, consistent with optimal corrosion conditions. For clarity, the SEM panels in which octahedral nanocrystals are present are highlighted in green in Fig. 33, demonstrating the threshold water content required to trigger the formation of nanoparticles by cathodic corrosion. The progressive emergence and sharpening of octahedral features with increasing water content strongly suggest that water governs key interfacial processes, including hydrogen evolution kinetics and double-layer structuring.

In summary, water at the electrode–electrolyte interface is indispensable for achieving high surface excess charge densities and sustaining vigorous hydrogen evolution, as demonstrated by methanol–water mixtures.

4.6.6. *Applications of cathodic corrosion*

4.6.6.1. Synthesis of nanoparticles and single-atom catalysts. Cathodic corrosion has emerged as a versatile bottom-up electrochemical route for the rapid, solution-phase synthesis of nanostructured materials. Unlike conventional chemical and physical methods, this approach operates under mild conditions using only an external potential, an electrolyte, and a bulk metal precursor. It can produce milligram-scale quantities of nanoparticles within minutes to hours without the need for surfactants, stabilizers, or capping agents that may block active sites or alter intrinsic catalytic properties. Consequently, cathodic corrosion has been successfully employed to generate a wide range of nanomaterials, including pure metallic nanoparticles, metallic alloys, and metal oxides, as well as single-atom catalysts. Because the fundamental aspects, synthetic strategies, and catalytic applications of corrosion-derived nanoparticles and single-atom catalysts have been comprehensively reviewed elsewhere [206], a more concise overview is provided here. For detailed discussions on mechanistic pathways, size and composition control, and advanced applications of colloidal nanoparticles synthesized via cathodic corrosion, readers are referred to that review.

4.6.6.2. Surface restructuring for electrocatalysis. Cathodic corrosion induces profound and controllable modifications of metal electrode surfaces, including changes in crystallographic orientation, substantial increases in EASA, and the formation of steps, kinks, defects, and nanoscale features often accompanied by nanoparticle formation. Such restructuring can be deliberately exploited to tailor the activity and selectivity of electrocatalysts without altering their chemical composition. In addition to enhancing catalytic performance, cathodically corroded electrodes frequently exhibit preferential facet distributions and clean nanostructures, making them valuable as model systems for structure–activity studies and as substrates for spectroelectrochemical techniques such as surface-enhanced Raman spectroscopy (SERS) [31,32,58].

A representative example is the restructuring of Au electrodes by cathodic polarization in concentrated alkaline electrolytes (10 M KOH or NaOH) [32]. A clear signature of corrosion under these conditions is a substantial redistribution of surface facets, with a

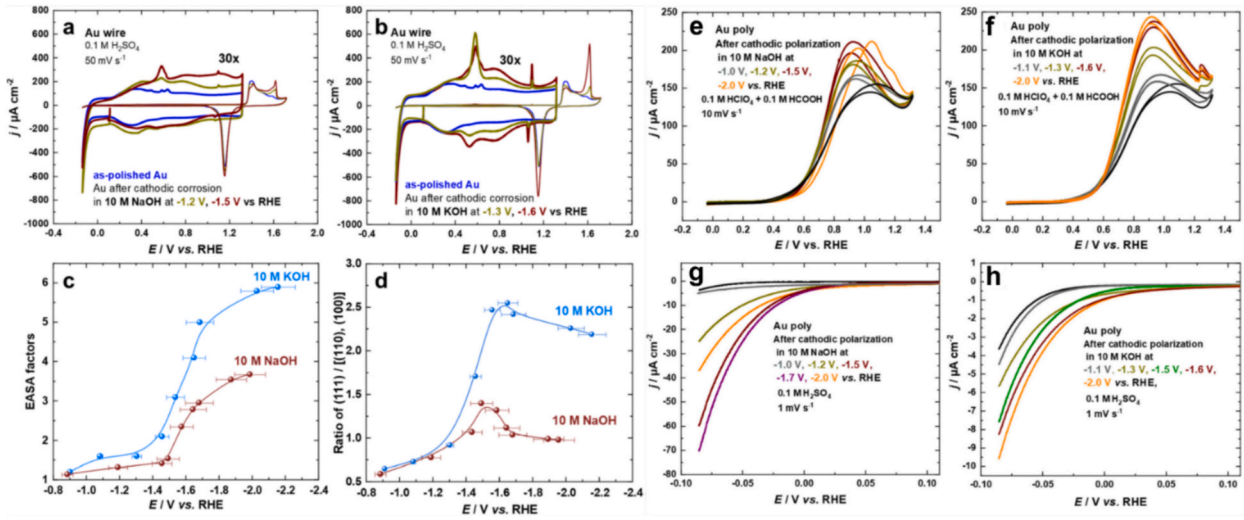

Fig. 35. Potential-dependent restructuring of Au in concentrated alkaline media and the electrocatalytic activity of the resulting Au surfaces. Cyclic voltammograms in 0.1 M H_2SO_4 (50 mV s^{-1}) before and after polarization in 10 M NaOH (a) and 10 M KOH (b) at different potentials for 60 s. (c) Corresponding EASA factors and (d) ratios of (111)/[(110),(100)] facets. Current–potential curves in 0.1 M $HClO_4$ + 0.1 M HCOOH (e,f) and in 0.1 M H_2SO_4 (g,h) illustrating catalytic behavior before and after cathodic polarization.
Reproduced with permission from [32]

pronounced enrichment of (111) domains, particularly after polarization in 10 M KOH. Under optimized potentials, the resulting surfaces exhibit electrochemical characteristics closely resembling those of Au(111) single crystals while retaining a nanostructured morphology. Cyclic voltammetry in 0.1 M H_2SO_4 provides a highly sensitive probe of the surface atomic arrangement. After cathodic polarization, the voltammograms display several fingerprint features associated with Au(111). In the double-layer region, an enhanced anodic peak near 0.60 V *vs.* RHE appears, attributed to lifting of surface reconstruction by specifically adsorbed sulfate. More distinctly, sharp anodic and cathodic spikes at approximately 1.10 and 1.06 V *vs.* RHE emerge, corresponding to a two-dimensional phase transition within the sulfate adlayer on Au(111) terraces. These spikes are significantly sharper and carry higher charge densities for electrodes polarized in KOH compared with NaOH, indicating the formation of larger (111) terraces (Fig. 35a and 35b).

Additional structural information is obtained from the oxide formation region. Anodic peaks at approximately 1.61, 1.41, and 1.38 V *vs.* RHE correspond to oxidation of (111), (110), and (100) surface domains, respectively. The relative charge associated with these peaks directly reflects the facet distribution. Cathodic polarization leads to a pronounced increase in the (111) oxidation peak, particularly for KOH-treated electrodes, confirming the preferential formation of (111) facets. Quantitative analysis shows that both EASA and the fraction of (111) sites increase with more negative polarization potentials, although the enrichment of (111) terraces reaches a maximum within a specific potential window before declining at excessively negative potentials (Fig. 35c and 35d). Notably, polarization in 10 M KOH produces substantially higher EASA and a larger (111)/(100 + 110) ratio than 10 M NaOH. Fascinatingly, the electrocatalytic behavior of cathodically-corroded Au electrodes towards FAOR and HER was investigated (Fig. 35e-h). For the formic acid oxidation reaction (FAOR) in acidic media, electrodes with high (111) contributions display the characteristic bell-shaped current–potential profile known for the Au(111). The specific activity increases with the fraction of (111) terraces, and additional features such as a current "kink" associated with phase transitions of strongly adsorbed formate appear only when large, well-ordered terraces are present. These observations indicate that FAOR proceeds most efficiently on extended (111) domains. In contrast, the hydrogen evolution reaction (HER) is primarily governed by low-coordination sites introduced during nanostructuring. Cathodically corroded Au electrodes exhibit significantly enhanced HER activity compared with polished Au, with lower onset overpotentials approaching those of highly active noble metals. The activity increases as the density of edges, corners, steps, and defects rises, reaching a maximum at intermediate polarization potentials where nanocrystal density is highest. Thus, while FAOR is driven by

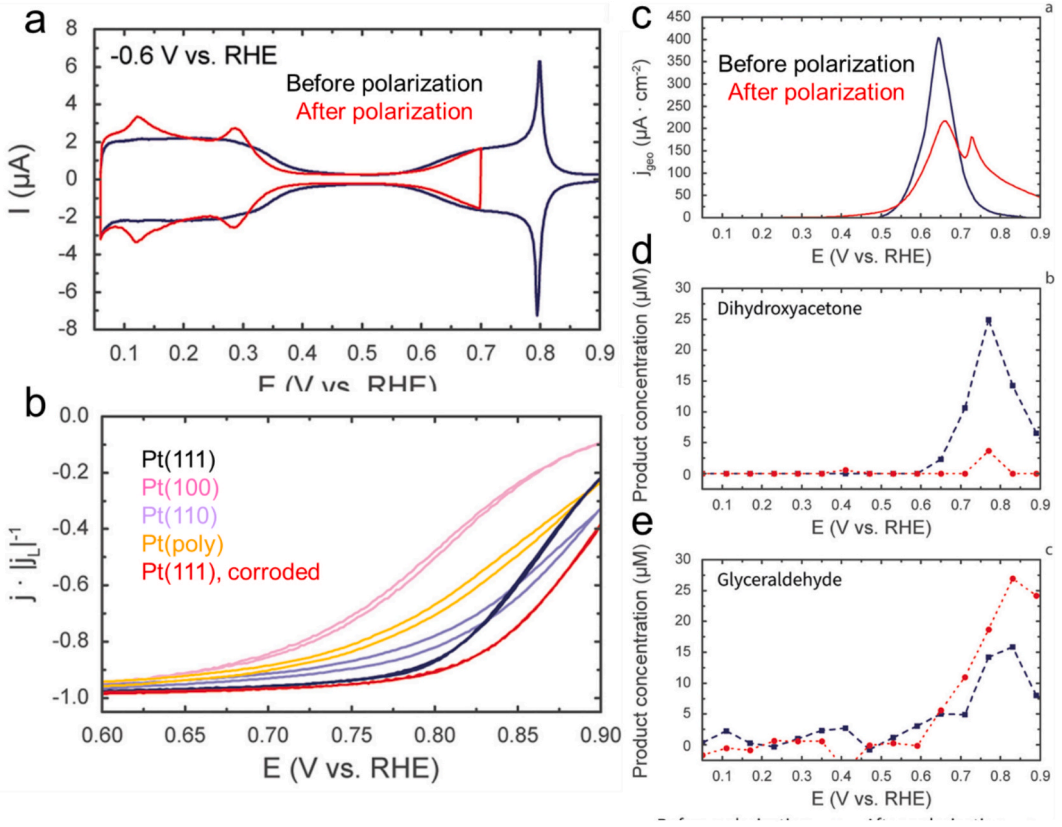

Fig. 36. Modification of Pt(111) electrocatalysis by cathodic corrosion. (a) Cyclic voltammograms of Pt(111) before and after polarization in 1 M NaOH at −0.6 V *vs* RHE (recorded in 0.1 M $HClO_4$, 50 mV s^{-1}). (b) Oxygen reduction polarization curves for Pt single crystals and corroded Pt(111) (1600 rpm, O_2-saturated electrolyte). (c) Glycerol oxidation voltammograms of Pt(111) before and after corrosion in 10 M NaOH at −3 V *vs.* RHE. (d,e) Corresponding concentrations of dihydroxyacetone and glyceraldehyde determined by online HPLC.
Reproduced with permission from [31]

terrace sites, HER is highly sensitive to the low-coordination sites, illustrating the structure sensitivity of both reactions. Cathodically restructured Au electrodes therefore provide a unique platform containing both extended terraces and abundant low-coordination sites. This combination enables systematic identification of active sites and bridges the gap between ideal single-crystal surfaces and practical nanostructured catalysts.

Beyond electrocatalysis, cathodic corrosion offers a simple and reproducible route to fabricate surface-enhanced Raman spectroscopy (SERS)-active Au substrates [58]. Nanostructured electrodes enriched in (111) domains, which are produced by cathodic polarization in 10 M KOH at −1.6 V *vs.* RHE, exhibit strong Raman enhancement for adsorbed probe molecules such as pyridine, whereas untreated Au surfaces show negligible signal under identical conditions. Importantly, these substrates provide a homogeneous response across the entire modified area and retain the electrochemical behavior of clean Au surfaces. Consequently, cathodically corroded Au electrodes serve as cost-effective, contamination-free SERS platforms suitable for *in-situ* spectroelectrochemical investigations.

Cathodic corrosion can also be employed to modify well-defined platinum single-crystal surfaces, providing a powerful route to tune catalytic activity and selectivity without introducing foreign elements [31]. A representative case is the restructuring of Pt(111) electrodes by cathodic polarization in alkaline media. The pristine Pt(111) surface exhibits the characteristic voltammetric response of an atomically flat terrace: hydrogen adsorption/desorption features between ~0.06 and 0.40 V *vs.* RHE, followed by the double-layer region and subsequent OH adsorption between ~0.5 and 0.9 V *vs.* RHE, with no signatures of step sites. After polarization at −0.6 V *vs.* RHE in 1 M NaOH, the voltammetric profile changes markedly. New peaks emerge at ~0.13 V and ~0.29 V *vs.* RHE, corresponding to the formation of (110)-type and (100)-type step sites, respectively (Fig. 36a). These features indicate controlled nanoscale roughening of the surface, accompanied by a moderate (~12%) increase in hydrogen desorption charge, reflecting an increase in EASA. In parallel, the onset of OH adsorption shifts slightly toward more positive potentials, suggesting weakened OH binding on the remaining (111) terraces. Such a modification of adsorption energetics is expected to influence reactions limited by oxygenated species adsorption, most notably the oxygen reduction reaction (ORR).

Furthermore, electrochemical measurements demonstrate that cathodically corroded Pt(111) exhibits enhanced ORR activity compared with pristine Pt(111), polycrystalline Pt, and even the low-index basal planes of platinum. At 0.9 V *vs.* RHE, the activity of the modified surface exceeds that of Pt(100), Pt(110), and Pt(111) due to the combination of terraces and newly generated low-coordination sites (Fig. 36b). Thus, controlled cathodic corrosion enables activity enhancement while preserving the intrinsic chemical identity of the surface.

When Pt(111) is subjected to strong cathodic corrosion in 10 M NaOH at −3 V *vs.* RHE, the voltammetric response reveals a substantial increase in surface area, approximately threefold based on the double-layer current. The newly generated surface is dominated by (100)-type sites: a sharp peak at ~0.29 V *vs.* RHE indicates abundant (100) steps, while a broad feature at higher potentials reflects the formation of extended (100) terraces, with a smaller contribution from (110) steps.

This structural transformation has a profound effect on glycerol oxidation, a reaction known for its complex product distribution. On pristine Pt(111), oxidation proceeds with a peak at ~0.60–0.65 V *vs.* RHE and produces both dihydroxyacetone and

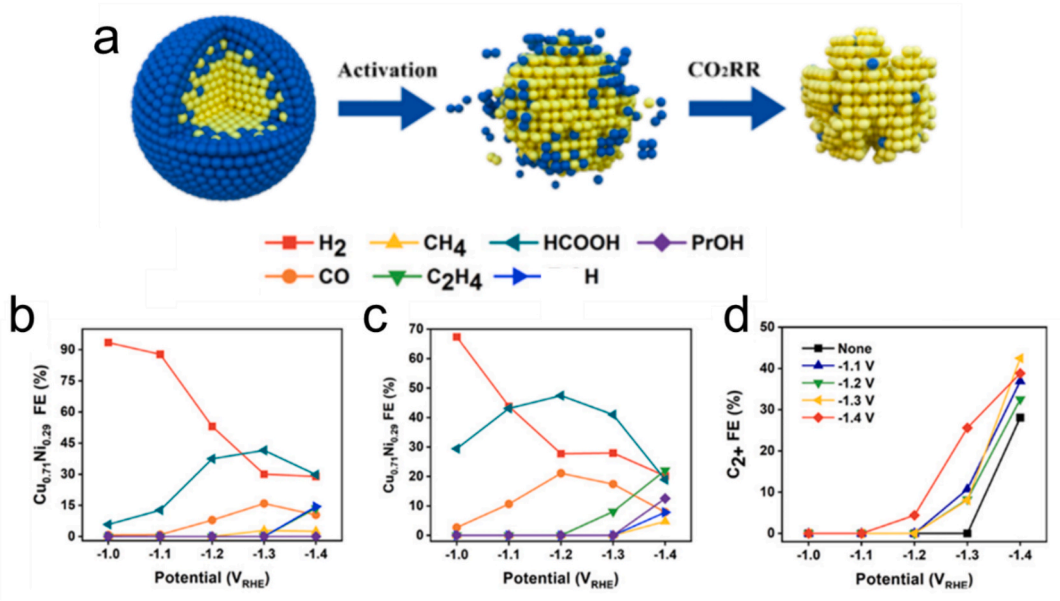

Fig. 37. Cathodic corrosion-driven evolution of Cu_xNi_{1-x} nanoparticles during CO_2 reduction. (a) Schematic illustrating structural transformation under cathodic conditions. Faradaic efficiencies for CO_2 reduction on $Cu_{0.71}Ni_{0.29}$ nanoparticles (b) before activation and (c) after activation at −1.3 V *vs.* RHE for 2 h. (d) Dependence of C_{2+} product selectivity on activation potential.
Reproduced with permission from [207].

glyceraldehyde. In contrast, the cathodically corroded surface shows a shifted peak at more positive potentials (~0.70–0.75 V *vs.* RHE), consistent with the behavior of Pt(100) surfaces (Fig. 36c). Product analysis by high-performance liquid chromatography (HPLC) reveals suppressed formation of dihydroxyacetone and enhanced production of glyceraldehyde, demonstrating that cathodic corrosion redirects the reaction pathway toward a Pt(100)-like selectivity (Fig. 36d and 36e). Importantly, this shift arises primarily from the generation of (100) terraces rather than from step sites alone.

Overall, these results demonstrate that cathodic corrosion provides a versatile tool for transforming an atomically flat Pt(111) surface into a nanostructured catalyst with tunable ensembles of terraces and low-coordination sites. Moderate restructuring enhances activity (*e.g.,* for ORR), whereas extensive restructuring can redirect product selectivity (*e.g.*, for glycerol oxidation).

Another example of cathodic corrosion as an *operando* restructuring strategy is provided by bimetallic Cu–Ni nanoparticles for electrochemical CO_2 reduction [207]. Copper is capable of forming multi-carbon (C_{2+}) products, yet its selectivity is often limited by

Table 1
Qualitative comparison of electrochemical restructuring strategies for metal electrodes.

Method	Key Strengths	Main Limitations	Typical Surface Features	Best Use Cases
Electrodeposition (UPD/OPD)	Scalable, precise control over thickness/composition, industrial compatibility	Metastable structures, sensitive to local pH and mass transport	Thin films, dendrites, alloys, hierarchical structures	Tailored thin films, device-integrated electrodes, compositional tuning
Oxidation–Reduction Cycles (ORCs)	Generates defect-rich surfaces, activates catalysts dynamically	Limited structural control, reproducibility challenges	Roughened surfaces, defects, grain boundaries, nanoparticles	Catalyst activation, defect engineering
Anodic Polarization (moderate)	Forms oxide-derived structures, enhances roughness and activity	Possible material loss, instability under long-term operation	Oxide layers, porous/rough metallic surfaces after reduction	Oxide-derived catalysts, defect-mediated reactions
High-voltage anodization	Produces highly ordered nanostructures (e.g., nanotubes, porous films)	Requires specific electrolytes (e.g., fluoride), limited material scope	Nanotubes, nanopores, self-organized oxide layers	High-surface-area architectures, photo/electrocatalysis
Extreme anodic polarization (plasma-assisted)	Rapid restructuring, unique morphologies, high defect density	high energy consumption, specialized power requirements, Competing Reactions, scalability challenges	High roughness, nanoparticles, amorphous or partially oxidized surfaces	Rapid activation, exploratory surface engineering
Square-wave potential (SWP)	Drives non-equilibrium states, enables dynamic restructuring	Limited reproducibility, complex parameter space	Metastable, defect-rich, nanostructured surfaces	Dynamic catalyst activation, metastable phase generation
Electrochemical dealloying	High surface area, nanoporous structures, tunable composition	Structural coarsening, stability issues over time	Nanoporous metals, bicontinuous structures	High-current–density applications, mass transport-limited reactions
Cathodic corrosion	Facet-selective etching, clean surfaces, nanoparticle formation without surfactants	Harsh conditions, limited mechanistic understanding	Faceted nanoparticles, pits, high-index surfaces	Structure-sensitive reactions, nanoparticle synthesis, single-atom catalysts
Method	Key Strengths	Main Limitations	Typical Surface Features	Best Use Cases
Electrodeposition (UPD/OPD)	Scalable, precise control over thickness/composition, industrial compatibility	Metastable structures, sensitive to local pH and mass transport	Thin films, dendrites, alloys, hierarchical structures	Tailored thin films, device-integrated electrodes, compositional tuning
Oxidation–Reduction Cycles (ORCs)	Generates defect-rich surfaces, activates catalysts dynamically	Limited structural control, reproducibility challenges	Roughened surfaces, defects, grain boundaries	Catalyst activation, defect engineering
Anodic Polarization (moderate)	Forms oxide-derived structures, enhances roughness and activity	Possible material loss, instability under long-term operation	Oxide layers, porous/rough metallic surfaces after reduction	Oxide-derived catalysts, defect-mediated reactions
High-voltage anodization	Produces highly ordered nanostructures (e.g., nanotubes, porous films)	Requires specific electrolytes (e.g., fluoride), limited material scope	Nanotubes, nanopores, self-organized oxide layers	High-surface-area architectures, photo/electrocatalysis
Extreme anodic polarization (plasma-assisted)	Rapid restructuring, unique morphologies, high defect density	Poor control, harsh conditions, scalability concerns	Highly roughened, amorphous or partially oxidized surfaces	Rapid activation, exploratory surface engineering
Square-wave potential (SWP/RSWPS)	Drives non-equilibrium states, enables dynamic restructuring	Limited reproducibility, complex parameter space	Metastable, defect-rich, nanostructured surfaces	Dynamic catalyst activation, metastable phase generation
Electrochemical dealloying	High surface area, nanoporous structures, tunable composition	Structural coarsening, stability issues over time	Nanoporous metals, bicontinuous structures	High-current–density applications, mass transport-limited reactions
Cathodic corrosion	Facet-selective etching, clean surfaces, nanoparticle formation without surfactants	Harsh conditions, limited mechanistic understanding	Faceted nanoparticles, pits, roughness, high-index surfaces	Structure-sensitive reactions, Tailoring the electrode activity, nanoparticle synthesis, single-atom catalysts

competing HER. Incorporation of a second metal can tune adsorption energetics and reaction pathways. In Cu–Ni systems, the higher oxophilicity of Ni leads to surface segregation and oxidation in air, producing Ni-enriched shells that strongly favor HER and suppress CO_2 reduction. Thus, the as-prepared catalyst structure does not necessarily represent the true active state. Cathodic activation at sufficiently negative potentials induces selective corrosion of Ni, fundamentally transforming the electrocatalyst. Initially, Cu_xNi_{1-x} nanoparticles exhibit spherical morphology with homogeneous alloy structures, but surface-sensitive analyses reveal Ni enrichment at the outer layer. Before activation, this Ni-rich surface leads to extremely high HER selectivity (often > 90% Faradaic efficiency for H_2 at −1.0 V *vs.* RHE), reflecting the intrinsic hydrogen evolution activity of Ni. Upon cathodic polarization in a CO_2-saturated electrolyte, cathodic corrosion preferentially dissolves Ni from the surface (Fig. 37a). Because Ni is thermodynamically less stable than Cu under these conditions, it leaches into the electrolyte without significant redeposition, whereas Cu remains and is progressively reduced to the metallic state.

This corrosion-driven dealloying produces irregular, defect-rich Cu nanoparticles with roughened surfaces and increased densities of low-coordination sites. Microscopic observations show a transition from smooth spheres to highly distorted particles, while compositional analyses indicate dramatic Ni loss, up to nearly complete removal after extended activation. Concomitantly, the oxidation state of Cu shifts toward metallic Cu^0, accompanied by an increase in Cu–Cu coordination and a decrease in Cu–O contributions, confirming reduction and restructuring of the catalyst surface.

These structural changes translate directly into electrocatalytic performance. After activation, HER is strongly suppressed and CO_2 reduction is enhanced across all compositions. Prior to activation, the $Cu_{0.71}Ni_{0.29}$ catalyst exhibits a strong preference for the hydrogen evolution reaction (HER), delivering a Faradaic efficiency (FE) for H_2 exceeding 90% at −1.0 V *vs.* RHE, while CO_2 reduction products are formed only in minor amounts (Fig. 37b). This behavior is consistent with a Ni-enriched surface, which favors HER over CO_2RR. Cathodic activation at increasingly negative potentials (−1.2 to −1.4 V *vs.* RHE) markedly alters the catalytic response. For example, after activation at −1.3 V *vs.* RHE, the H_2 FE decreases to 67.4% at −1.0 V *vs.* RHE, accompanied by a pronounced shift in product distribution toward CO_2RR. The formate FE increases from 5.8% to 29.4% at −1.0 V *vs.* RHE, while the CO FE rises from 7.9% to 21.1% at −1.2 V *vs.* RHE (Fig. 37c). Most notably, the selectivity toward multicarbon (C_{2+}) products is strongly enhanced: a maximum C_{2+} FE of 42.5% is achieved at −1.4 V *vs.* RHE following activation at −1.3 V *vs.* RHE, identifying this treatment as optimal. In addition, 1-propanol emerges as a new liquid product with an FE of 12.6% under these conditions (Fig. 36d). Overall, cathodic activation induces a substantial suppression of HER and a concurrent promotion of CO_2 reduction, particularly toward C_{2+} products, a trend that is similarly observed across other Cu_xNi_{1-x} compositions.

The appearance of multi-carbon products such as ethylene, ethanol, and even propanol indicates that the reconstructed Cu surface promotes C–C coupling. The improvement correlates with both increased defect density and exposure of metallic Cu sites following Ni removal.

Importantly, this study demonstrates that cathodic corrosion can be leveraged not merely as a degradation phenomenon but as an activation protocol to transform bimetallic nanoparticles into highly selective CO_2RR catalysts. By tuning composition and activation potential, the balance between HER and CO_2 reduction can be systematically controlled. More broadly, these findings highlight that the true active phase of many electrocatalysts may emerge only under strongly reducing conditions, where dissolution, redeposition, and surface reconstruction occur simultaneously.

To provide a practical framework for selecting appropriate electrochemical restructuring strategies, the key methods discussed above are qualitatively compared in terms of their strengths, limitations, and the resulting surface architectures (Table 1).

5. Support and substrate effects in electrochemically restructured systems

Electrochemical restructuring processes are inherently interfacial phenomena that occur at the boundary between the active metal phase and its underlying support or substrate. While this review emphasizes the development of binder-free electrodes, the term “free-standing” must be interpreted with care. In most practical systems, the evolving catalytic phase remains electronically and structurally coupled to a conductive substrate, which plays an active and often decisive role in governing restructuring pathways and catalytic performance.

A large body of literature in electrocatalysis and heterogeneous catalysis has established that catalyst supports are not inert components, but can strongly influence activity, selectivity, and stability through particle–support interactions. These effects arise from several interrelated factors, including electronic coupling, interfacial strain, charge transfer, and the stabilization of specific surface structures. In electrochemical environments, these interactions are further complicated by potential-dependent phenomena, such as double-layer structure, ion adsorption, and dynamic surface oxidation–reduction processes [208,209].

In the context of electrochemical restructuring Methods, the substrate can directly influence nucleation and growth processes during electrodeposition or square-wave potentials [210]. For instance, lattice mismatch and epitaxial relationships between the substrate and deposited metal can dictate crystallographic orientation and facet distribution [211]. Similarly, the local electric field distribution, which is strongly affected by electrode geometry, can lead to spatially heterogeneous restructuring, as frequently observed during cathodic corrosion at sharp tips or defect sites [32].

Beyond structural effects, the substrate also plays a critical role in charge transport and catalytic functionality. The electrical conductivity and interfacial contact between the active phase and the support determine the efficiency of electron transfer, particularly under high current densities. In some cases, catalytic activity is not solely associated with the deposited metal, but emerges from synergistic interactions at the metal–support interface. These include modification of the electronic structure of active sites, stabilization of reaction intermediates, and participation of the support in adsorption or reaction pathways. In some systems, the active phase must remain electrically connected to the support to sustain catalytic activity, and disconnection leads to deactivation, highlighting the

functional interdependence of catalyst and substrate [212]. Importantly, the substrate itself may undergo dynamic changes under electrochemical conditions. Even materials commonly considered stable, such as glassy carbon, can experience surface oxidation, reconstruction, or functionalization under anodic or cathodic polarization [213,214]. These transformations can alter surface wettability, local pH, and interfacial bonding, thereby indirectly influencing restructuring processes and catalytic behavior.

These considerations highlight that the concept of "free-standing" electrodes should not be interpreted as the absence of a supporting structure, but rather as the elimination of polymeric binders and insulating additives. A more accurate description is that electrochemical restructuring enables the formation of binder-free and substrate-integrated catalytic architectures, in which the active material is directly grown from or transformed out of the electrode itself.

Recognizing the active role of supports also opens new design opportunities. Rather than minimizing substrate effects, future strategies may deliberately exploit support–catalyst interactions to guide restructuring pathways, stabilize desired surface configurations, and enhance long-term performance. This perspective aligns with the broader understanding that catalytic functionality in electrochemical systems emerges from the coupled evolution of both the active phase and its supporting interface.

6. Perspectives and design guidelines for electrochemical restructuring of metal surfaces

The analysis presented in this review underscores that electrochemical restructuring methods go beyond simple preparation strategies, serving as a versatile materials-design toolbox for engineering catalytic interfaces. A key insight emerging from the structure-oriented classification is that no single restructuring strategy is universally optimal; rather, each method provides access to a distinct class of surface architectures with specific catalytic functionalities. This perspective shifts the focus from method comparison toward rational selection and integration of restructuring pathways.

A central design principle is that the targeted catalytic function should dictate the restructuring strategy. For reactions governed by structure-sensitive pathways, such as those where selectivity is strongly dependent on surface atomic arrangement, approaches capable of generating well-defined facets, most notably cathodic corrosion, are particularly advantageous. In contrast, applications requiring high current densities and robust performance benefit from nanoporous architectures generated by dealloying, which provide a balance between surface area and structural stability.

Electrodeposition provides a versatile and scalable route for controlled growth of metallic structures. By tuning deposition parameters such as potential, current density, and electrolyte composition, it is possible to precisely control film thickness, morphology, and composition. This makes electrodeposition particularly attractive for the fabrication of tailored thin films and hierarchical electrode architectures under industrially relevant conditions. However, it is important to recognize that electrodeposited structures are often not static; they may undergo further restructuring during operation, which can either enhance or compromise catalytic performance depending on the system.

Dynamic electrochemical methods, including potential cycling and pulsed or square-wave techniques, introduce an additional level of control by driving the system far from equilibrium. These approaches promote the formation of defect-rich and metastable surface states, including vacancies, disordered domains, and transient active sites. Such dynamically generated structures are highly relevant for catalyst activation and can access configurations that are not attainable under steady-state conditions. At the same time, the lack of precise control over the final morphology and the limited reproducibility of these methods remain significantly challenging.

Anodic polarization provides a complementary route toward oxide-derived and roughened metallic surfaces. This process typically generates defect-rich structures with enhanced catalytic activity, particularly in reactions where defects and grain boundaries play a key role. However, they are frequently associated with material loss and structural instability, especially under aggressive electrochemical conditions.

Another important guideline is the need to consider restructuring as a dynamic process rather than a static outcome. Under realistic operating conditions, electrode surfaces continuously evolve, and the initially prepared structure may differ significantly from the active state. Therefore, catalyst design must account for *operando* transformations, including defect formation, surface diffusion, and phase transitions. In this context, strategies that either stabilize desired structures or exploit controlled dynamic evolution represent promising directions.

The role of the electrolyte and interfacial environment also emerges as a critical, yet often underappreciated, parameter. As discussed for cathodic corrosion, electrolyte cations, pH, and applied potentials can fundamentally alter restructuring pathways and the nature of active sites. Future research should therefore place greater emphasis on coupling material design with electrolyte engineering to achieve precise control over surface transformations.

Importantly, the combination of restructuring strategies offers a powerful route toward hierarchical electrode architectures. Sequential approaches, such as dealloying followed by cathodic corrosion, or electrodeposition combined with dynamic activation protocols, enable the integration of complementary structural features within a single system. Such hybrid strategies provide a pathway to decouple surface area, active site distribution, and stability—parameters that are often intrinsically linked in single-method approaches. Despite their potential, these combined methodologies remain largely unexplored and represent a key opportunity for future research.

Looking forward, several challenges must be addressed to fully realize the potential of electrochemical restructuring. These include achieving quantitative control over restructuring processes, improving reproducibility across different systems, and, critically, bridging the gap between laboratory-scale demonstrations and industrial implementation. In particular, systematic studies under technologically relevant conditions, including high current densities (>100 mA cm^{-2}), extended operational lifetimes (>1000 h), and device-level configurations, are still scarce. Addressing these challenges will require advances in *operando* characterization techniques, multiscale modelling, and standardized testing protocols to reliably correlate dynamic surface evolution with catalytic performance.

In summary, the rational design of electrochemically restructured electrodes requires a shift from empirical optimization to mechanism-informed strategy selection. By linking restructuring pathways to specific surface architectures and catalytic functions, and by embracing the dynamic nature of electrochemical interfaces, it becomes possible to develop design rules that guide the next generation of high-performance electrocatalysts.

Based on these aspects, the **key take-home messages** are;

– Electrochemical Methods for restructuring of metal surfaces function as a **design toolbox**, not just a preparation method.
– **Structure dictates function**: method selection must follow the targeted surface architecture.
– The **active catalyst state is dynamic**, not the initially prepared structure.
– **Electrolyte effects are decisive** in directing restructuring pathways and resulting surface structure.
– **Hybrid strategies** might offer a route to decouple activity, stability, and selectivity.
– The **translation** of restructured binder-free electrodes to **industrially relevant conditions** remains a major unresolved challenge.
– Future progress requires integration of **mechanistic understanding, *operando* techniques, and system-level design**.

CRediT authorship contribution statement

Mohamed M. Elnagar: Writing – review & editing, Writing – original draft, Visualization, Validation, Methodology, Investigation, Formal analysis, Data curation, Conceptualization. **Ludwig A. Kibler:** Writing – review & editing, Visualization, Validation, Conceptualization. **Timo Jacob:** Writing – review & editing, Validation, Resources, Project administration, Funding acquisition, Conceptualization.

Declaration of competing interest

The authors declare that they have no known competing financial interests or personal relationships that could have appeared to influence the work reported in this paper.

Acknowledgements

This work was funded by the SFB-CRC1316 (grant no. 327886311) and project 5018053 of the DFG (German Research Foundation). Further, support by the state of Baden-Württemberg and the DFG through grant no INST40/574-1 FUGG is gratefully acknowledged. Finally, support by the BMBF (ministry for science and education) through project OptiABBy (ID: 03XP0531B) is gratefully acknowledged.

Data availability

Data will be made available on request.

References

[1] Ehlers JC, Feidenhans'l AA, Therkildsen KT, Larrazábal GO.. Affordable Green Hydrogen from Alkaline Water Electrolysis: Key Research needs from an Industrial Perspective. ACS Energy Lett 2023;8:1502–9. https://doi.org/10.1021/acsenergylett.2c02897.
[2] Yang Y, Peltier CR, Zeng R, Schimmenti R, Li Q, Huang X, et al. Electrocatalysis in Alkaline Media and Alkaline Membrane-based Energy Technologies. Chem Rev 2022;122:6117–321. https://doi.org/10.1021/acs.chemrev.1c00331.
[3] Hepburn C, Adlen E, Beddington J, Carter EA, Fuss S, Mac Dowell N, et al. The Technological and Economic Prospects for CO_2 Utilization and Removal. Nature 2019;575:87–97. https://doi.org/10.1038/s41586-019-1681-6.
[4] Gao D, Arán-Ais RM, Jeon HS, Roldan CB. Rational Catalyst and Electrolyte Design for CO_2 Electroreduction towards Multicarbon Products. Nat Catal 2019;2:198–210. https://doi.org/10.1038/s41929-019-0235-5.
[5] Foster SL, Bakovic SIP, Duda RD, Maheshwari S, Milton RD, Minteer SD, et al. Catalysts for Nitrogen Reduction to Ammonia. Nat Catal 2018;1:490–500. https://doi.org/10.1038/s41929-018-0092-7.
[6] Ge X, Sumboja A, Wuu D, An T, Li B, Goh FWT, et al. Oxygen Reduction in Alkaline Media: from Mechanisms to Recent Advances of Catalysts. ACS Catal 2015;5:4643–67. https://doi.org/10.1021/acscatal.5b00524.
[7] Möhle S, Zirbes M, Rodrigo E, Gieshoff T, Wiebe A, Waldvogel SR. Modern Electrochemical Aspects for the Synthesis of Value-Added Organic Products. Angew Chem Int Ed 2018;57:6018–41. https://doi.org/10.1002/anie.201712732.
[8] Li P, Zhang T, Mushtaq MA, Wu S, Xiang X, Yan D. Research Progress in Organic Synthesis by Means of Photoelectrocatalysis. Chem Rec 2021;21:841–57. https://doi.org/10.1002/tcr.202000186.
[9] Seh ZW, Kibsgaard J, Dickens CF, Chorkendorff I, Nørskov JK, Jaramillo TF. Combining Theory and Experiment in Electrocatalysis: Insights into Materials Design. Science 1979;2017:355. https://doi.org/10.1126/science.aad4998.
[10] Nørskov JK, Bligaard T, Rossmeisl J, Christensen CH. Towards the Computational Design of Solid Catalysts. Nat Chem 2009;1:37–46. https://doi.org/10.1038/nchem.121.
[11] Yang Y, Luo M, Zhang W, Sun Y, Chen X, Guo S. Metal Surface and Interface Energy Electrocatalysis: Fundamentals, Performance Engineering, and Opportunities. Chem 2018;4:2054–83. https://doi.org/10.1016/j.chempr.2018.05.019.
[12] Bentley CL, Kang M, Unwin PR. Nanoscale Surface Structure–Activity in Electrochemistry and Electrocatalysis. J Am Chem Soc 2019;141:2179–93. https://doi.org/10.1021/jacs.8b09828.
[13] Linnemann J, Kanokkanchana K, Tschulik K. Design strategies for Electrocatalysts from an Electrochemist's Perspective. ACS Catal 2021;11:5318–46. https://doi.org/10.1021/acscatal.0c04118.
[14] Masa J, Andronescu C, Schuhmann W. Electrocatalysis as the Nexus for Sustainable Renewable Energy: the Gordian Knot of activity, Stability, and Selectivity. Angew Chem Int Ed 2020;59:15298–312. https://doi.org/10.1002/anie.202007672.

[15] P. Sabatier, J.-B. Senderens. Hydrogénation directe des oxydes du carbone en présence de divers métaux divisés. C R Acad Sci 1903;134:689–91.
[16] Fechete I. Paul Sabatier – the father of the chemical theory of catalysis. C R Chim 2016;19:1374–81. https://doi.org/10.1016/j.crci.2016.08.006.
[17] Müller K, Fleige M, Rachow F, Schmeißer D. Sabatier based CO_2-methanation of Flue Gas Emitted by conventional Power Plants. Energy Procedia 2013;40:240–8. https://doi.org/10.1016/j.egypro.2013.08.028.
[18] Vogt; C, Weckhuysen BM. The Concept of Active Site in Heterogeneous Catalysis. Nat Rev Chem 2022;6:89–111. https://doi.org/10.1038/s41570-021-00340-y.
[19] Pauling L. The Nature of the Chemical Bond. Press: Cornell Univ; 1939.
[20] Yoshimoto S, Itaya K. Adsorption and Assembly of Ions and Organic Molecules at Electrochemical Interfaces: Nanoscale Aspects. Annu Rev Anal Chem 2013;6:213–35. https://doi.org/10.1146/annurev-anchem-062012-092559.
[21] Rizo R, Roldan CB. Shape-Controlled Nanoparticles as Anodic Catalysts in Low-Temperature Fuel Cells. ACS Energy Lett 2019;4:1484–95. https://doi.org/10.1021/acsenergylett.9b00565.
[22] Busó-Rogero C, Grozovski V, Vidal-Iglesias FJ, Solla-Gullón J, Herrero E, Feliu JM. Surface Structure and Anion Effects in the Oxidation of Ethanol on Platinum Nanoparticles. J Mater Chem A 2013;1:7068. https://doi.org/10.1039/c3ta10996h.
[23] O'Mullane AP. From Single Crystal Surfaces to Single Atoms: investigating Active Sites in Electrocatalysis. Nanoscale 2014;6:4012–26. https://doi.org/10.1039/C4NR00419A.
[24] Safo IA, Dosche C, Özaslan M. Effects of Capping Agents on the Oxygen Reduction Reaction activity and Shape Stability of Pt Nanocubes. ChemPhysChem 2019;20:3010–23. https://doi.org/10.1002/cphc.201900653.
[25] Tran TD, Le HV, Le LT, Nguyen AD, Ung TDT, Tran PD. Restructuring a Gold Nanocatalyst by Electrochemical Treatment to Recover its H_2 Evolution Catalytic Activity. Sustain Energy Fuels 2021;5:1458–65. https://doi.org/10.1039/D1SE00026H.
[26] Alba-Molina D, Puente Santiago AR, Giner-Casares JJ, Martín-Romero MT, Camacho L, Luque R, et al. Citrate-Stabilized Gold Nanoparticles as High-Performance Electrocatalysts: the Role of Size in the Electroreduction of Oxygen. J Phys Chem C 2019;123:9807–12. https://doi.org/10.1021/acs.jpcc.9b00249.
[27] Ma TY, Dai S, Qiao SZ. Self-supported Electrocatalysts for Advanced Energy Conversion Processes. Mater Today 2016;19:265–73. https://doi.org/10.1016/j.mattod.2015.10.012.
[28] Li R, Li Y, Yang P, Wang D, Xu H, Wang B, et al. Electrodeposition: Synthesis of Advanced Transition Metal-based Catalyst for Hydrogen Production via Electrolysis of Water. Journal of Energy Chemistry 2021;57:547–66. https://doi.org/10.1016/j.jechem.2020.08.040.
[29] Huang K, Clausmeyer J, Luo L, Jarvis K, Crooks RM. Shape-controlled Electrodeposition of Single Pt Nanocrystals onto Carbon Nanoelectrodes. Faraday Discuss 2018;210:267–80. https://doi.org/10.1039/C8FD00018B.
[30] Gautam S, Hadley AMK, Gates BD. Controlled growth of platinum Nanoparticles during Electrodeposition using Halide Ion Containing Additives. J Electrochem Soc 2022;169:112508. https://doi.org/10.1149/1945-7111/ac9e22.
[31] Hersbach TJP, Ye C, Garcia AC, Koper MTM. Tailoring the Electrocatalytic activity and Selectivity of Pt(111) through Cathodic Corrosion. ACS Catal 2020;10:15104–13. https://doi.org/10.1021/acscatal.0c04016.
[32] Elnagar MM, Kibler LA, Jacob T. Metal Deposition and Electrocatalysis for Elucidating Structural Changes of Gold Electrodes during Cathodic Corrosion. Green Chem 2023;25:6238–52. https://doi.org/10.1039/D3GC01614E.
[33] Hersbach TJP, McCrum IT, Anastasiadou D, Wever R, Calle-Vallejo F, Koper MTM. Alkali Metal Cation Effects in Structuring Pt, Rh, and Au Surfaces through Cathodic Corrosion. ACS Appl Mater Interfaces 2018;10:39363–79. https://doi.org/10.1021/acsami.8b13883.
[34] Ahrens P, Zander M, Hasse U, Wulff H, Jeyabharathi C, Kruth A, et al. Electrochemical Formation of Gold Nanoparticles on Polycrystalline Gold Electrodes during Prolonged Potential Cycling. ChemElectroChem 2018;5:943–57. https://doi.org/10.1002/celc.201700745.
[35] Zhang H, Chen L, Dong F, Lu Z, Lv E, Dong X, et al. Dynamic Transformation of Active Sites in Energy and Environmental Catalysis. Energy Environ Sci 2024;17:6435–81. https://doi.org/10.1039/D4EE02365J.
[36] Lai W, Ma Z, Zhang J, Yuan Y, Qiao Y, Huang H. Dynamic Evolution of active Sites in Electrocatalytic CO $_2$ Reduction Reaction: Fundamental Understanding and recent Progress. Adv Funct Mater 2022;32:2111193. https://doi.org/10.1002/adfm.202111193.
[37] Chen H, Wang L, Na M, Zou X. Reconstruction chemistry of electrocatalysts under working conditions. Chem Sci 2025;16:20662–76. https://doi.org/10.1039/D5SC06605K.
[38] Chen J, Wang L. Effects of the Catalyst Dynamic Changes and Influence of the Reaction Environment on the Performance of Electrochemical CO_2 Reduction. Adv Mater 2022;34:2103900. https://doi.org/10.1002/adma.202103900.
[39] Zhang H, Zhou Z, Lei Q, Lo TWB. Recent Advances in the *Operando* Structural and Interface Characterisation of Electrocatalysts. Curr Opin Electrochem 2023;38:101215. https://doi.org/10.1016/j.coelec.2023.101215.
[40] Santana Santos C, Jaato BN, Sanjuán I, Schuhmann W, Andronescu C. *Operando* Scanning Electrochemical Probe Microscopy during Electrocatalysis. Chem Rev 2023;123:4972–5019. https://doi.org/10.1021/acs.chemrev.2c00766.
[41] Wirtanen T, Prenzel T, Tessonnier J-P, Waldvogel SR. Cathodic Corrosion of Metal Electrodes—How to prevent it in Electroorganic Synthesis. Chem Rev 2021;121:10241–70. https://doi.org/10.1021/acs.chemrev.1c00148.
[42] Arulmozhi N, Hersbach P, TJ, M Koper MT.. Nanoscale Morphological Evolution of Monocrystalline Pt Surfaces during Cathodic Corrosion. PNAS 2017;117:32267–77. https://doi.org/10.1073/pnas.2017086117/-/DCSupplemental.
[43] Elnagar MM, Kibler LA, Jacob T. Effect of Alkali Metal Cations and Trace Metal Impurities on Cathodic Corrosion of Gold Electrode Surfaces. ChemCatChem 2024;16:e202400526. https://doi.org/10.1002/cctc.202400526.
[44] Yanson AI, Rodriguez P, Garcia-Araez N, Mom RV, Tichelaar FD, Koper MTM. Cathodic corrosion: a Quick, Clean, and Versatile Method for the Synthesis of Metallic Nanoparticles. Angew Chem Int Ed 2011;50:6346–50. https://doi.org/10.1002/anie.201100471.
[45] Yanson AI, Antonov PV, Yanson YI, Koper MTM. Controlling the Size of Platinum Nanoparticles Prepared by Cathodic Corrosion. Electrochim Acta 2013;110:796–800. https://doi.org/10.1016/j.electacta.2013.03.121.
[46] Feng J, Chen D, Sediq AS, Romeijn S, Tichelaar FD, Jiskoot W, et al. Cathodic Corrosion of a Bulk Wire to Nonaggregated Functional Nanocrystals and Nanoalloys. ACS Appl Mater Interfaces 2018;10:9532–40. https://doi.org/10.1021/acsami.7b18105.
[47] Rodriguez P, Tichelaar FD, Koper MTM, Yanson AI. Cathodic Corrosion as a Facile and Effective Method to Prepare Clean Metal Alloy Nanoparticles. J Am Chem Soc 2011;133:17626–9. https://doi.org/10.1021/ja208264e.
[48] Li R, Xu J, Zhao Q, Ren W, Zeng R, Pan Q, et al. Cathodic Corrosion as a Facile and Universal Method for the Preparation of Supported Metal Single Atoms. Nano Res 2021. https://doi.org/10.1007/s12274-021-3767-3.
[49] Perez J, Gonzalez ER, Villullas HM. Hydrogen Evolution Reaction on Gold Single-Crystal Electrodes in Acid Solutions. J Phys Chem B 1998;102:10931–5. https://doi.org/10.1021/jp9831987.
[50] Huang Y, Handoko AD, Hirunsit P, Yeo BS. Electrochemical Reduction of CO_2 using Copper Single-Crystal Surfaces: Effects of CO* Coverage on the Selective Formation of Ethylene. ACS Catal 2017;7:1749–56. https://doi.org/10.1021/acscatal.6b03147.
[51] Sandrini RMLM, Sempionatto JR, Tremiliosi-Filho G, Herrero E, Feliu JM, Souza-Garcia J, et al. Electrocatalytic Oxidation of Glycerol on Platinum Single Crystals in Alkaline Media. ChemElectroChem 2019;6:4238–45. https://doi.org/10.1002/celc.201900311.
[52] Kibler LA, Hermann JM, Matzik FM, Wittmann M, Fackler S, Jacob T. Surface preparation of Well-defined Electrodes: Single Crystal Electrochemistry. Encyclopedia of Solid-Liquid Interfaces, Elsevier 2024:426–49. https://doi.org/10.1016/B978-0-323-85669-0.00112-4.
[53] Climent V, Feliu J. Single Crystal Electrochemistry as an In Situ Analytical Characterization Tool. Annu Rev Anal Chem 2020;13:201–22. https://doi.org/10.1146/annurev-anchem-061318-115541.
[54] Kibler LA, Hermann JM, Abdelrahman A, El-Aziz AA, Jacob T. New Insights on Hydrogen Evolution at Au Single Crystal Electrodes. Curr Opin Electrochem 2018;9:265–70. https://doi.org/10.1016/j.coelec.2018.05.013.

[55] Scholten F, Nguyen KC, Bruce JP, Heyde M, Roldan CB. Identifying Structure–Selectivity Correlations in the Electrochemical Reduction of CO_2 : a Comparison of Well-Ordered Atomically Clean and Chemically Etched Copper Single-Crystal Surface. Angew Chem Int Ed 2021;60:19169–75. https://doi.org/10.1002/anie.202103102.
[56] Kronberg R, Laasonen K. Reconciling the Experimental and Computational Hydrogen Evolution Activities of Pt(111) through DFT-Based Constrained MD Simulations. ACS Catal 2021;11:8062–78. https://doi.org/10.1021/acscatal.1c00538.
[57] Zhao J, Wang M, Peng Y, Ni J, Hu S, Zeng J, et al. Exploring the Strain Effect in Single Particle Electrochemistry using Pd Nanocrystals. Angew Chem Int Ed 2023;62:e202304424. https://doi.org/10.1002/anie.202304424.
[58] Elnagar MM, Hermann JM, Jacob T, Kibler LA. An Affordable Option to Au Single Crystals through Cathodic Corrosion of a Wire: Fabrication, Electrochemical Behavior, and Applications in Electrocatalysis and Spectroscopy. Electrochim Acta 2021;372:137867. https://doi.org/10.1016/j.electacta.2021.137867.
[59] Raaijman SJ, Arulmozhi N, da Silva AHM, Koper MTM. Clean and Reproducible Voltammetry of Copper Single Crystals with Prominent Facet-specific Features using Induction Annealing. J Electrochem Soc 2021;168:096510. https://doi.org/10.1149/1945-7111/ac24b9.
[60] Behjati S, Koper MTM. In Situ STM Study of Roughening of Au(111) Single-Crystal Electrode in Sulfuric Acid Solution during Oxidation–Reduction Cycles. J Phys Chem C 2024;128:19024–1903419024. https://doi.org/10.1021/acs.jpcc.4c06362.
[61] Krupski K, Moors M, Jóźwik P, Kobiela T, Krupski A. Structure Determination of Au on Pt(111) Surface: LEED. STM and DFT Study Materials 2015;8:2935–52. https://doi.org/10.3390/ma8062935.
[62] He Y, Borguet E. Metastable phase of the Au(111) Surface in Electrolyte Revealed by STM and Asymmetric potential Pulse Perturbation. J Phys Chem C 2011;115:5726–31. https://doi.org/10.1021/jp110484w.
[63] Köntje C, Kolb DM, Jerkiewicz G. Roughening and Long-Range Nanopatterning of Au(111) through Potential Cycling in Aqueous Acidic Media. Langmuir 2013;29:10272–8. https://doi.org/10.1021/la4018757.
[64] Kondo T, Morita J, Hanaoka K, Takakusagi S, Tamura K, Takahasi M, et al. Structure of Au(111) and Au(100) Single-Crystal Electrode Surfaces at Various Potentials in Sulfuric Acid solution Determined by In Situ Surface X-ray Scattering. J Phys Chem C 2007;111:13197–204. https://doi.org/10.1021/jp072601j.
[65] Bagger A, Arán-Ais RM, Halldin Stenlid J, Campos dos Santos E, Arnarson L, Degn Jensen K, et al. Ab Initio Cyclic Voltammetry on Cu(111), Cu(100) and Cu (110) in Acidic, Neutral and Alkaline Solutions. ChemPhysChem 2019;20:3096–105. https://doi.org/10.1002/cphc.201900509.
[66] Hamelin A. Cyclic Voltammetry at Gold Single-Crystal Surfaces. Part 1. Behaviour at Low-Index Faces. J Electroanal Chem 1996;407:1–11. https://doi.org/10.1016/0022-0728(95)04499-X.
[67] Feliu JM, Herrero E. Pt Single Crystal Surfaces in Electrochemistry and Electrocatalysis. EES Catal 2024;2:399–410. https://doi.org/10.1039/D3EY00260H.
[68] Monteiro MCO, Jacobse L, Koper MTM. Understanding the Voltammetry of Bulk CO Electrooxidation in Neutral Media through combined SECM Measurements. J Phys Chem Lett 2020;11:9708–13. https://doi.org/10.1021/acs.jpclett.0c02779.
[69] Kibler LA. Hydrogen Electrocatalysis. ChemPhysChem 2006;7:985–91. https://doi.org/10.1002/cphc.200500646.
[70] Rebollar L, Intikhab S, Oliveira NJ, Yan Y, Xu B, McCrum IT, et al. Beyond Adsorption. Descriptors in Hydrogen Electrocatalysis ACS Catal 2020;10:14747–62. https://doi.org/10.1021/acscatal.0c03801.
[71] Rodriguez P, Koper MTM. Electrocatalysis on Gold. PCCP 2014;16:13583–94. https://doi.org/10.1039/C4CP00394B.
[72] Kibler LA, Al-Shakran M. Adsorption of Formate on Au(111) in Acid solution: Relevance for Electro-Oxidation of Formic Acid. J Phys Chem C 2016;120:16238–45. https://doi.org/10.1021/acs.jpcc.6b02044.
[73] Zheng J, Nash J, Xu B, Yan Y. Perspective—Towards Establishing Apparent Hydrogen Binding Energy as the Descriptor for Hydrogen Oxidation/Evolution Reactions. J Electrochem Soc 2018;165:H27. https://doi.org/10.1149/2.0881802jes.
[74] Zheng J, Sheng W, Zhuang Z, Xu B, Yan Y. Universal Dependence of Hydrogen Oxidation and Evolution Reaction Activity of Platinum-Group Metals on pH and Hydrogen Binding Energy. Sci Adv 2016;2. https://doi.org/10.1126/sciadv.1501602.
[75] Chen X, McCrum IT, Schwarz KA, Janik MJ, Koper MTM. Co-adsorption of Cations as the Cause of the Apparent pH Dependence of Hydrogen Adsorption on a Stepped platinum Single-Crystal Electrode. Angew Chem Int Ed 2017;56:15025–9. https://doi.org/10.1002/anie.201709455.
[76] McCrum IT, Chen X, Schwarz KA, Janik MJ, Koper MTM. Effect of Step Density and Orientation on the Apparent pH Dependence of Hydrogen and Hydroxide Adsorption on Stepped Platinum Surfaces. J Phys Chem C 2018;122:16756–64. https://doi.org/10.1021/acs.jpcc.8b03660.
[77] Busó-Rogero C, Herrero E, Feliu JM. Ethanol Oxidation on Pt Single-Crystal Electrodes: Surface-Structure Effects in Alkaline Medium. ChemPhysChem 2014;15:2019–28. https://doi.org/10.1002/cphc.201402044.
[78] Hernández J, Solla-Gullón J, Herrero E, Aldaz A, Feliu JM. Electrochemistry of Shape-Controlled Catalysts: Oxygen Reduction Reaction on Cubic Gold Nanoparticles. J Phys Chem C 2007;111:14078–83. https://doi.org/10.1021/jp0749726.
[79] Liao H-G, Jiang Y-X, Zhou Z-Y, Chen S-P, Sun S-G. Shape-Controlled Synthesis of Gold Nanoparticles in Deep Eutectic Solvents for Studies of Structure-Functionality Relationships in Electrocatalysis. Angew Chem Int Ed 2008;47:9100–3. https://doi.org/10.1002/anie.200803202.
[80] Chen Y, Milenkovic S, Hassel AW. {110}-Terminated Square-shaped Gold Nanoplates and their Electrochemical Surface Reactivity. ChemElectroChem 2017;4:557–64. https://doi.org/10.1002/celc.201600307.
[81] Tian N, Zhou Z-Y, Sun S-G, Ding Y, Wang ZL. Synthesis of Tetrahexahedral platinum Nanocrystals with High-Index Facets and High Electro-Oxidation activity. Science 1979;2007(316):732–5. https://doi.org/10.1126/science.1140484.
[82] Choi M, Siepser NP, Jeong S, Wang Y, Jagdale G, Ye X, et al. Probing Single-Particle Electrocatalytic Activity at Facet-Controlled Gold Nanocrystals. Nano Lett 2020;20:1233–9. https://doi.org/10.1021/acs.nanolett.9b04640.
[83] Lim J, Liu C-Y, Park J, Liu Y-H, Senftle TP, Lee SW, et al. Structure Sensitivity of Pd Facets for Enhanced Electrochemical Nitrate Reduction to Ammonia. ACS Catal 2021;11:7568–77. https://doi.org/10.1021/acscatal.1c01413.
[84] De Gregorio GL, Burdyny T, Loiudice A, Iyengar P, Smith WA, Buonsanti R. Facet-Dependent Selectivity of Cu Catalysts in Electrochemical CO_2 Reduction at Commercially Viable Current Densities. ACS Catal 2020;10:4854–62. https://doi.org/10.1021/acscatal.0c00297.
[85] Kempler PA, Coridan RH, Luo L. Gas Evolution in Water Electrolysis. Chem Rev 2024;124:10964–1007. https://doi.org/10.1021/acs.chemrev.4c00211.
[86] Liu S, Li Y, Wang D, Xi S, Xu H, Wang Y, et al. Alkali Cation-Induced Cathodic Corrosion in Cu Electrocatalysts. Nat Commun 2024;15:5080. https://doi.org/10.1038/s41467-024-49492-7.
[87] Sandbeck DJS, Secher NM, Speck FD, Sørensen JE, Kibsgaard J, Chorkendorff I, et al. Particle Size Effect on Platinum Dissolution: Considerations for Accelerated Stability Testing of Fuel Cell Catalysts. ACS Catal 2020;10:6281–90. https://doi.org/10.1021/acscatal.0c00779.
[88] Fuchs T, Briega-Martos V, Drnec J, Stubb N, Martens I, Calle-Vallejo F, et al. Anodic and Cathodic platinum Dissolution Processes Involve Different Oxide Species. Angew Chem Int Ed 2023;62:e202304293. https://doi.org/10.1002/anie.202304293.
[89] Bae JH, Brocenschi RF, Kisslinger K, Xin HL, Mirkin MV. Dissolution of Pt during Oxygen Reduction Reaction Produces Pt Nanoparticles. Anal Chem 2017;89:12618–21. https://doi.org/10.1021/acs.analchem.7b03121.
[90] Arulmozhi N, Esau D, Lamsal RP, Beauchemin D, Jerkiewicz G. Structural Transformation of Monocrystalline Platinum Electrodes upon Electro-oxidation and Electro-dissolution. ACS Catal 2018;8:6426–39. https://doi.org/10.1021/acscatal.8b00319.
[91] Ibach H, Physics of. Surfaces and Interfaces 2006.
[92] Kolb D. Reconstruction Phenomena at Metal-Electrolyte Interfaces. Prog Surf Sci 1996;51:109–73. https://doi.org/10.1016/0079-6816(96)00002-0.
[93] Hermann JM, Abdelrahman A, Jacob T, Kibler LA. Potential-dependent Reconstruction Kinetics Probed by HER on Au(111) Electrodes. Electrochim Acta 2020;347:136287. https://doi.org/10.1016/j.electacta.2020.136287.
[94] Woodruff DP. Adsorbate-induced Reconstruction of Surfaces: an Atomistic Alternative to Microscopic Faceting? J Phys Condens Matter 1994;6:6067–94. https://doi.org/10.1088/0953-8984/6/31/007.
[95] Sun JT, Gao L, He XB, Cheng ZH, Deng ZT, Lin X, et al. Surface Reconstruction Transition of Metals induced by Molecular Adsorption. Phys Rev B 2011;83:115419. https://doi.org/10.1103/PhysRevB.83.115419.
[96] Huang M. First-Principles Study on the Reconstruction Induced by the Adsorption of C_{60} on Pt(111). PCCP 2012;14:4959. https://doi.org/10.1039/c2cp23592g.

[97] Ovalle VJ, Waegele MM. Impact of Electrolyte Anions on the Adsorption of CO on Cu Electrodes. J Phys Chem C 2020;124:14713–21. https://doi.org/10.1021/acs.jpcc.0c04037.

[98] Abdelrahman A, Hermann JM, Jacob T, Kibler LA. Adsorption of Acetate on Au(111): an *in-situ* Scanning Tunnelling Microscopy Study and Implications on Formic Acid Electrooxidation. ChemPhysChem 2019;20:2989–96. https://doi.org/10.1002/cphc.201900560.

[99] Sandbeck DJS, Brummel O, Mayrhofer KJJ, Libuda J, Katsounaros I, Cherevko S. Dissolution of Platinum Single Crystals in Acidic Medium. ChemPhysChem 2019;20:2997–3003. https://doi.org/10.1002/cphc.201900866.

[100] Cherevko S, Zeradjanin AR, Topalov AA, Kulyk N, Katsounaros I, Mayrhofer KJJ. Dissolution of Noble Metals during Oxygen Evolution in Acidic Media. ChemCatChem 2014;6:2219–23. https://doi.org/10.1002/cctc.201402194.

[101] Yang Y, Xiong Y, Zeng R, Lu X, Krumov M, Huang X, et al. Operando Methods in Electrocatalysis ACS Catal 2021;11:1136–78. https://doi.org/10.1021/acscatal.0c04789.

[102] Chen S, Ma L, Huang Z, Liang G. Zhi C. *In situ/operando* Analysis of surface Reconstruction of Transition Metal-based Oxygen Evolution Electrocatalysts. Cell Rep Phys Sci 2022;3:100729. https://doi.org/10.1016/j.xcrp.2021.100729.

[103] Matzik FM, Hermann JM, Kibler LA, Jacob T. Au(111) Surface Oxidation Kinetics Probed by Electrocatalytic Oxidation of Formic Acid. J Electrochem Soc 2022;169:116513. https://doi.org/10.1149/1945-7111/aca3d5.

[104] Hermann JM, Müller H, Daccache L, Adler C, Keller S, Metzler M, et al. Formic Acid Oxidation Reaction on Au(111) Electrodes Modified with 4-Mercaptopyridine SAM. Electrochim Acta 2021;388:138547. https://doi.org/10.1016/j.electacta.2021.138547.

[105] Sebastián-Pascual P, Escudero-Escribano M. Surface Characterization of Copper Electrocatalysts by Lead Underpotential Deposition. J Electroanal Chem 2021;896. https://doi.org/10.1016/j.jelechem.2021.115446.

[106] Magnussen OM. Ordered Anion Adlayers on Metal Electrode Surfaces. Chem Rev 2002;102:679–726. https://doi.org/10.1021/cr000069p.

[107] Jacobse L, Rost MJ, Koper MTM. Atomic-Scale Identification of the Electrochemical Roughening of Platinum. ACS Cent Sci 2019;5:1920–8. https://doi.org/10.1021/acscentsci.9b00782.

[108] Baeckmann WV, Schwenk W, Prinz W. Handbook of Cathodic Corrosion Protection. (3rd ed.). Elsevier; 1997.

[109] Hersbach TJP, Koper MTM, Cathodic Corrosion,. 21st Century Insights into a 19th Century Phenomenon. Curr Opin. Electrochem 2021;26:100653. https://doi.org/10.1016/j.coelec.2020.100653.

[110] Hersbach TJP, Yanson AI, Koper MTM. Anisotropic Etching of Platinum Electrodes at the Onset of Cathodic Corrosion. Nat Commun 2016;7:12653. https://doi.org/10.1038/ncomms12653.

[111] Bernal Lopez M, Ustarroz J. Electrodeposition of Nanostructured Catalysts for Electrochemical Energy Conversion: Current Trends and Innovative Strategies. Curr Opin. Electrochem 2021;27:100688. https://doi.org/10.1016/j.coelec.2021.100688.

[112] Budevski E, Staikov G, Lorenz WJ. Electrocrystallization. Electrochim Acta 2000;45:2559–74. https://doi.org/10.1016/S0013-4686(00)00353-4.

[113] Rurainsky C, Manjón AG, Hiege F, Chen YT, Scheu C, Tschulik K. Electrochemical Dealloying as a Tool to Tune the Porosity, Composition and Catalytic Activity of Nanomaterials. J Mater Chem A 2020;8:19405–13. https://doi.org/10.1039/d0ta04880a.

[114] Perdriel CL, Arvia AJ, Ipohorski M. Electrochemical Faceting of Polycrystalline Gold in 1 M H_2SO_4. J Electroanal Chem Interfacial Electrochem 1986;215:317–29. https://doi.org/10.1016/0022-0728(86)87025-5.

[115] Xiao C, Lu B-A, Xue P, Tian N, Zhou Z-Y, Lin X, et al. High-Index-Facet- and High-Surface-Energy Nanocrystals of Metals and Metal Oxides as Highly Efficient Catalysts. Joule 2020;4:2562–98. https://doi.org/10.1016/j.joule.2020.10.002.

[116] Raaijman SJ, Arulmozhi N, Koper MTM. Anisotropic Cathodic Corrosion of Gold Electrodes in the Absence and Presence of Carbon Monoxide. J Phys Chem C 2020;124:28539–54. https://doi.org/10.1021/acs.jpcc.0c08574.

[117] Yang H, Driess M, Menezes PW. Self-Supported Electrocatalysts for Practical Water Electrolysis. Adv Energy Mater 2021;11. https://doi.org/10.1002/aenm.202102074.

[118] Lu X, Yu T, Wang H, Qian L, Lei P. Electrochemical Fabrication and Reactivation of Nanoporous Gold with Abundant Surface Steps for CO_2 Reduction. ACS Catal 2020;10:8860–9. https://doi.org/10.1021/acscatal.0c00627.

[119] Yan Z, Sun H, Chen X, Liu H, Zhao Y, Li H, et al. Anion Insertion Enhanced Electrodeposition of Robust Metal Hydroxide/Oxide Electrodes for Oxygen Evolution. Nat Commun 2018;9:2373. https://doi.org/10.1038/s41467-018-04788-3.

[120] Elnagar MM, Hermann JM, Jacob T, Kibler LA. Tailoring the Electrode Surface Structure by Cathodic Corrosion in Alkali Metal Hydroxide Solution: Nanostructuring and Faceting of Au. Curr Opin. Electrochem 2021;27:100696. https://doi.org/10.1016/j.coelec.2021.100696.

[121] Lim J, Kim K-H, Cojocaru C-S. Highly Uniform, Straightforward, Controllable Fabrication of Copper Nano-objects via Artificial Nucleation-assisted Electrodeposition. J Electroanal Chem 2021;897:115594. https://doi.org/10.1016/j.jelechem.2021.115594.

[122] Morsali R, Qian D, Minary-Jolandan M. Mechanisms of Localized Pulsed Electrodeposition (L-PED) for Microscale 3D Printing of Nanotwinned Metals. J Electrochem Soc 2019;166:D354. https://doi.org/10.1149/2.0051910jes.

[123] Liu J, Duan JL, Toimil-Molares ME, Karim S, Cornelius TW, Dobrev D, et al. Electrochemical Fabrication of Single-Crystalline and Polycrystalline Au Nanowires: the Influence of Deposition Parameters. Nanotechnology 2006;17:1922–6. https://doi.org/10.1088/0957-4484/17/8/020.

[124] Kibler LA, El-Aziz AM, Hoyer R, Kolb DM. Tuning Reaction rates by Lateral Strain in a Palladium Monolayer. Angew Chem Int Ed 2005;44:2080–4. https://doi.org/10.1002/anie.200462127.

[125] Tang J, Petri M, Kibler LA, Kolb DM. Pd Deposition onto Au(111) Electrodes from Sulphuric Acid Solution. Electrochim Acta 2005;51:125–32. https://doi.org/10.1016/j.electacta.2005.04.009.

[126] Kibler LA, El-Aziz AM, Kolb DM. Electrochemical Behaviour of Pseudomorphic Overlayers: Pd on Au(1 1 1). J Mol Catal A Chem 2003;199:57–63. https://doi.org/10.1016/S1381-1169(03)00018-9.

[127] Hussein HEM, Maurer RJ, Amari H, Peters JJP, Meng L, Beanland R, et al. Tracking Metal Electrodeposition Dynamics from Nucleation and Growth of a Single Atom to a Crystalline Nanoparticle. ACS Nano 2018;12:7388–96. https://doi.org/10.1021/acsnano.8b04089.

[128] Liu Y, Gokcen D, Bertocci U, Moffat TP. Self-Terminating Growth of Platinum Films by Electrochemical Deposition. Science 1979;2012(338):1327–30. https://doi.org/10.1126/science.1228925.

[129] Sasaki K, Naohara H, Choi Y, Cai Y, Chen W-F, Liu P, et al. Highly Stable Pt Monolayer on PdAu Nanoparticle Electrocatalysts for the Oxygen Reduction Reaction. Nat Commun 2012;3:1115. https://doi.org/10.1038/ncomms2124.

[130] Baldauf M, Kolb DM. Formic Acid Oxidation on Ultrathin Pd Films on Au(*hkl*) and Pt(*hkl*) Electrodes. J Phys Chem 1996;100:11375–81. https://doi.org/10.1021/jp952859m.

[131] Shi Y, Huang W-M, Li J, Zhou Y, Li Z-Q, Yin Y-C, et al. Site-specific Electrodeposition Enables Self-terminating Growth of Atomically Dispersed Metal Catalysts. Nat Commun 2020;11:4558. https://doi.org/10.1038/s41467-020-18430-8.

[132] Zakaria ND, Omar MH, Ahmad Kamal NN, Abdul Razak K, Sönmez T, Balakrishnan V, et al. Effect of Supporting Background Electrolytes on the Nanostructure Morphologies and Electrochemical Behaviors of Electrodeposited Gold Nanoparticles on Glassy Carbon Electrode Surfaces. ACS Omega 2021;6:24419–31. https://doi.org/10.1021/acsomega.1c02670.

[133] Abbondanza G, Larsson A, Linpé W, Hetherington C, Carlá F, Lundgren E, et al. Templated Electrodeposition as a Scalable and Surfactant-free Approach to the Synthesis of Au Nanoparticles with Tunable Aspect Ratios. Nanoscale Adv 2022;4:2452–67. https://doi.org/10.1039/D2NA00188H.

[134] Gotti G, Fajerwerg K, Evrard D, Gros P. Electrodeposited Gold Nanoparticles on Glassy Carbon: Correlation between Nanoparticles Characteristics and Oxygen Reduction Kinetics in Neutral Media. Electrochim Acta 2014;128:412–9. https://doi.org/10.1016/j.electacta.2013.10.172.

[135] Shu H, Cao L, Chang G, He H, Zhang Y, He Y. Direct Electrodeposition of Gold Nanostructures onto Glassy Carbon Electrodes for Non-enzymatic Detection of Glucose. Electrochim Acta 2014;132:524–32. https://doi.org/10.1016/j.electacta.2014.04.031.

[136] Moon Y, Kim J, Park J, Kim K, Kwon G, Kim J. Coordination Tuning of Nanoporous Metal Films by Secondary Electrodeposition to Optimize Methanol Electrooxidation Activity. Nanoscale 2025;17:22361–7. https://doi.org/10.1039/D5NR01650A.

[137] Yeo K-R, Kim H, Lee K-S, Kim S, Lee J, Park H, et al. Controlled Doping of Ultralow Amounts Ru on Ni Cathode for PEMWE: Experimental and Theoretical Elucidation of Enhanced Performance. Applied Catalysis B: Environment and Energy 2024;346:123738. https://doi.org/10.1016/j.apcatb.2024.123738.
[138] Rost MJ. Nucleation and growth of Nano-Islands during Surface Reactions or Alloying with Increased Lattice Constant. J Electrochem Soc 2023;170:012504. https://doi.org/10.1149/1945-7111/acaa02.
[139] Krug J. Four Lectures on the Physics of Crystal Growth. Physica A 2002;313:47–82. https://doi.org/10.1016/S0378-4371(02)01034-8.
[140] Menezes PV, Elnagar MM, Al-Shakran M, Eckl MJ, Menezes PW, Kibler LA, et al. In-Liquid Plasma for Surface Engineering of Cu Electrodes with Incorporated SiO_2 Nanoparticles: from Micro to Nano. Adv Funct Mater 2022;32:2107058. https://doi.org/10.1002/adfm.202107058.
[141] Zhao G, Lin J, Lu M, Li L, Xu P, Liu X, et al. Potential Cycling Boosts the Electrochemical Conversion of Polyethylene Terephthalate-derived Alcohol into Valuable Chemicals. Nat Commun 2024;15:8463. https://doi.org/10.1038/s41467-024-52789-2.
[142] Sukeri A, Saravia LPH, Bertotti M. A Facile Electrochemical Approach to Fabricate a Nanoporous Gold Film Electrode and its Electrocatalytic Activity Towards Dissolved Oxygen Reduction. PCCP 2015;17:28510–4. https://doi.org/10.1039/C5CP05220C.
[143] Sukeri A, Bertotti M. Nanoporous Gold Surface: an Efficient Platform for Hydrogen Evolution Reaction at very Low Overpotential. J Braz Chem Soc 2017: 226–31. https://doi.org/10.21577/0103-5053.20170132.
[144] Fang C, Bandaru NM, Ellis AV, Voelcker NH. Electrochemical Fabrication of Nanoporous Gold. J Mater Chem 2012;22:2952–7. https://doi.org/10.1039/C2JM14889G.
[145] Chopra D, Guo T, Ivanovski S, Gulati K. Single-step Nano-Engineering of Multiple Micro-rough Metals via Anodization. Nano Res 2023;16:1320–9. https://doi.org/10.1007/s12274-022-4847-8.
[146] Jiang L, Li P, Wang S, Liu R, Zhu X, Song Y, van Ree T. Anodization Fabrication Techniques and Energy-related Applications for Nanostructured Anodic Films on Transition Metals. Energy Mater 2022;2:200038. https://doi.org/10.20517/energymater.2022.52.
[147] Elbanna AM, Salem KE, Mokhtar AM, Ramadan M, Elgamal M, Motaweh HA, et al. Ternary Ti–Mo–Fe Nanotubes as Efficient Photoanodes for Solar-Assisted Water Splitting. J Phys Chem C 2021;125:12504–17. https://doi.org/10.1021/acs.jpcc.1c01478.
[148] Mao X, Xiao T, Zhang Q, Liu Z. An Electrochemical Anodization Strategy Towards High-Activity Porous MoS_2 Electrodes for the Hydrogen Evolution Reaction. RSC Adv 2018;8:15030–5. https://doi.org/10.1039/C8RA01554F.
[149] Dai X-C, Hou S, Huang M-H, Li Y-B, Li T, Xiao F-X. Electrochemically Anodized One-Dimensional Semiconductors: A Fruitful Platform for Solar Energy Conversion. J Phys: Energy 2019;022002(1). https://doi.org/10.1088/2515-7655/ab0718.
[150] Jarosz M, Grudzień J, Kapusta-Kołodziej J, Chudecka A, Sołtys M, Sulka GD. Anodization of Titanium Alloys for Biomedical Applications. Nanostructured Anodic Metal Oxides, Elsevier 2020:211–75. https://doi.org/10.1016/B978-0-12-816706-9.00007-8.
[151] Sikdar S, Menezes PV, Maccione R, Jacob T, Menezes PL. Plasma Electrolytic Oxidation (PEO) Process—Processing, Properties, and Applications. Nanomaterials 2021;11:1375. https://doi.org/10.3390/nano11061375.
[152] Lu X, Blawert C, Zheludkevich ML, Kainer KU. Insights into Plasma Electrolytic Oxidation Treatment with Particle Addition. Corros Sci 2015;101:201–7. https://doi.org/10.1016/j.corsci.2015.09.016.
[153] Baranov O, Levchenko I, Bell JM, Lim JWM, Huang S, Xu L, et al. From Nanometre to Millimetre: a Range of Capabilities for Plasma-enabled Surface Functionalization and Nanostructuring. Mater Horiz 2018;5:765–98. https://doi.org/10.1039/c8mh00326b.
[154] Lou BS, Lin YY, Tseng CM, Lu YC, Duh JG, Lee JW. Plasma Electrolytic Cxidation Coatings on AZ31 Magnesium Alloys with Si_3N_4 Nanoparticle Additives. Surf Coat Technol 2017;332:358–67. https://doi.org/10.1016/j.surfcoat.2017.05.094.
[155] Lu X, Blawert C, Huang Y, Ovri H, Zheludkevich ML, Kainer KU. Plasma Electrolytic Oxidation Coatings on Mg Alloy with Addition of SiO_2 Particles. Electrochim Acta 2016;187:20–33. https://doi.org/10.1016/j.electacta.2015.11.033.
[156] Sen Gupta SK, Singh R. Cathodic Contact Glow Discharge Electrolysis: its Origin and Non-Faradaic Chemical Effects. Plasma Sources Sci Technol 2016;26: 015005. https://doi.org/10.1088/0963-0252/26/1/015005.
[157] Kaseem M, Fatimah S, Nashrah N, Ko YG. Recent Progress in Surface Modification of Metals Coated by Plasma Electrolytic Oxidation: Principle, Structure, and Performance. Prog Mater Sci 2021;117:100735. https://doi.org/10.1016/j.pmatsci.2020.100735.
[158] Zhang G, Huang X, Ma X, Liu Y, Ying Y, Guo X, et al. A Fast and General Approach to Produce a Carbon Coated Janus Metal/Oxide Hybrid for Catalytic Water Splitting. J Mater Chem A 2021;9:7606–16. https://doi.org/10.1039/D0TA12021A.
[159] Ji R-Y, Huang R, Cheng X-Y, Fu F, Jiang Y-X, Sun S-G. Controlled Synthesis of High-index Faceted Pt Nanocatalysts Directly on Carbon Paper for Methanol Electrooxidation. Electrocatalysis 2022. https://doi.org/10.1007/s12678-022-00749-z.
[160] Xiao C, Tian N, Tang J-X, Chen L-F, Zhou Z-Y, Sun S-G. Electrolyte Effects on the Shape-controlled Synthesis of Pt Nanocrystals by Electrochemical Square-Wave Potential Method. J Electroanal Chem 2023;935:117344. https://doi.org/10.1016/j.jelechem.2023.117344.
[161] Han L, Tian B, Gao X, Zhong Y, Wang S, Song S, et al. Copper Nanowire with Enriched High-Index Facets for Highly Selective CO_2 Reduction. SmartMat 2022;3: 142–50. https://doi.org/10.1002/smm2.1082.
[162] Xiao C, Tian N, Li W-Z, Qu X-M, Du J-H, Lu B-A, et al. Shape Transformations of Pt Nanocrystals Enclosed with High-Index Facets and Low-Index Facets. CrstEngComm 2021;23:6655–60. https://doi.org/10.1039/D1CE00949D.
[163] Xiao J, Liu S, Tian N, Zhou Z-Y, Liu H-X, Xu B-B, et al. Synthesis of Convex Hexoctahedral Pt Micro/Nanocrystals with High-Index Facets and Electrochemistry-Mediated Shape Evolution. J Am Chem Soc 2013;135:18754–7. https://doi.org/10.1021/ja410583b.
[164] Taranovskyy A, Guézo S, Matsushima H, Gründer Y, Magnussen OM. Studies of Electrochemical Surface Alloying and Dealloying by in situ High-Speed STM. PCCP 2012;14:10579. https://doi.org/10.1039/c2cp41023k.
[165] Erlebacher J, Aziz MJ, Karma A, Dimitrov N, Sieradzki K. Evolution of Nanoporosity in Dealloying. Nature 2001;410:450–3. https://doi.org/10.1038/35068529.
[166] Erlebacher J, Seshadri R. Hard Materials with Tunable Porosity. MRS Bull 2009;34:561–8. https://doi.org/10.1557/mrs2009.155.
[167] Li X, Chen Q, McCue I, Snyder J, Crozier P, Erlebacher J, et al. Dealloying of Noble-Metal Alloy Nanoparticles. Nano Lett 2014;14:2569–77. https://doi.org/10.1021/nl500377g.
[168] Koh S, Strasser P. Electrocatalysis on Bimetallic Surfaces: Modifying Catalytic Reactivity for Oxygen Reduction by Voltammetric Surface Dealloying. J Am Chem Soc 2007;129:12624–5. https://doi.org/10.1021/ja0742784.
[169] Mondal S, Raj CR. Electrochemical Dealloying-Assisted Surface-Engineered Pd-based Bifunctional Electrocatalyst for Formic Acid Oxidation and Oxygen Reduction. ACS Appl Mater Interfaces 2019;11:14110–9. https://doi.org/10.1021/acsami.9b00589.
[170] Jana R, Bhim A, Bothra P, Pati SK, Peter SC. Electrochemical Dealloying of $PdCu_3$ Nanoparticles to Achieve Pt-like activity for the Hydrogen Evolution Reaction. ChemSusChem 2016;9:2922–7. https://doi.org/10.1002/cssc.201601081.
[171] Bruckenstein S, Shay M. An in situ Weighing Study of the Mechanism for the Formation of the Adsorbed Oxygen Monolayer at a Gold Electrode. J Electroanal Chem Interfacial Electrochem 1985;188:131–6. https://doi.org/10.1016/S0022-0728(85)80057-7.
[172] Gordon JS, Johnson DC. Application of an Electrochemical Quartz Crystal Microbalance to a Study of Water Adsorption at Gold Surfaces in Acidic Media. J Electroanal Chem 1994;365:267–74. https://doi.org/10.1016/0022-0728(94)02965-2.
[173] Stamenkovic VR, Fowler B, Mun BS, Wang G, Ross PN, Lucas CA, et al. Improved Oxygen Reduction Activity on Pt_3 Ni(111) via Increased Surface Site Availability. Science 1979;2007(315):493–7. https://doi.org/10.1126/science.1135941.
[174] Strasser P, Koh S, Anniyev T, Greeley J, More K, Yu C, et al. Lattice-Strain Control of the Activity in Dealloyed Core–Shell Fuel Cell Catalysts. Nat Chem 2010;2: 454–60. https://doi.org/10.1038/nchem.623.
[175] Yu W, Porosoff MD, Chen JG. Review of Pt-based Bimetallic Catalysis: from Model Surfaces to Supported Catalysts. Chem Rev 2012;112:5780–817. https://doi.org/10.1021/cr300096b.
[176] F. Haber Über Elektrolyse der Salzsäure nebst Mitteilungen über kathodische Formation von Blei III Mitteilung Zeitschrift Für Anorganische Chemie 16 1898 438 449 10.1002/zaac.18980160144.
[177] Haber F. The Phenomenon of the Formation of Metallic Dust from Cathodes. Trans Am Electrochem Soc 1902:189–96.

[178] Kabanov BN, Astakhov II, Kiseleva IG. Formation of Crystalline Intermetallic Compounds and Solid Solutions in Electrochemical Incorporation of Metals into Cathodes. Electrochim Acta 1979;24:167–71. https://doi.org/10.1016/0013-4686(79)80020-1.
[179] Salzberg HW, Mies F. Cathodic Disintegration of Tin. J Electrochem Soc 1958;105:64. https://doi.org/10.1149/1.2428763.
[180] Evazzade I, Zagalskaya A, Alexandrov V. Revealing Elusive Intermediates of Platinum Cathodic Corrosion through DFT Simulations. J Phys Chem Lett 2022;13:3047–52. https://doi.org/10.1021/acs.jpclett.1c04187.
[181] Hersbach TJP, Mints VA, Calle-Vallejo F, Yanson AI, Koper MTM. Anisotropic Etching of Rhodium and Gold as the Onset of Nanoparticle Formation by Cathodic Corrosion. Faraday Discuss 2016;193:207–22. https://doi.org/10.1039/c6fd00078a.
[182] Kromer ML, Monzó J, Lawrence MJ, Kolodziej A, Gossage ZT, Simpson BH, et al. High-Throughput Preparation of Metal Oxide Nanocrystals by Cathodic Corrosion and their use as active Photocatalysts. Langmuir 2017;33:13296–302. https://doi.org/10.1021/acs.langmuir.7b02465.
[183] Wei Q, Wang P, Ma Y, Du K, Yin H, Zhu H, et al. The Correlation of the Nickel (111) Facet with the Hydrogen Evolution Performance of Ni Electrodes in Alkaline Solutions. J Electroanal Chem 2022;923:116833. https://doi.org/10.1016/j.jelechem.2022.116833.
[184] Simonet J. Large-Scale Cathodic Carboxylation of Copper Surfaces. Electrochem Commun 2017;76:67–70. https://doi.org/10.1016/j.elecom.2017.01.018.
[185] Katsounaros I, Ipsakis D, Polatides C, Kyriacou G. Efficient Electrochemical Reduction of Nitrate to Nitrogen on Tin Cathode at very High Cathodic Potentials. Electrochim Acta 2006;52:1329–38. https://doi.org/10.1016/j.electacta.2006.07.034.
[186] Elnagar MM, Jacob T, Kibler LA. Cathodic Corrosion of Au in Aqueous Methanolic Alkali Metal Hydroxide Electrolytes: Notable Role of Water. Electrochem Sci Adv 2022;2:e2100175. https://doi.org/10.1002/elsa.202100175.
[187] Hersbach TJP, Garcia-Esparza AT, Hanselman S, Paredes Mellone OA, Hoogenboom T, McCrum IT, et al. Platinum Hydride Formation during Cathodic Corrosion in Aqueous Solutions. Nat Mater 2025;24:574–80. https://doi.org/10.1038/s41563-024-02080-y.
[188] Elnagar MM, Kibler LA, Jacob T. Structural Evolution of Au Electrodes during Cathodic Corrosion: Initial Stages of Octahedral-Nanocrystal Growth. J Electrochem Soc 2022;169:102509. https://doi.org/10.1149/1945-7111/ac9930.
[189] Pourbaix M. Atlas of Electrochemical Equilibria in Aqueous Solution. National Association of Corrosion Engineers 1974.
[190] Ryu J, Surendranath Y. Polarization-Induced local pH Swing Promotes Pd-Catalyzed CO_2 Hydrogenation. J Am Chem Soc 2020;142:13384–90. https://doi.org/10.1021/jacs.0c01123.
[191] Monteiro MCO, Jacobse L, Touzalin T, Koper MTM. Mediator-Free SECM for probing the Diffusion Layer pH with Functionalized Gold Ultramicroelectrodes. Anal Chem 2020;92:2237–43. https://doi.org/10.1021/acs.analchem.9b04952.
[192] P.W. Atkins J. de Paula Kurzlehrbuch Physikalische Chemie 2008 Wiley-VCH Weinheim n.d.
[193] G. Wedler Lehrbuch Der Physikalischen Chemie 2007 Wiley-VCH Weinheim n.d.
[194] Wu J. Understanding the Electric Double-Layer Structure, Capacitance, and Charging Dynamics. Chem Rev 2022;122:10821–59. https://doi.org/10.1021/acs.chemrev.2c00097.
[195] Helmholtz H. Ann Der Phys Und Chemie 1879;7:337–82.
[196] Kariv-Miller E, Christian PD, Svetlicic V. Ex Situ Structural Studies of a Tetraalkylammonium Lead Compound. Langmuir 1994;10:3338–42. https://doi.org/10.1021/la00021a070.
[197] Kariv-Miller E, Lawin PB, Vajtner Z. The Reduction of Tetraalkylammonium Ions on Metal Electrodes. J Electroanal Chem Interfacial Electrochem 1985;195:435–8. https://doi.org/10.1016/0022-0728(85)80064-4.
[198] Simonet J, Labaume E, Rault-Berthelot J. On the Cathodic Corrosion of Platinum in the Presence of Iodides in Dry Aprotic Solvents. Electrochem Commun 1999;1:252–6. https://doi.org/10.1016/S1388-2481(99)00050-8.
[199] Ghilane J, Guilloux-Viry M, Lagrost C, Hapiot P, Simonet J. Cathodic Modifications of Platinum Surfaces in Organic Solvent: Reversibility and Cation Type Effects. J Phys Chem B 2005;109:14925–31. https://doi.org/10.1021/jp051846y.
[200] Hoch C, Simon A. Tetramethylammoniumamalgam, $[N(CH_3)_4]Hg_8$. Z Anorg Allg Chem 2006;632:2288–94. https://doi.org/10.1002/zaac.200600163.
[201] Kariv-Miller E, Lawin PB. Tetraalkylammonium-lead: Electrogeneration and Stoichiometry. J Electroanal Chem Interfacial Electrochem 1988;247:345–9. https://doi.org/10.1016/0022-0728(88)80156-6.
[202] Teherani TH, Peer WJ, Lagowski JJ, Bard AJ. Electrochemical Behavior and Standard Potential of Gold(1-) Ion in Liquid Ammonia. J Am Chem Soc 1978;100. https://doi.org/10.1021/ja00492a077.
[203] Miao M, Brgoch J, Krishnapriyan A, Goldman A, Kurzman JA, Seshadri R. On the Stereochemical Inertness of the Auride Ione Pair: Ab Initio Studies of AAu (a = K, Rb, Cs). Inorg Chem 2013;52:8183–9. https://doi.org/10.1021/ic400947p.
[204] Ghilane J, Fontaine O, Martin P, Lacroix J-C, Randriamahazaka H. Formation of Negative Oxidation States of Platinum and Gold in Redox Ionic Liquid: Electrochemical Evidence. Electrochem Commun 2008;10. https://doi.org/10.1016/j.elecom.2008.05.038.
[205] Lu F, Ji X, Yang Y, Deng W, Banks CE. Room Temperature Ionic Liquid Assisted Well-Dispersed Core-Shell Tin Nanoparticles through Cathodic Corrosion. RSC Adv 2013;3:18791–3. https://doi.org/10.1039/c3ra43532f.
[206] Elnagar MM, Kibler LA, Jacob T. Electrochemical Fabrication of Nanoparticles and Single-Atom Catalysts via Cathodic Corrosion. Chemistry – a. European Journal 2025;31:e202500036. https://doi.org/10.1002/chem.202500036.
[207] Sun W, Min B, Wang M, Han X, Gao Q, Hwang S, et al. Cathodic Corrosion-Induced Structural Evolution of CuNi Electrocatalysts for Enhanced CO_2 Reduction. Materials and Interfaces 2024:79–88. https://doi.org/10.53941/mi.2024.100007.
[208] Liu J, Chen L, Liu X. Deep Insight into Characterizing the Metal–Support Interface in Heterogeneous Catalysis. ACS Catal 2024;14:1987–2002. https://doi.org/10.1021/acscatal.3c04930.
[209] Wang H, Zhou X, Yu T, Lu X, Qian L, Liu P, et al. Surface Restructuring in AgCu Single-Atom Alloy Catalyst and Self-enhanced Selectivity toward CO_2 Reduction. Electrochim Acta 2022;426:140774. https://doi.org/10.1016/j.electacta.2022.140774.
[210] Harti H, Bubendorff J-L, Florentin A, Pirri C, Ebothe J. Analysis of the Substrate Effect on the Nucleation and Growth Mode of Electrodeposited Cobalt on Copper and Graphite Electrodes. J Cryst Growth 2011;319:79–87. https://doi.org/10.1016/j.jcrysgro.2011.01.028.
[211] Hsiao P-Y, Tsai Z-H, Huang J-H, Yu G-P. Strong Asymmetric Effect of Lattice Mismatch on Epilayer Structure in Thin-Film Deposition. Phys Rev B 2009;79:155414. https://doi.org/10.1103/PhysRevB.79.155414.
[212] Ding Y, Gu Q, Klyushin A, Huang X, Choudhury SH, Spanos I, et al. Dynamic Carbon Surface Chemistry: Revealing the Role of Carbon in Electrolytic Water Oxidation. J Energy Chem 2020;47:155–9. https://doi.org/10.1016/j.jechem.2019.12.006.
[213] Choudhury SH, Ding Y, Yi Y, Rohner C, Frandsen W, Lunkenbein T, et al. Oxidation Behavior of Glassy Carbon in Acidic Electrolyte. ChemElectroChem 2022;9:e202200637. https://doi.org/10.1002/celc.202200637.
[214] Sun J, Dang Y, Sun X, Heumann S, Ding Y. Can Carbon be used as an Anode for Water Splitting? ChemSusChem 2025;18:e202401340. https://doi.org/10.1002/cssc.202401340.